BRASKI

DOE/ET-0058/7

Alloy Development for Irradiation Performance

Quarterly Progress Report

For Period Ending September 30, 1979

U.S. Department of Energy

Assistant Secretary for Energy Technology

Office of Fusion Energy

Printed in the United States of America. Available from
National Technical Information Service
U.S. Department of Commerce
5285 Port Royal Road, Springfield, Virginia 22161
NTIS price codes—Printed Copy: A09 Microfiche A01

DOE/ET-0058/7
Distribution
Category
UC-20, 20c

ALLOY DEVELOPMENT FOR IRRADIATION PERFORMANCE QUARTERLY PROGRESS REPORT FOR PERIOD ENDING SEPTEMBER 30, 1979

Compiled and Edited by B. G. Ashdown, ORNL
from Contributions of Participating Laboratories

ARGONNE NATIONAL LABORATORY

GENERAL ATOMIC COMPANY

HANFORD ENGINEERING DEVELOPMENT LABORATORY

MCDONNELL DOUGLAS ASTRONAUTICS COMPANY

NAVAL RESEARCH LABORATORY

OAK RIDGE NATIONAL LABORATORY

WESTINGHOUSE FUSION POWER SYSTEMS

Date **Published: April 1980**

Prepared by
OAK RIDGE NATIONAL LABORATORY
Oak Ridge, Tennessee 37830
operated by
UNION CARBIDE CORPORATION
for the
DEPARTMENT OF ENERGY
Under Contract No. W-7405-eng-26

FOREWORD

This report is the seventh in a series of Quarterly Technical Progress Reports on *"Alloy Development for Irradiation Performance"* (ADIP), which is one element of the Fusion Reactor Materials Program, conducted in support of the Magnetic Fusion Energy Program of the U.S. Department of Energy. Other elements of the Materials Program are:

- *Damage Analysis and Fundamental Studies (DAFS)*
- *Plasma-Materials Interaction (PMI)*
- *Special-Purpose Materials (SPM)*

The ADIP program element is a national effort composed of contributions from a number of National Laboratories and other government laboratories, universities, and industrial laboratories. It was organized by the Materials and Radiation Effects Branch, Office of Fusion Energy, DOE, and a Task Group on *Alloy Development for Irradiation Performance,* which operates under the auspices of that Branch. The purpose of this series of reports is to provide a working technical record of that effort for the use of the program participants, for the fusion energy program in general, and for the Department of Energy.

This report is organized along topical lines in parallel to a Program Plan of the same title so that activities and accomplishments may be followed readily relative to that Program Plan. Thus, the work of a given laboratory may appear throughout the report. Chapters 1, 2, 7, and 8 review activities on analysis and evaluation, test methods development, status of irradiation experiments, and corrosion testing and hydrogen permeation studies, respectively. These activities relate to each of the alloy development paths. Chapters 3, 4, 5, and 6 present the ongoing work on each alloy development path. The Table of Contents is annotated for the convenience of the reader.

This report has been compiled and edited under the guidance of the Chairman of the Task Group on *Alloy Development for Irradiation Performance,* E. E. Bloom, Oak Ridge National Laboratory, and his efforts, those of the supporting staff of ORNL and the many persons who made technical contributions are gratefully acknowledged. T. C. Reuther, Materials and Radiation Effects Branch, is the Department of Energy Counterpart to the Task Group Chairman and has responsibility for the ADIP Program within DOE.

Klaus M. Zwilsky, Chief,
Materials and Radiation Effects Branch
Office of Fusion Energy

CONTENTS

The status of the molten-salt thermal-convection loops (LiF-BeF_2, KNO_3-$NaNO_2$-$NaNO_3$, and LiF-$LiBr$-$LiCl$) is reviewed. The corrosion rates of type 316 stainless steel in KNO_3-$NaNO_2$-$NaNO_3$ and the composition of the salt are reported as a function of time and temperature. Corrosion rates varied from about 5 mg/m²h (4 μm/year) at 430°C to 66 mg/m²h (59 μm/year) at 550°C.

1. ANALYSIS AND EVALUATION STUDIES

The designs for power-producing fusion reactors are in a very embryonic and rapidly changing state. Requirements for materials performance are thus not well defined. However, regardless of the final designs, the environment will clearly be extremely demanding on materials in regions of high neutron flux. One cannot identify a class of alloys on which the development efforts should focus — thus the parallel paths of the Alloy Development Program. The combination of reactor designs that are evolving and the necessity for including alloys with widely different physical, chemical, and mechanical properties in the program could lead to an impossibly large number of potential problems and possible solutions. Analysis and evaluation studies are an essential part of the Alloy Development Program in order to translate fusion reactor performance goals into material property requirements and to identify crucial and generic problems on which development activities should be focused. As the Alloy Development Program proceeds and a better understanding of the behavior of materials in potential fusion reactor environments is attained, these studies will also identify problems that will necessitate design solutions.

1.1 FERRITIC STAINLESS STEELS FOR FUSION APPLICATIONS

W. Y. Chen, U. A. Peuron, P. H. Miller, Jr., J. M. Rawls, L. D. Thompson and S. N. Rosenwasser (General Atomic Company)

1.1.1 ADIP Task

ADIP Task I.A.1, Define material property requirements and make structural life predictions.

1.1.2 Objective

The objective of this study is to assess the feasibility of incorporating ferromagnetic (martensitic) steels in fusion reactor designs and to evaluate the advantages of this class of material with respect to first wall/blanket lifetime. The pertinent experience base is being evaluated, and the irradiated and unirradiated property data needed for the application of ferritic stainless steels in fusion designs are being defined as part of this task.

1.1.3 Summary

The magnetics aspects of utilizing ferromagnetic martensitic stainless steels as structural materials for tokamak reactors were studied by analytical means. For purposes of solving the associated non-linear 3-dimensional magnetostatic field problems a computer program based on an integral equation method was implemented. The program was primarily geared for geometries that are envisioned in connection with the future design of martensitic steel blankets of tokamak fusion reactors. The field perturbations and magnetic loads due to both toroidal and poloidal currents were computed and discussed.

Essentially the solutions are obtained by discretizing only the magnetized body and solving the associated linearized equations iteratively by matrix inversion for each improved value of the magnetizing vectors and susceptibilities.

The results show that the field perturbations caused by the magnetization of the blanket are in general small within the plasma region. This is due to the high degree of saturation which makes the

effective permeability to approach that of vacuum. A further small decrease in permeability is caused by the poloidal field excited by field control and plasma currents. The largest perturbations which appear in the region of blanket penetrations, that is port holes for fueling, diagnostics, etc., are still small, particularly when the penetrations are midway between the toroidal coils. The cylindrical structures analyzed tend to be self-supporting and the forces create pressures of the order of a few atmospheres. All the results indicate that the use of magnetic materials in fusion reactors should not present any feasibility questions. The effects introduced by the magnetic blanket structure can be countered by proper engineering design and selection of control parameters.

1.1.4 Progress and Status

The work during this reporting period emphasized a computer study to evaluate the design impact of employing ferromagnetic materials in first wall/blanket applications. The computer code, IRON, was utilized to analyze the toroidal field ripple resulting from ferromagnetic first wall/blanket configurations corresponding to TNS, ETF, and Starfire. The additional effects created by blanket penetrations such as neutral beam ducts were also studied. The interactions of the ferromagnetic blanket with the plasma shaping and control system, in particular the field-shaping coils, were analyzed. The most important question from the point of view of engineering impact appears to be the magnetic forces on the blanket. The magnetic forces on blanket sections of different geometries were analyzed and the implications of the resultant forces were determined.

1.1.4.1 Introduction

Martensitic 9-12% chromium steels may offer significant advantages as a first wall/blanket material in terms of greater wall lifetime in comparison with comonly considered materials such as 20CW316.[1] However, it is important to evaluate the magnetics impact of a ferromagnetic blanket on a tokamak reactor. Studies reported here have focused on two potential problem areas: the effects on plasma performance and

the impact on the mechanical design of the blanket. A 3-D field code IRON allowing the presence of saturable ferromagnetic material was used for the investigation.

One major concern in the area of plasma performance is the effect of the ferromagnetic blanket on toroidal field ripple. The code IRON was utilized extensively to analyze the toroidal field ripple of tokamak reactors with axisymmetric ferromagnetic (FM) blankets. The reactors considered have sizes and configurations corresponding to TNS[2], ETF[3], and STARFIRE[4]. The additional effects created by blanket penetrations such as neutral beam ducts were also studied.

Another concern is the interaction of the ferromagnetic blanket with the plasma shaping and control system, in particular the field-shaping coils. The code IRON was used to study the poloidal field configurations in the presence of toroidal field, which tend to put the FM blankets into a high level of saturation. The perturbations to the poloidal fields introduced by the FM blankets were computed, and the implications on the required compensations in the poloidal field controls are discussed. The possible time delay in poloidal field control caused by the presence of the FM blankets was also studied.

The most important question from the point of view of engineering impact appears to be the magnetic forces on the blanket. The magnetic forces on blanket sections of different geometries were analyzed using the code IRON, which was benchmarked by comparison with analytic calculations for axisymmetric geometries. The implications of the resultant forces on the mechanical design of the blanket are discussed.

1.1.4.2 The IRON Computer Code

The 3-D saturable iron field code IRON was developed based on a numerical formulation very similar to that utilized in the field code GFUN3D developed by the Rutherford Laboratory.[5] However, IRON was not designed for the generality GFUN3D was implemented for, so a considerably simplified coil geometry was assumed. In the present version, only a set of toroidal coils and a set of axisymmetric poloidal coils are considered. The second simplification is in the manner in which

the shapes of the ferromagnetic elements are specified. Analytic expressions are used to specify the three-dimensional boundary surfaces of the ferromagnetic elements. Typically the surfaces are of cylindrical, spherical or ellipsoidal shapes and the bodies may be further separated into smaller, usually periodic structures, by means of planes. A large number of insulating gaps may be defined by means of pairs of cutting planes. Such a scheme can most effectively take into account the inherent toroidal and poloidal symmetries of the reactor geometries.

The field $\vec{H}$ and magnetization $\vec{M}$ are solved based on an integral equation scheme similar to GFUN3D. The scalar potential ϕ_m is given by

$$\phi_m = \frac{1}{4\pi}\int \frac{\vec{M}\cdot\vec{r}}{r^3}\, dV \quad , \tag{1}$$

and the field due to the magnetized body is

$$\vec{H}_m = -\nabla\phi_m \quad . \tag{2}$$

The total field is the sum of the field due to the current flow $\vec{H}_c$ and $\vec{H}_m$

$$\vec{H} = \vec{H}_c + \vec{H}_m \quad . \tag{3}$$

Furthermore, the magnetization $\vec{M}$ is related to $\vec{H}$ by

$$\vec{M} = \chi\vec{H} \quad . \tag{4}$$

The numerical scheme involves subdividing the FM region into subelements (denoted by Greek indices, a, g, ...) each assigned a constant magnetization $\vec{M}_a$. The subdivision should be sufficiently fine so that discretizing errors are minimized, while keeping the number of subelements below a limit so that computation time does not become excessive. If $\vec{H}_\alpha$ and $\vec{H}_{c\alpha}$ are the total field and the field due to coil currents at the center of the subelement a, respectively, then for the case with N subelements

$$\vec{H}_\alpha = \vec{H}_{c\alpha} + \sum_{\beta=1}^{N} \overleftrightarrow{C}_{\alpha\beta} \cdot \vec{M}_\beta$$

$$= \vec{H}_{ca} \sum_{\beta=1}^{N} \chi_\beta \overleftrightarrow{\alpha\beta} \vec{g} \quad . \tag{5}$$

The components of the demagnetization tensor $\overleftrightarrow{C}_{\alpha\beta}$ are given by

$$C_{\alpha\beta,ij} = \frac{1}{4\pi} \int_{v_\beta} \left[3 \left(x_{\alpha i} - x'_{\beta i} \right) \left(x_{\alpha j} - x'_{\beta 1} \right) r^{-5} \right.$$

$$\left. - \delta_{ij} r^{-3} - \frac{4}{3}\pi \delta_{ij} \delta \left(\vec{x}_\alpha - \vec{x}'_\beta \right) \right] dv'_\beta \quad , \tag{6}$$

where i,j denotes the coordinate indices (x,y,z), and $\delta(\vec{r})$ is the Dirac delta function. Then the problem is reduced to iteratively solving for the local field $\vec{H}_\alpha$ and susceptibility χ_α from the set of 3N equations

$$\sum_{\beta=1}^{N} \sum_{j=1}^{3} \chi_\beta \left(C_{\alpha\beta,if} - \delta_{13} \delta_{\alpha\beta} \right) H_{\beta,jj} = H_{c\alpha,1} \quad . \tag{7}$$

As compared with GFUN3D in which the basic subelements are tetrahedral in shape, in IRON the subelements are defined by cutting the FM region with planes perpendicular to the rectangular coordinate axis. In the optional case where cylindrical coordinates are used, the boundaries of subelements are simply constant r,z or θ surfaces. The numerical computation of the demagnetization tensor $\overleftrightarrow{C}_{\alpha\beta}$ is simply a summation of Eq. (6) over a number of lattice points, and the integrand is a simple power expression free of the singularity and multivaluedness problems which plague the analytically integrated expressions for the demagnetization tensor of tetrahedral subelements.[5] Notice that the singularity in Eq. (6) when the field point and source point coincide can be easily cut off because the integration of the

first two terms of the integrand in Eq. (6) yields zero when the field point is situated at the geometric center of a rectangular cube. It was discovered that for a finite sized element such a numerical scheme converges rapidly because the integrand behaves as r^{-3}. Such an approach also avoids the difficulty in implementing the analytical integration scheme for tetrahedral elements which requires a large number of coordinate transformations.

The accuracy of IRON was checked against analytical computations for simple geometries such as a simple ferromagnetic sphere in uniform external field. In general the agreement was quite satisfactory. Accuracy to within a fraction of a percent can be achieved typically with about 50 subelements. The fact that most of the cases studied involved highly saturated FM elements implies fairly rapid convergency in the iteration. Typically less than five iterations were required to achieve the desired accuracy. The inherent toroidal symmetry also helps greatly in reducing the amount of computation time needed to solve the problem.

1.1.4.3 Results: Toroidal Field Ripple

Toroidal field ripple computations were based on reactor geometries representing three conceptual designs denoted as GA TNS, ETF and STARFIRE. The characteristic parameters most relevant in this context are given in Table 1. The blanket material was assumed to have a saturation magnetization of 1 T; this is reached when the ambient field is above 2 T, which is the case for all three examples.

TABLE 1

Parameters Used for Field Perturbation and Force Computations

	GA TNS	ETF	STARFIRE
Plasma major radius, R(m)	3.6	5.0	6.92
Plasma current (MA)	11.4	5	13.5
Number of TF-coils	12	12	12
Total TF ampere turns (10^6 A-turns)	90	132	183
Blanket thickness (m)	1	1	1.3
Outer blanket inside radius (m)	4.6	7.1	8.4
Outer blanket outside radius (m)	5.6	8.1	9.7
Inner blanket inside radius	-	2.8	4.5
Inner blanket outside radius	-	3.0	4.9

Figure 1 is a plot of the midplane toroidal field ripple versus the radius for STARFIRE, for the three cases: (1) non-magnetic blanket, (2) axisymmetric FM blanket, and (3) FM blanket with 0.5 m x 0.5 m penetration. It can be seen that the axisymmetric FM blanket causes insignificant modification to the field ripple. Even for the case with penetrations, the ripple over the plasma region is very modest. Similar results were obtained for studies made on the GA TNS and ETF. Thus, it can be concluded that due to the high level of saturation, the FM blankets have effective permeability close to unity, and therefore do not cause any significant changes to the toroidal field ripple.

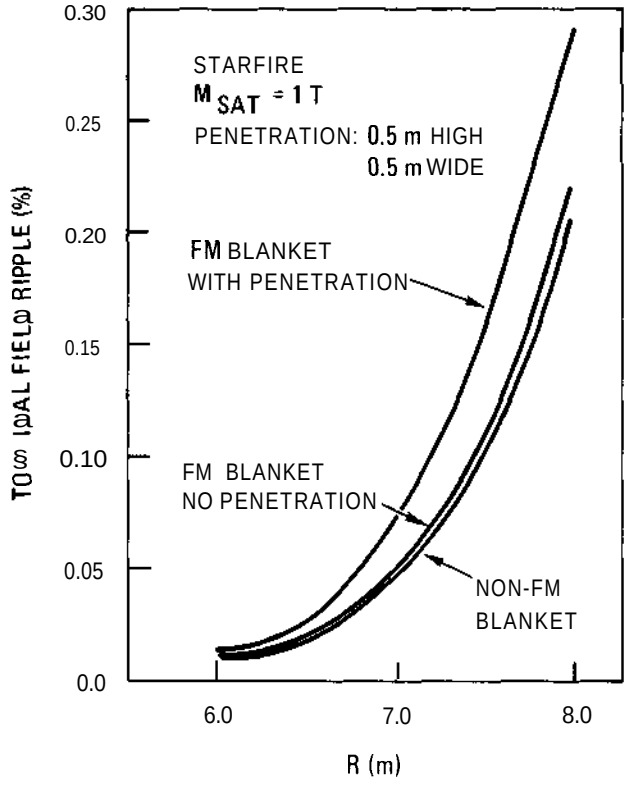

Fig. 1. STARFIRE toroidal field ripple showing the effects of a ferromagnetic blanket with and without penetrations.

Results (Cont'd): Poloidal Field Perturbation

The perturbations in the poloidal fields introduced by the FM blankets have been studied by comparing the poloidal field distributions for the same poloidal current distribution with and without the FM blankets. Because the currents in the poloidal system are much smaller than those of the toroidal system and act on a more open magnetic circuit, the poloidal magnetization cannot change the permeability significantly. This means the parametric coupling between the two systems is very small. Furthermore, it is clear from energy considerations that the permeability reached when building up the final state of currents is independent of the order in which the poloidal and toroidal currents are built up. This is due to the fact that hysteresis effects are negligible at the high level of saturation that the final toroidal

currents generate. All of these expectations were verified during the course of the computational studies. Hysteresis effects were not modeled, however, but it is clear that the minor hysteresis loop normally traversed by the high magnetic field will be very minor indeed if measurable at all.

Figure 2 is the plot of poloidal field perturbation versus the z-coordinate for various radii in the plasma region for STARFIRE. It can be seen that throughout the plasma region field perturbations as high as 3% can be generated by the presence of the FM blankets. However, since in practice all the poloidal coils are actively controlled for the stability and position control of the plasma, such a small perturbation can be easily countered by adjustment of the control parameters.

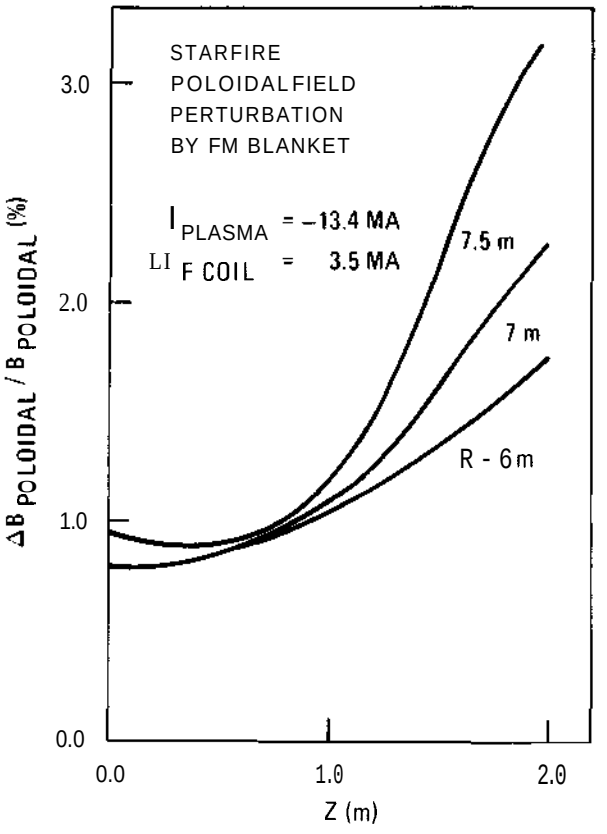

Fig. 2. STARFIRE poloidal field perturbation due to a ferromagnetic blanket.

Another concern about the possible effects on plasma control is introduced by the delay needed by the control field to penetrate the FM blanket. Since the blankets are highly saturated with the effective permeability very close to unity, a FM blanket should behave just like an ordinary metallic blanket in that regard. It must be noted that any such metallic blankets whether FM or not must be partitioned by insulating breaks for the ohmic heating coils to function properly.

Results (Cont'd): Magnetic Loads

The analysis of stationary and transient body forces was limited in most cases to simple cylindrical structures. Two methods were used, both of which utilized the Maxwell stress tensor. An option in the IRON program permits the computation of all force components in a body of somewhat arbitrary but analytically definable shape through numerical integration over a loosely fitting surface that encloses the magnetic body. A simpler analytical method gives the radial body force and the equivalent external pressure over an infinitely long cylindrical shell. The methods generally agree (for sufficiently long cylinders) within 15-25%. The simple analytical method always gives the higher values. Since the numerical method is much more time consuming, the results that are given in Table 2 have been computed analytically. Thus the forces are somewhat on the pessimistic side.

The table shows that the static pressures amount to only a few atmospheres. Since the forces are directed towards the axis it should be possible to design the blanket modules so that a self-supporting "keystoned" structure is achieved. The wedge-shaped modules will be under compression. Even in the case of an ellipsoidal blanket this should be possible. The STARFIRE design was also analyzed with the IRON program with a mostly ellipsoidal shell and it was found that the average radial body-force density (without the inner wall) amounts to 1.4×10^6 n/m^3 for M = 1 tesla as can be expected from the analytical results.

TABLE 2

Radial Body Forces and Equivalent Inward Pressures at Two Values of M*

	Design					
	GA TNS		ETF		STARFIRE	
Major radius	3.6		5.0		6.92	
On axis toroidal field (T)	5		5.3		5.3	
	Inboard	Outboard	Inboard	Outboard	Inboard	Outboard
Blanket:						
Inside radius (m)	-	4.6	2.8	7.1	4.5	8.6
Outside radius (m)	-	5.6	3.0	8.1	4.9	9.7
Inward pressure (atm)						
M = 0.5 T	-	2.8	2.3	1.9	2.5	2.35
M = 1 T	-	6.4	5.15	4.4	5.5	5.3
Body force (n/m^3)						
M = 0.5 T	-	0.31×10^6	1.3×10^6	0.21×10^6	0.7×10^6	0.2×10^6
M = 1 T	-	0.7×10^6	2.7×10^6	0.46×10^6	1.5×10^6	0.44×10^6

*M = saturation magnetization times packing factor.

Figure 3 shows a series of analytically computed equivalent magnetic pressures as a function of magnetization times packing factor. This product was chosen as the argument because in the reactor blanket which serves both for breeding and energy conversion, a large fraction of the volume is occupied by the breeding materials and coolant flow channels, and the FM material only occupies typically 10-20% of the volume. The low packing factor effectively reduces the magnetic loading on the blanket.

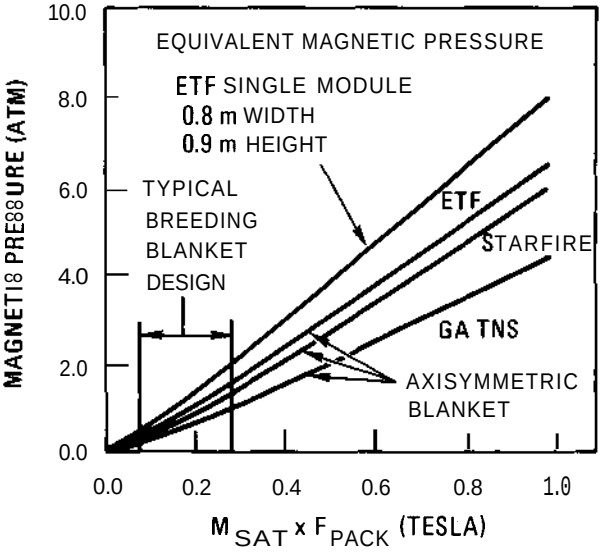

Fig. 3. Magnetic loading on the ferromagnetic blankets for the GA TNS, STARFIRE and ETF

With regard to the transient loads generated on the blankets due to plasma disruption, a FM blanket should behave almost the same as compared to a non-FM blanket.

1.1.5 References

1. S. N. Rosenwasser, et al., "The Application of Martensitic Stainless Steels in Long Lifetime Fusion First Wall/ Blanket," paper presented at the First Topical Meeting on Fusion Reactor Materials, Bal Harbour, Florida (1979).

2. "GA TNS Project, Status Report for FY-78," General Atomic Report GA-A15100, Vol. V (1978).

3. P. H. Sager, "Design Considerations for the Fusion Engineering Test Facility," paper to be presented at a Symposium on Engineering Problems of Fusion Research to be held in San Francisco, November 13-16, 1979.

4. C. C. Baker, et al., "STARFIRE - Commercial Tokamak Power Plant Overview," paper to be presented at a Symposium on Engineering Problems of Fusion Research to be held in San Francisco, November 13-16, 1979.

5. A. Armstrong, et al., "New Developments in the Magnet Design Computer Program GFUN3D," in Proc. of the Fifth International Conference on Magnet Technology, Roma, Italy, April 1975.

2. TEST MATRICES AND TEST METHODS DEVELOPMENT

An important part of the alloy development effort is the definition of test matrices and development of test methods. The alloy development strategy will proceed through stages requiring tests of generally increasing difficulty and complexity.

1. Scoping tests will be used to make relative judgments between materials and metallurgical conditions and to identify critical properties. Such tests, which will be used where large numbers of variables are involved, must be rapid, simple, and decisive.

2. Developmental tests will be used for optimization of the Prime Candidate Alloys. They will be broader and more extensive than the scoping tests. In-reactor testing will be an important part of this work.

3. Engineering property tests will be devised to provide the broad data base needed for reactor design.

2.1 APPLICATION OF THE ELECTROPOTENTIAL TECHNIQUE TO J-INTEGRAL MEASUREMENTS - F. H. Huang, B. A. Chin, and G. L. Wire (Hanford Engineering Development Laboratory).

2.1.1 ADIP Task

ADIP Task 1.B.5.1 "Development Specimens and Test Methods."

2.1.2 Objective

The objective of this work is to evaluate the use of the electropotential technique in obtaining single specimens J-integral fracture toughness measurements. This technique can reduce the large number of specimens needed for a conventional multi-specimen R-curve method and hence reduce the irradiation space required for a given data set. The ultimate goal is to characterize the fracture behavior of ferritics to establish their viability as fusion first wall materials.

2.1.3 Summary

The electropotential technique has been applied to develop single specimen J-integral measurement capability. Calibration curves for voltage change versus crack extension have been obtained at room temperature. Using these calibration curves, J versus Aa curves were generated at room temperature from single specimens of A286 and HT9. These curves compare favorably with multiple specimen results on the same materials. Based on these encouraging results, irradiation test matrices can be formulated to provide approximately five times as many fracture toughness measurements for a given test volume than with the multiple specimen technique.

2.1.4 Progress and Status

2.1.4.1 Experimental Technique

Test specimens were sectioned from a hot rolled 12.7 mm (0.5 inch) A286 bar stock and 1.62 mm (0.06 inch) HT9 sheet stock. The sheet stock was prepared by forging and subsequent rolling from 33.3 mm OD starting stock. The schematic diagram of the A286 miniature compact specimen (0.12 inch thick) is shown in Fig. 2.1.1(a). The HT9 specimen cross section

size is a 75% proportional reduction from Fig. 2.1.1. After machining, the A286 test specimens were aged at 720°C for 16 hours, and the HT9 specimens were solution-treated at 1038°C for 1 minute and subsequently aged at 760°C for one-half hour. It is not anticipated that this will be the reference thermomechanical treatment (TMT) for HT9 use in fusion applications. Prior to fracture testing, all test specimens were fatigue precracked using a conventional servo-hydraulic MTS system. The precrack length was 1.6 mm and the maximum stress intensity factor was 28 MPa $\sqrt{m}$.

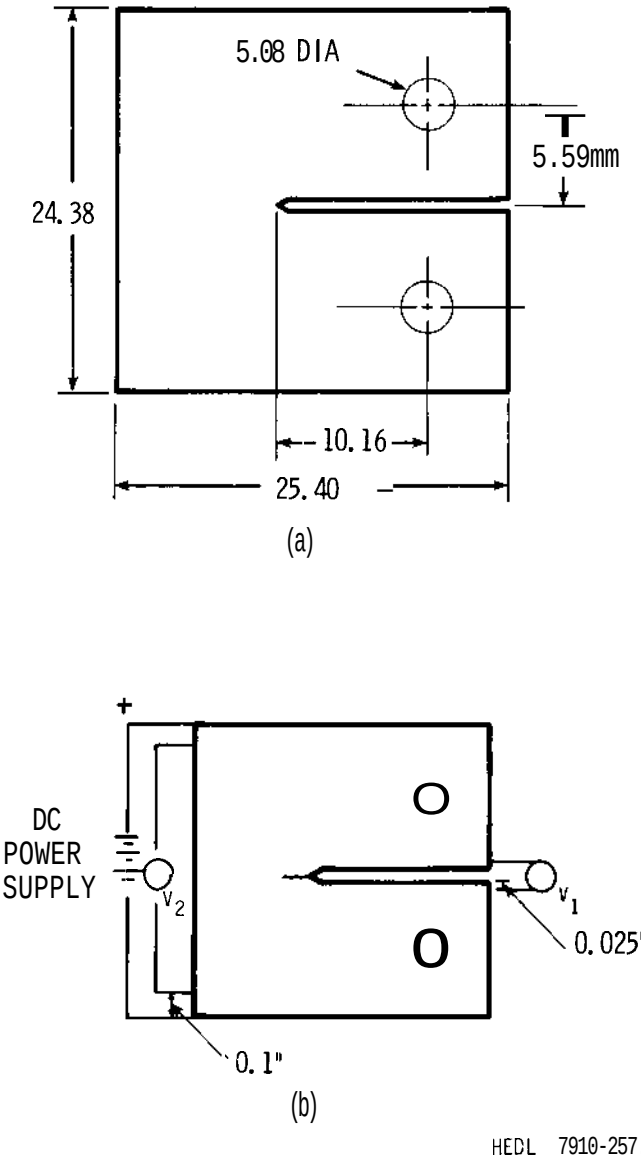

Fig. 2.1.1: (a) Compact tension test specimen of A286; (b) schematic drawing of Electric Potential Technique.

Fracture toughness tests were performed using an Instron testing machine. The details of the technique utilized to construct multiple specimen J-integral curves on the miniature specimens are given in Reference 1. Briefly, load and load-line displacement are recorded on a x - y recorder during specimen loading. After the specimen displacement has reached the desired level, the specimen is unloaded and heated to 538°C for one hour to heat tint the crack area. Fracture of the specimen is completed at room temperature and crack lengths are measured optically using a traveling microscope.

The electropotential technique was applied here to obtain continuous crack length measurements during each test. The theory of this technique is described in References 2 and 3. The current input and potential measurement leads were positioned as in Fig. 2.1.1(b). Crack extension increases the resistance near the crack and hence produces increases in V_1. The lead positions were chosen to give good sensitivity (large changes in V_1) and reproducibility, based on resistance paper mockups of the specimen lead configuration. The voltage V_2 from the crack was measured to account for possible resistivity changes in the specimen. During the actual tests, a constant DC current of 15 amps was applied across the specimens. V_1 and V_2 were recorded using a microvoltmeter.

The values of J were calculated from load versus load-line displacement curves using the following equation.[4]

$$J = \frac{2A}{Bb}$$

where A is the area under load versus load-line displacement curve, B is specimen thickness, and b is unbroken ligament size. Measurement of crack extension was obtained by measuring the maximum distance from the fatigue crack mark to the end of the heat tint mark, Fig. 2.1.2. On the plot of J versus crack extension Aa, the J_{1c} values are found by construction as the value of the intersection of line $2\sigma_{flow}$ x Aa, and the least squares fit line through all points of J versus Aa where $\sigma_{flow} = a_{ys} + a_{uts}$.

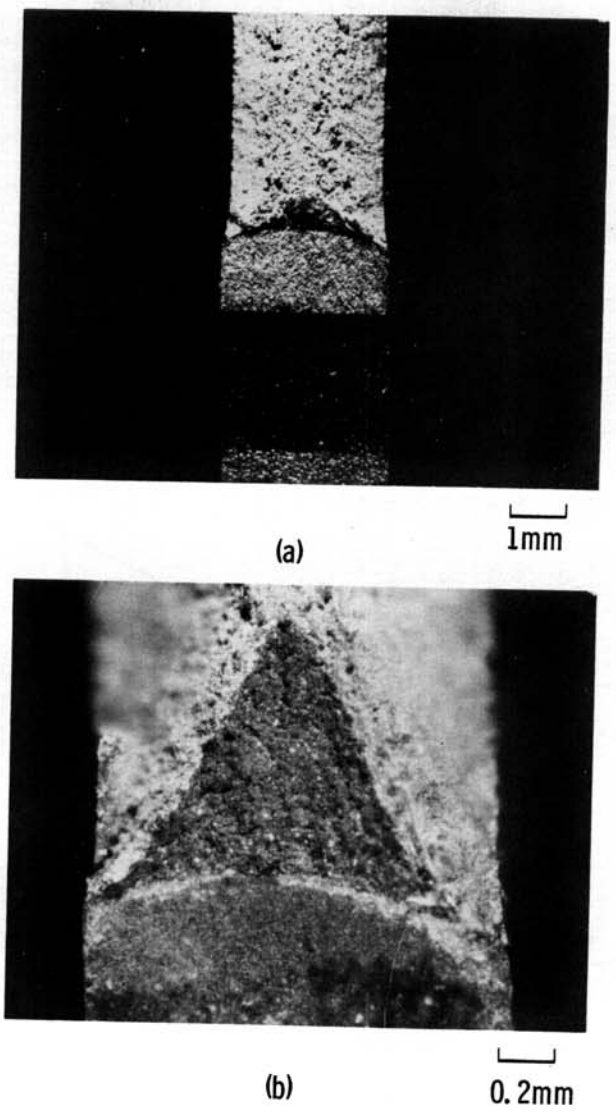

Fig. 2.1.2: Crack extension as revealed by heat tinting for (a) A286 (b) HT9.

2.1.4.2 Results and Discussions

Typical potential changes observed during fracture tests on A286 are shown in Fig. 2.1.3. The potential changes are plotted against the load-line displacement to provide a measure of crack extension versus sample extension. The voltage curves for this material increase smoothly with load line displacement as might be expected for crack growth in a ductile austenitic material at low temperature. The dimensionless ratio V_1/V_{1_o}, where V_{1o} is the voltage measured for the initial crack length after precracking,

was used as a parameter to correlate with crack extension. This ratio should be material property independent so that calibration established for a given specimen geometry should be valid for other composition and temperatures, etc. Of course, this assumption will be tested in detail as this work progresses.

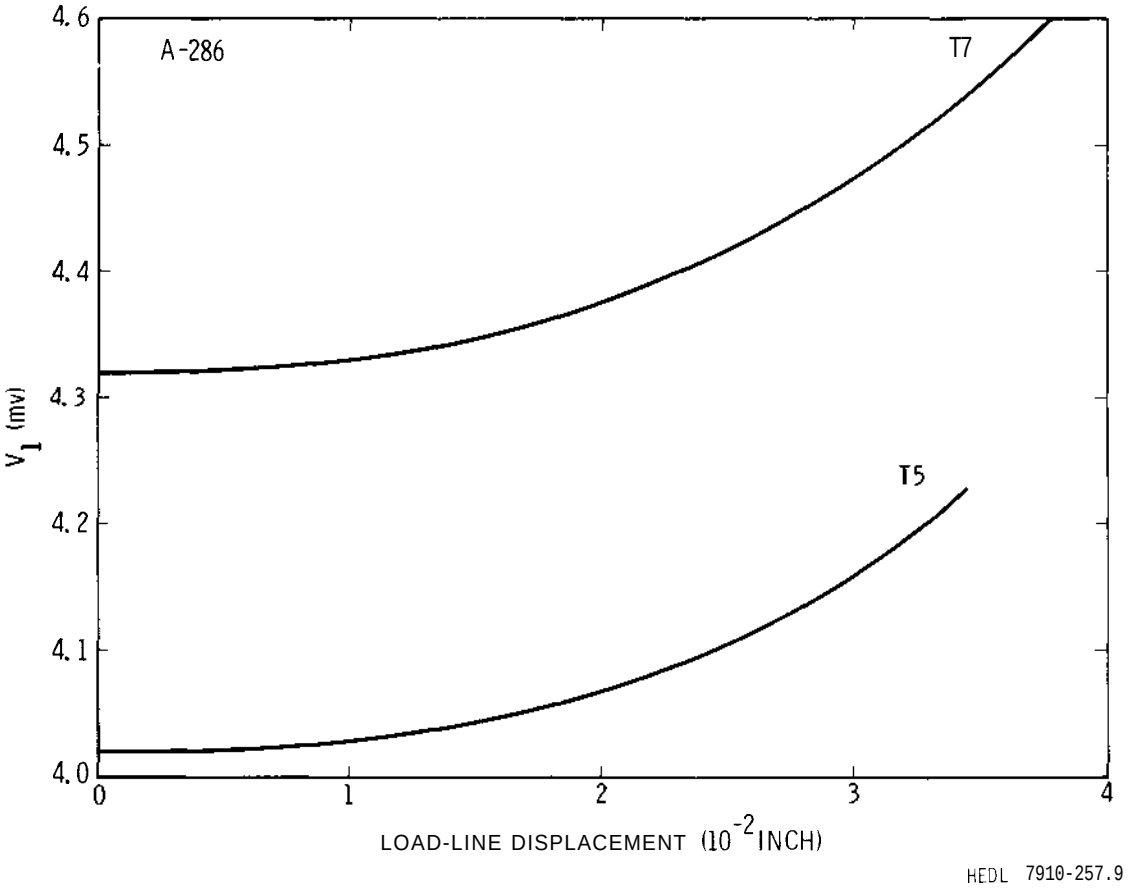

Fig. 2.1.3: Electrical potential V_1 versus load-line displacement for A286.

The calibration for tests done on A286 are shown in Fig. 2.1.4. Only three tests were done on this material with the goal of establishing feasibility of the method by linking to existing J-integral results.[1] A straight line fit to the curve was used for simplicity and emphasis was placed on the region where direct optical crack lengths measurements were available. Detailed calibration curves obtained for HT9 will be discussed later.

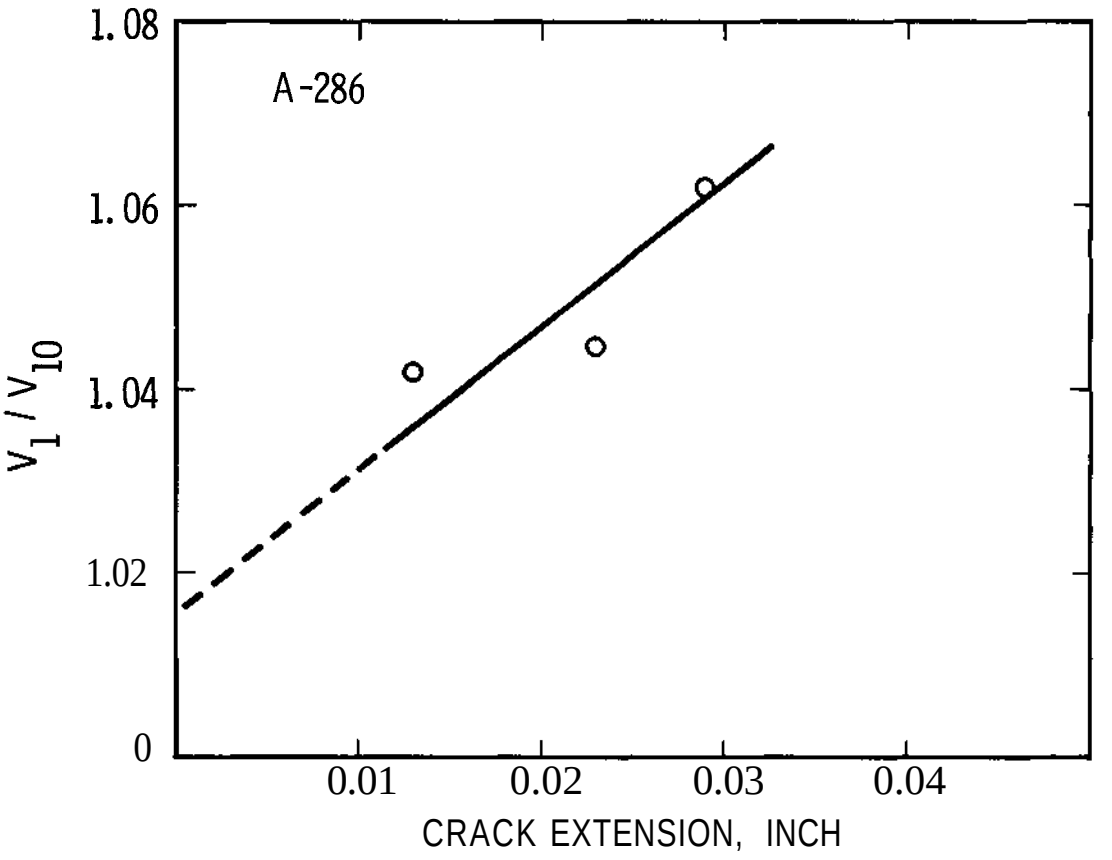

Fig. 2.1.4: Electrical potential calibration curve for A286.

The major point to be made with the A286 data is that using the calibration and electropotential measurements for a single specimen, a J versus Aa could be derived. Fig. 2.1.5 shows a comparison of the multiple specimen plot with the electropotential measurements. The electropotential results are within better than 10% of the overall R curve based on all specimens tested and within 2% of the values for the three specimens actually used for the calibration. The curve from the electropotential measurement was extrapolated back to the crack blunting line to estimate the J_{1c}, and as shown in Fig. 2.1.5, agreement is very good. This result proved experimental feasibility for the technique, and the decision was made to obtain a detailed set of data on a ferritic material to provide a stronger test of the technique on materials where fracture properties are of greatest concern for potential first wall applications.

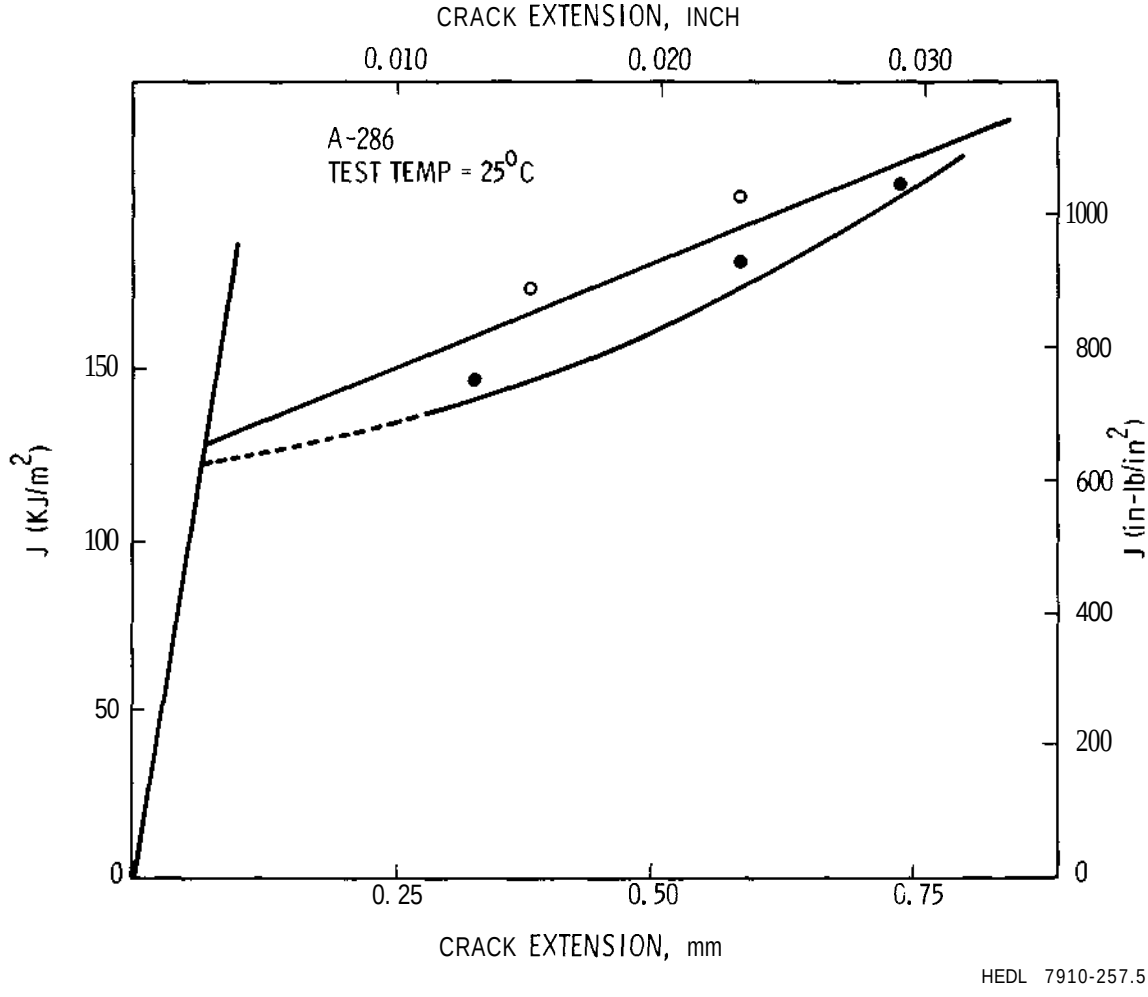

Fig. 2.1.5: J versus Aa tested at 25°C for 3 mm thick A286 specimens. The lower curve was obtained through the use of the calibration curve in Fig. 2.1.4.

Fifteen miniature specimens of HT9 were tested to obtain a complete calibration curve correlating the crack extension to electric potential increase. Three nondimensional ratios V_1/V_{1_o}, V_1/V_2 and $(V_1/V_2)/(V_{1_o}/V_{2_o})$ were compared in correlating crack extensions and voltage measurements. Because of relatively larger scatter, V_1/V_2 was not found useful. There was little difference between V_1/V_{1_o} or $(V_1/V_2)/(V_{1_o}/V_{2_o})$ as to the quality obtained. Hence, the former was selected for the present as it would require fewer leads attached and would be simpler for future in-cell testing.

The detailed calibration curve obtained for HT9 is shown in Fig. 2.1.6. The shape of the curve and magnitude of the voltage ratio change are in

qualitative agreement with theory. [21] However, one feature of the present result was unexpected--the fact that the curve does not extrapolate smoothly to a $V_1/V_{1_o} = 1.0$ from higher crack extensions. This proved to be a highly troublesome point as it was difficult to obtain low crack extension data (where there was an apparent change in slope) on HT9 due to a tendency for sudden crack extension in the material. Some data were obtained at low crack extension on a slightly different TMT of HT9; the authors feel that it must be established that this data can be used along with data from the reference TMT. Further experimental and theoretical work is planned to describe the low crack extension region, and emphasis here will be placed on the correlation for crack extension above 0.5 mm.

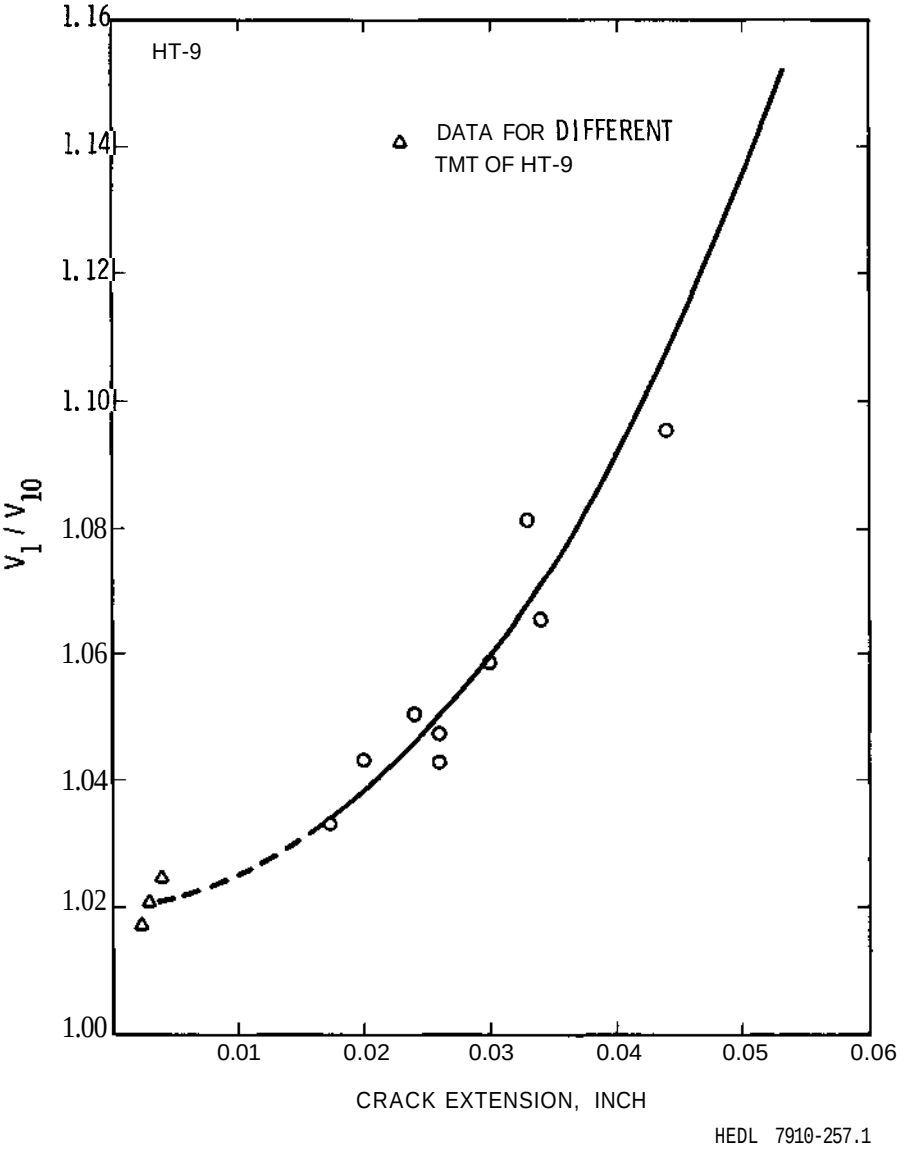

Fig. 2.1.6: Electrical potential calibration curve for HT9.

The nature of the crack extension process in the ferritic is less uniform than in A286, as might be expected at this temperature. The electropotential technique is ideally suited to show the variety of behavior observed. Plots showing two different modes of behavior are shown in Fig. 2.1.7. The sharp potential increase on curve HX 19 resulted from crack extension as reflected by the load drop for the same specimen shown in Fig. 2.1.8. The variation of crack extension rate in test specimens may be due to scatter in fracture toughness among test specimens in the brittle-ductile transition region. The electropotential technique is ideally suited to detect these effects.

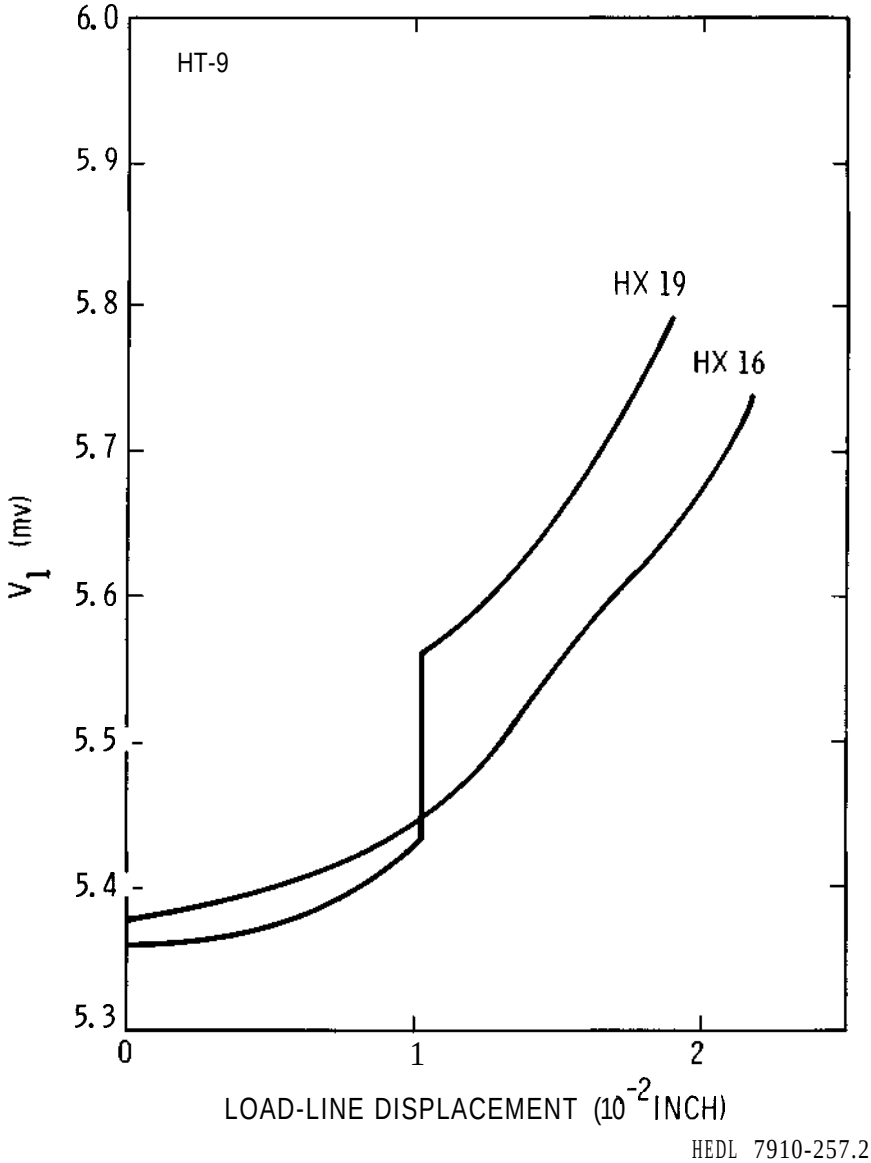

Fig. 2.1.7: Electrical potential V_1 versus load-line displacement for HT9.

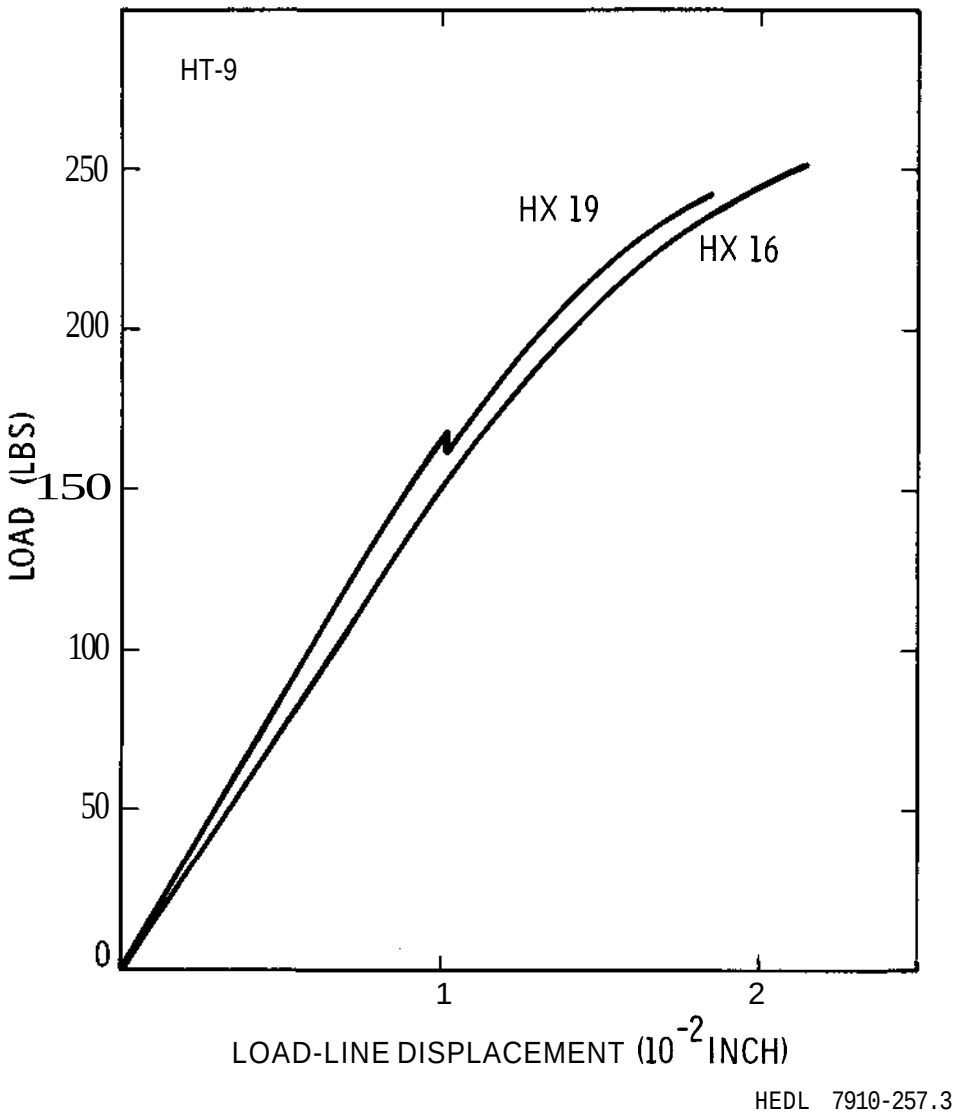

Fig. 2.1.8: Load versus load-line displacement for HT9.

The multiple specimen J-integral curve for HT9 is compared in Fig. 2.1.9 with J versus Aa curves derived for single specimens using the electropotential technique. In this plot, no results from specimens exhibiting load drops were included. The dotted lines below 0.5 mm crack extension reflect current uncertainty in the calibration at low crack extension. However, the J versus Aa curves are in good agreement with the multiple specimen technique above 0.5 mm crack extension, and the scatter between the electropotential J - Aa curves merely reflects the specimen-to-specimen variation in the J-integral value (±∿10%). It should be noted that once

detailed calibration data are obtained below 0.5 mm crack extension, the electropotential method will provide detailed J - Aa data at low crack extension even if fast cracking occurs. The multispecimen method, in contrast, would require an untenably large number of specimens for irradiation testing.

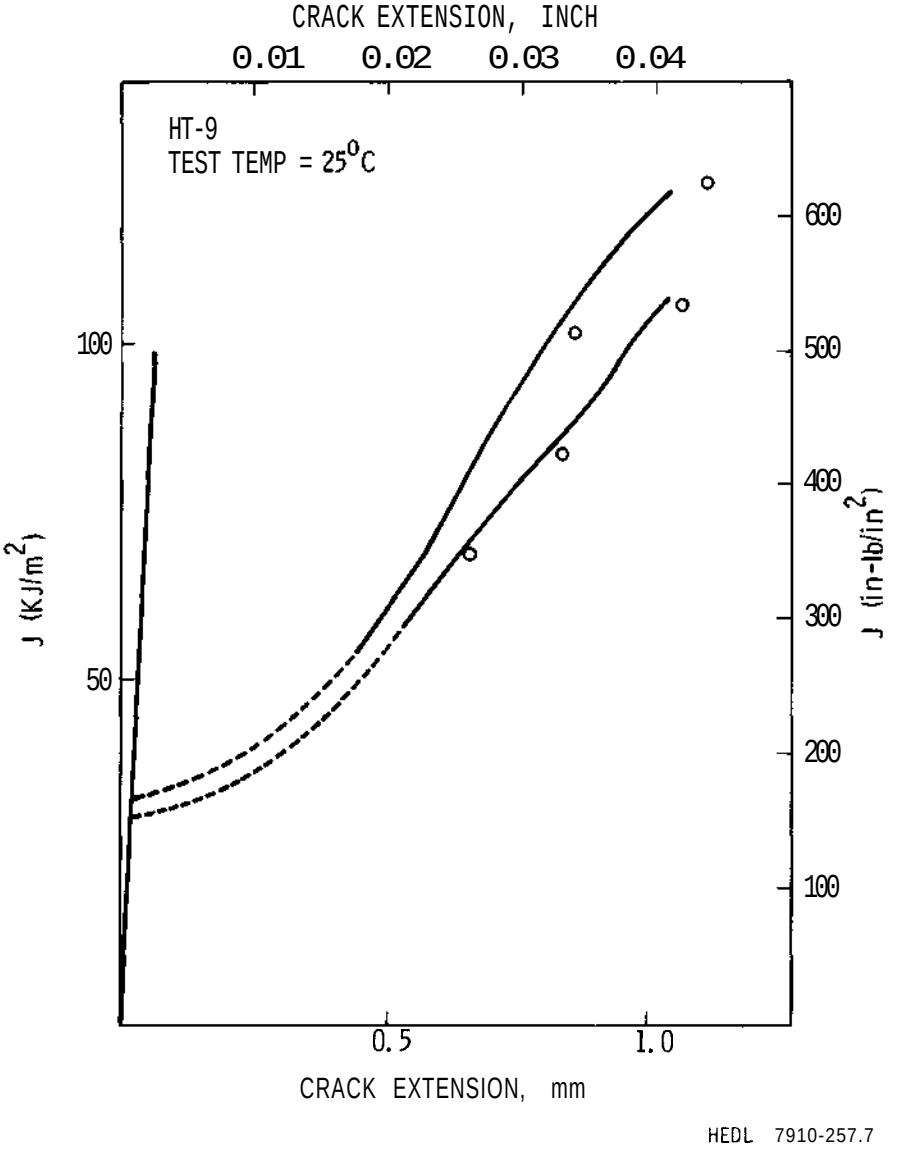

Fig. 2.1.9: J versus Aa tested at 25°C for 1.5 mm thick HT9 specimens. The curves were obtained through the use of the calibration curve in Figure 6.

2.1.5 Conclusions

1. The test results of fracture toughness tests on A286 and HT9 at room temperature using the single specimen electropotential technique agree to within ±5% with those obtained from the multiple-specimen method.

2. The electropotential technique allows instantaneous detection of crack extension rate, and hence can provide for example crack initiation and arrest data not available from post-test crack measurements.

3. The authors feel that these initial tests prove that the single specimen J-integral measurements using the electropotential technique are feasible and irradiation test matrices for fusion first wall applications should be planned accordingly.

2.1.5.1 Future Work

Fracture toughness tests at room temperature on HT9 using the electrical potential technique will continue to characterize the low crack extension region. Tests at elevated temperature will follow. A circular compact tension specimen will be designed for efficient stacking in EBR-II, and emphasis will be placed on calibrating the electropotential technique for this geometry. A variety of ferritic compositions and thermomechanical treatments will be studied to ensure that any potential material variability effects on calibration are well documented prior to irradiation of these specimens.

2.1.6 References

1. F. H. Huang and G. L. Wire, "Techniques Developed for Elevated Temperature Fracture Toughness Testing of Irradiated Materials in Thin Sections," to be published in *J. of Eng. Materials and Technol.*, 1979.

2. W. F. Brown and J. E. Srawley, *Plane Strain Crack Toughness Testing of High Strength Metallic Materials*, STP410, American Society for Testing and Materials, 1967.

3. G. H. Aronson and R. 0. Ritchie, "Optimization of the Electrical Potential Technique for Crack Growth Monitoring in Compact Test Pieces Using Finite Element Analysis," *J. of Testing and Evaluation,* J TEVA Vol. 7, No. 4, pp. 208, 1979.

4. J. R. Rice, P. C. Paris, and J. G. Merkle, *Progress in Flow Growth and Fracture Toughness Testing*, STP536, American Society for Testing and Materials, pp 231 (1973).

2.2 DEVELOPMENT OF THE MINIATURE FATIGUE CRACK GROWTH MACHINE - D. A. Mervyn, M. M. Paxton, and A. M. Ermi (Hanford Engineering Development Laboratory).

2.2.1 ADIP Task

Task I.A.2, define test matrices and test procedures.

2.2.2 Objective

Miniature specimen technology has been developed to provide the high volume, low cost postirradiation testing capabilities necessary to characterize the fatigue crack growth behavior of first wall materials. This technology is based on a miniature, weldable center-cracked-tension specimen cyclicly tested with a fatigue test machine designed for in-cell operation.

2.2.3 Summary

A baseline study of Path A, Path B, and Path D alloys has been initiated. Results of ambient temperature fatigue crack growth testing on 20% CW 316 SS, alloys B1, B2, B3, B4, B6 and HT-9 are presented. The miniature fatigue machine designed as a prototype for high volume low cost, in-cell operation was used for testing these alloys. Elevated temperature tests performed on Path A 316 SS at 260°C and 595°C are compared with results of other investigators.

2.2.4 Progress and Status

2.2.4.1 Introduction

Given the inevitable presence of flaws in fabricated sheet structures, the fatigue crack propagation (FCP) behavior of a fusion first wall material is a primary design factor for any cyclically operating magnetic fusion reactor. Therefore, the effect of irradiation on the FCP behavior of candidate first wall materials must be characterized. Currently, an insufficient amount of data exists from which to draw design criteria.

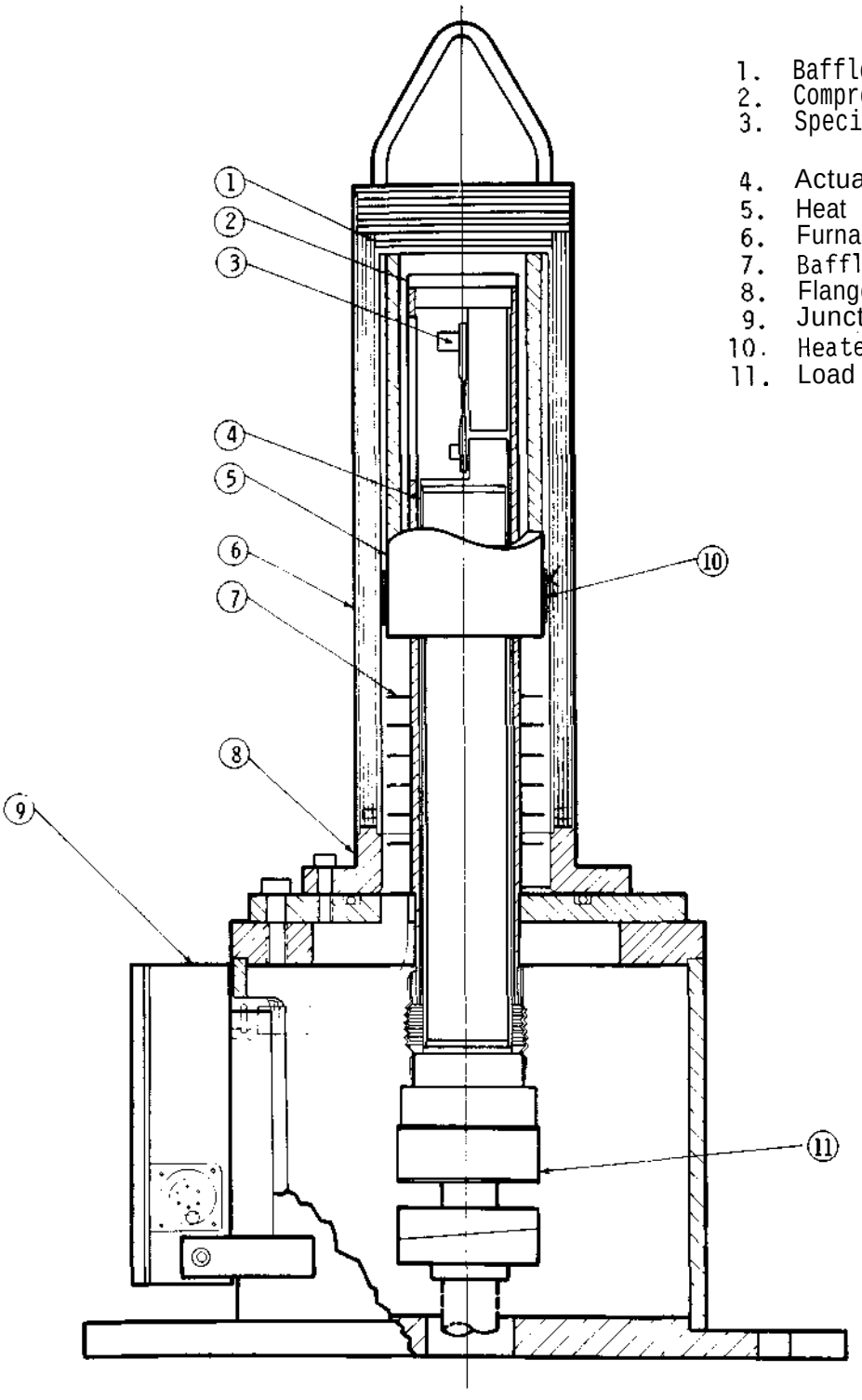

Figure 2.2.1: Miniature Fatigue Test Machine

Miniature specimen technology designed for high volume, low cost postirradiation testing has been developed to provide the necessary volume of data. A miniature weldable center-cracked-tension (CCT) specimen and electrical potential (e.p.) method of measuring crack growth form the basis of this technology. The CCT specimen and e.p. technique were described in a previous quarterly.[1] Ambient and elevated temperature data were also reported.

Using a miniature fatigue test machine designed for in-cell operation, a baseline study on several Path A, B, and D candidate alloys has been initiated. Ambient temperature data is reported as well as elevated temperature results from Path A 316 SS in helium and air.

2.2.4.2 Experimental Technique

Ambient temperature testing was performed in air on 20% cold worked (CW) 316 SS (Path A reference alloy), nickel base alloys B1, B2, B3, B4 and B6 (Path B), and ferritic alloy HT-9 (Path D) using the miniature CCT specimen and in-cell prototypic test machine. Alloy compositions and heat treatments are described in Table 2.2.1 while test conditions are detailed in Table 2.2.2.

To compare test results generated using the miniature specimen technology with conventional techniques, elevated temperature tests were performed on the reference alloy, 20% CW 316 SS, in air at 25°C and 595°C and in helium at 260°C.

Crack length measurements were made using the electrical potential technique adapted to the miniature specimen, described previously.[2] Occasional visual measurements of crack length were made with a traveling microscope to confirm the e.p. measurements.

Tests were performed with the miniature fatigue machine designed for the CCT specimen, Figure 2.2.1. The testing system consists of three modules; a servohydraulic actuating component, a furnace and environmental control unit, and an electronic control and data acquisition system.

Table 2.2.1 Alloy Composition and Condition

Alloy	Condition	Nominal Composition Wt% Fe	Ni	Cr	Mo	Nb	Ti	Al	Mn	C
Path A										
316SS	20% Cold Worked	Bal	13	18	2.5	-	0.5	-	1.9	0.05
Path B										
B1	1025°C/5min/AC(SA) +50% CW	Bal	25	10	1	-	3	1.5	1	0.03
B2	SA + 50% CW	Bal	40	12	3	-	1.5	1.5	0.2	0.03
B3	SA + 50% CW	Bal	30	12	-	2	2	0.5	1	0.03
B4	SA + 50% CW	Bal	40	12	-	3	1.8	0.3	0.2	0.03
B6	SA + 50% CW	Bal	75	15	-	1	2.5	1.5	0.2	0.03
Path D						W	V	Si		
HT-9	1050°C/30min/AC +3.5 Hr/780°C/AC	Bal	.50	11.3	.85	.50	.27	.38	.52	.22

Table 2.2.2 Test Conditions

Alloy	Temp. °C	Maximum Load	Stress Ratio	Cyclic(H_z) Frequency	Waveform	Orientation
Path A						
316SS	25	400	0.05	15	Sine	WR
316SS	260	350	0.05	15	Sine	WR
316SS	595	475	0.05	0.167	Sine	WR
Path B						
B1	25	400	0.05	15	Sine	WR
B2	25	475	0.05	15	Sine	WR
B3	25	400	0.05	15	Sine	WR
B4	25	400	0.05	15	Sine	WR
B6	25	400	0.05	15	Sine	WR
Path D						
HT-9	25	475	0.05	15	Sine	WR

The servohydraulic system consists of the hydraulic actuator, servovalve, and load frame. The test frame and assembly have been optimized for easy in-cell operation. The assembly stands 100cm (39 inch) high and is 36cm (14 inch) in diameter. Specimens are inserted through a window in the compression tube which acts as a fixed support for the specimen.

Elevated temperature testing capabilities are provided by a resistance heating cylindrical furnace which fits over the load frame. Temperature can be controlled to within $\pm 1°C$ across the specimen. A portable vacuum station and inert gas line supply a helium atmosphere to the furnace chamber. The leads used for e.p. crack growth measurements are fed out of the chamber through a porthole to a junction box where they are joined to the data acquisition system.

Load control is exercised through a flat load cell using an MTS feedback controller. The controller interfaces with the data acquisition system through a 16 bit parrallel interface and TTL counter which provides eight digit count accuracy.

The data acquisition system consists of a desk top computer (HP-9845) and digital voltmeter which monitor changes in potential across the specimen through a scanner/multiplexor joined to the specimen probes at the junction box. The data acquisition system has been designed to monitor a number of test stations. Equipped with scanning/multiplexing capabilities, the computer will be able to monitor up to 50 test stations. Individual MTS controllers and TTL counters will allow test conditions at each station to be controlled independently.

By scanning and accessing each individual counter, the computer can be triggered to take e.p. measurements at predesignated count intervals, and therefore, determine the fatigue crack growth as a function of the number of cycles. Since the e.p. measurements are averaged at cued count intervals, the computer can continuously monitor each test without interrupting the load cycle.

On line measurements substantially increase the amount of data which can be accumulated during a test; and test time is reduced. This automized measuring capability will enable postirradiation tests to be

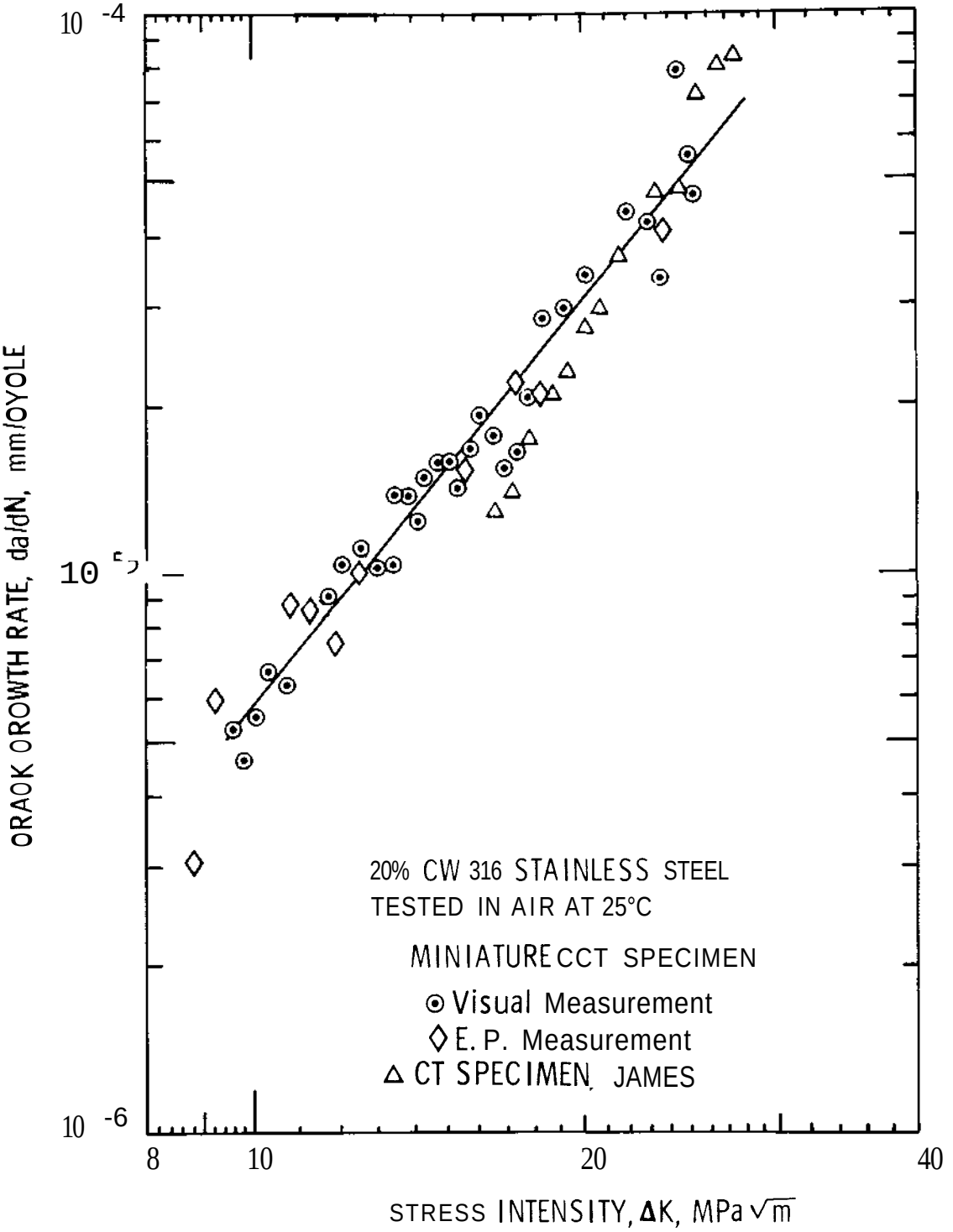

Figure 2.2.2: Comparison of Room Temperature Fatigue Crack Growth Rates for CCT Specimen (e.p. and Visual Measurements), and CT Specimen (Visual), James.[3]

monitored continuously, in-cell,with a high degree of accuracy. Substantial savings in capital investment cost and technical labor are also accrued.

2.2.4.3 Results: Path A

Testing was conducted using the miniature test assembly and data acquisition system. All data was analyzed using a fracture mechanics approach where the crack growth rate (da/dN) is described as a function of the effective stress intensity at the crack tip (ΔK).

Crack growth was monitored both visually and with the e.p. method on the initial Path A 316SS room temperature test. Both visual and e.p. measurements agree with data obtained using conventional test techniques and a CT specimen, James[3], Figure 2.2.2.

Results of the 260°C test in helium are compared with a conventional test, CT specimen, in air[3] in Figure 2.2.3. Although data from the miniature CCT specimen extends into a lower crack growth regime, agreement is excellent in the 10^{-5} to 10^{-4} mm/cycle region. Environment does not appear to effect the crack growth behavior of 316SS at this temperature.

The 593°C test was performed in air for direct comparison with Shahinian,[4] Figure 2.2.4. The single-edge-notched cantilever (SENC) specimen data agrees with the miniature CCT specimen results in the 2×10^{-4} to 5×10^{-4} mm/cycle regime. Further tests will be conducted to extend this region of comparison to a higher crack growth regime.

Results: Path B and D

Preliminary data on the nickel base precipitation hardened Path B alloys in the solution anneal +50% CW condition is summarized in Figure 2.2.5. At room temperature, none of these alloys in the SA + 50% CW conditions exhibit better crack growth behavior than annealled 304 SS. Alloys B3, B2, and B4 exhibit higher crack growth rates than annealled 304 SS, and B1 and B6 approximately the same.

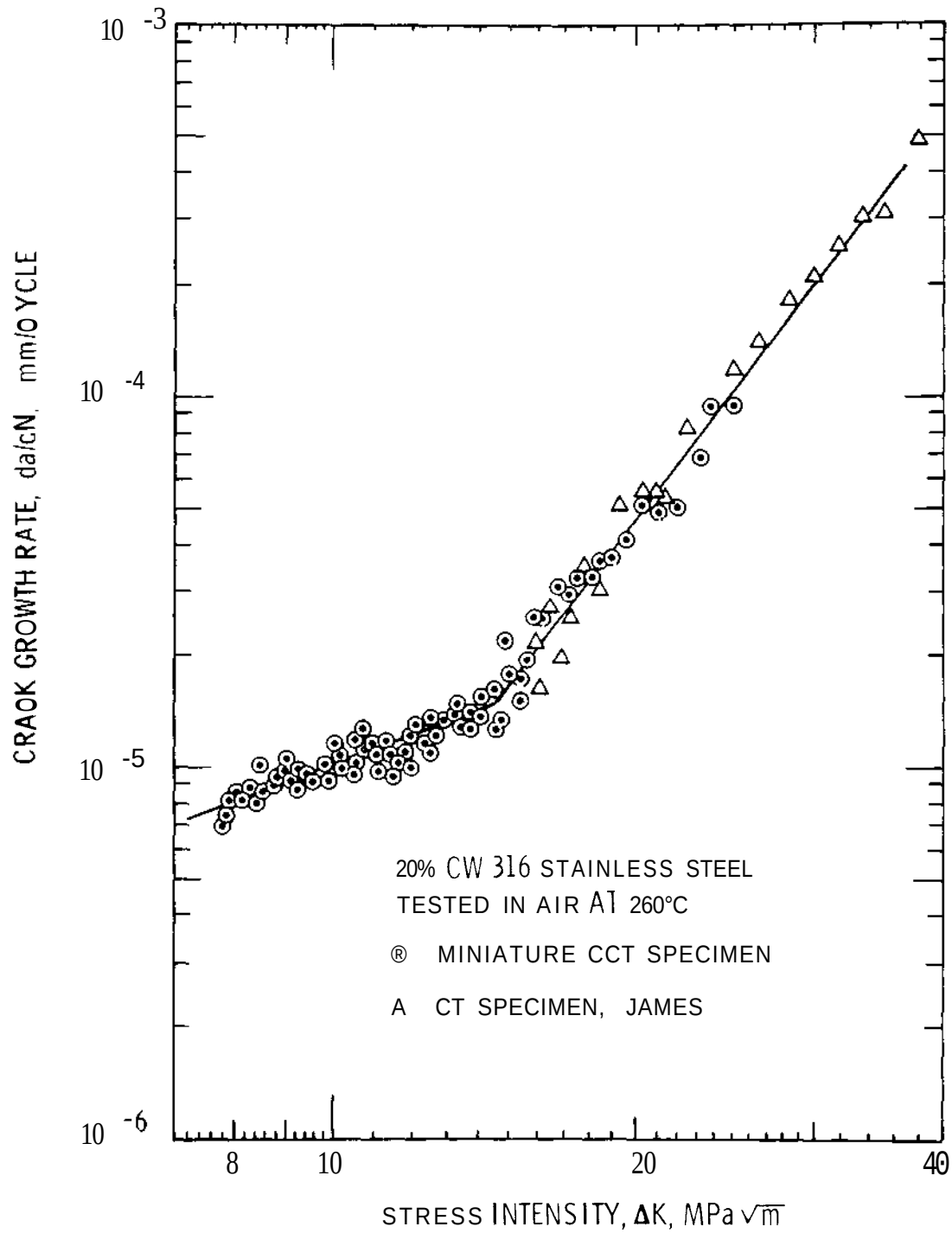

Figure 2.2.3: Comparison of Elevated Temperature Fatigue Crack Growth Rates for CCT Specimen (e.p. Method) and CT Specimen (Visual Method), James.[3]

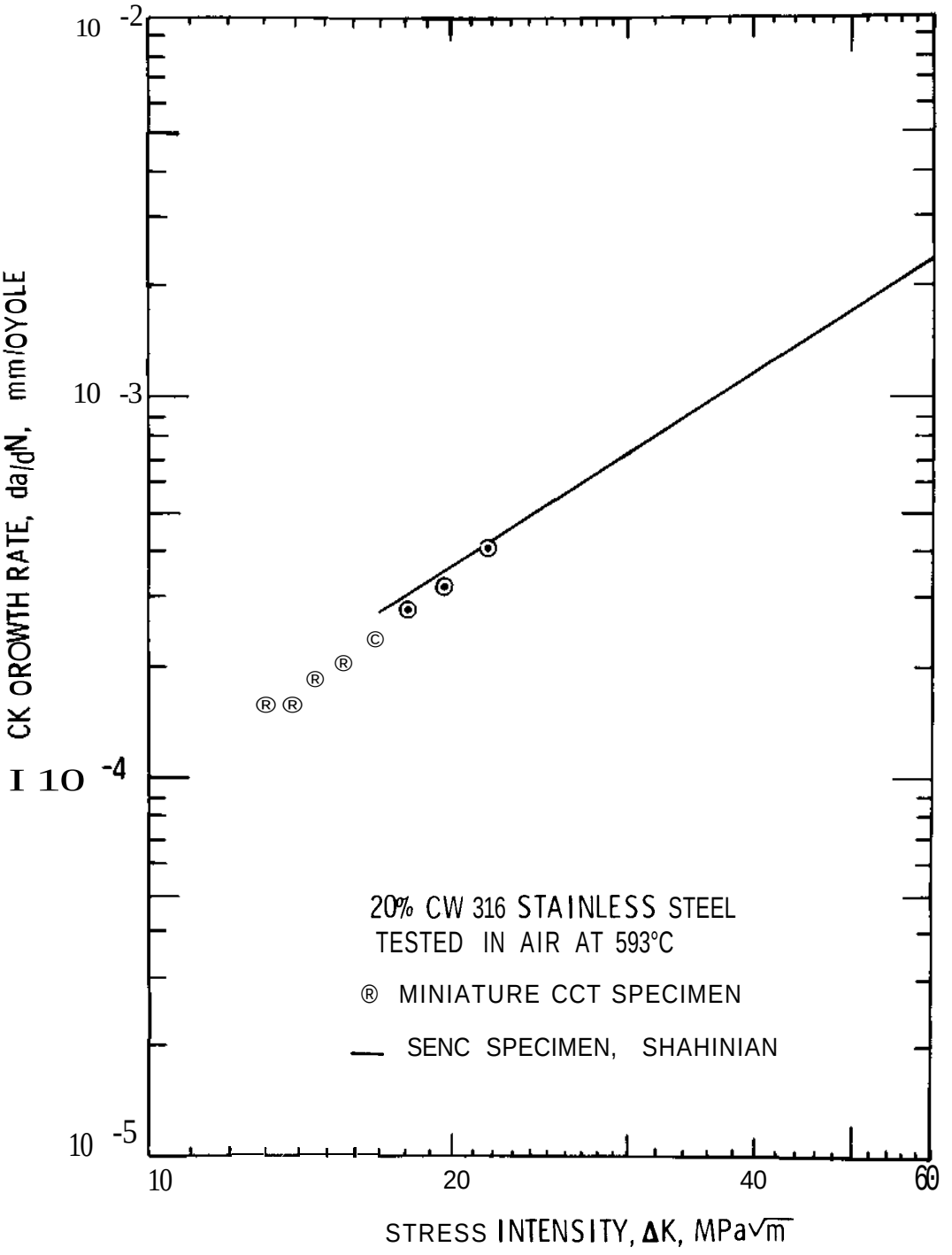

Figure 2.2.4: Comparison of Elevated Temperature Fatigue Crack Growth Rates for CCT Specimen (e.p. Method) and SENC Specimen (Visual Method), Shahinian.[4]

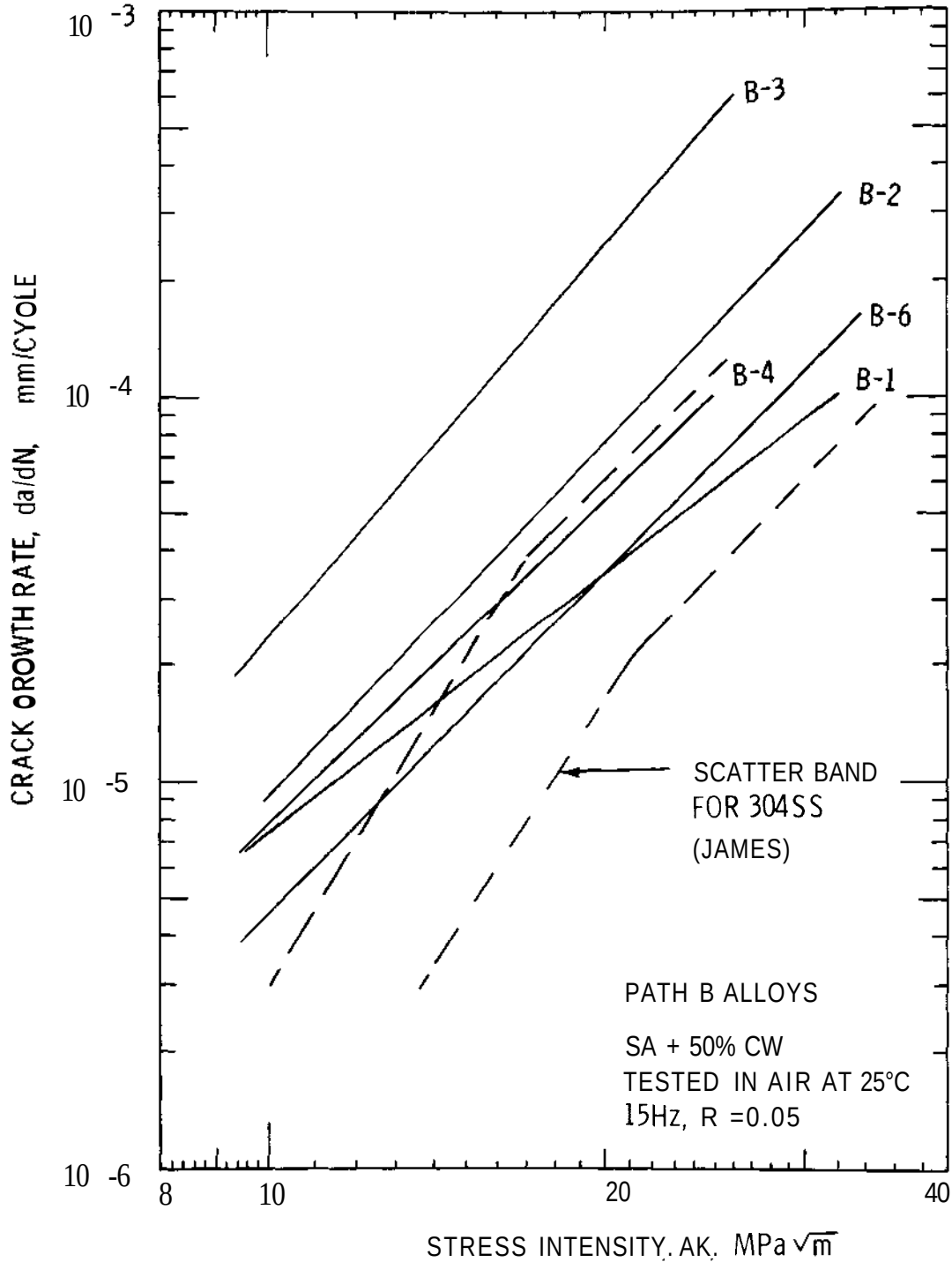

Figure 2.2.5: Comparison of Path B Alloys with 304SS.[1]

When crack growth rate, for a constant ΔK, is plotted as a function of Wt% nickel for these alloys, some unexpected results are obtained, Figure 2.2.6. With the exception of alloy B1, an increase in nickel content appears to enhance the crack propagation resistance for the SA + 50% CW condition. The high fatigue crack growth rate of B3 may be due to phase instabilities encountered during its slow cool down from the solution anneal.

The Path B alloys will be tested at room and elevated temperatures in the solution treated and aged (STA) condition to further investigate the effect of nickel and microstructure on crack propagation resistance. Mills[5] has shown a factor of 2.5 difference between the solution treated and STA conditions of Inconel X718; therefore, the trend observed for the SA + 50% CW condition of the high nickel B alloys may change when they are tested in the STA condition.

Very few crack growth studies have been performed on the high Cr ($\geq$9% Cr) ferritic stainless steels. The preliminary results of this study indicate that at room temperature in the solution annealed and tempered condition, HT-9 exhibits the same crack growth behavior as annealed 304 SS, Figure 2.2.7. The baseline study on the ferritic alloys will be continued. HT-9 will be tested in different heat treated conditions and at elevated temperatures. Nine Cr, 1 Mo steel will also be included in this study of the ferritic alloys.

2.2.5 Conclusion

1. Tests on Path A 316SS have confirmed the accuracy and reliability of the miniature specimen technology in characterizing the FCP behavior of materials at ambient and elevated temperatures.

2. Results of this investigation indicate that nickel concentration in the Path B alloys may have an effect on their fatigue crack propagation resistance.

3. The fatigue crack propagation behavior of ferritic alloy HT-9 is similar to that of 304SS at room temperature.

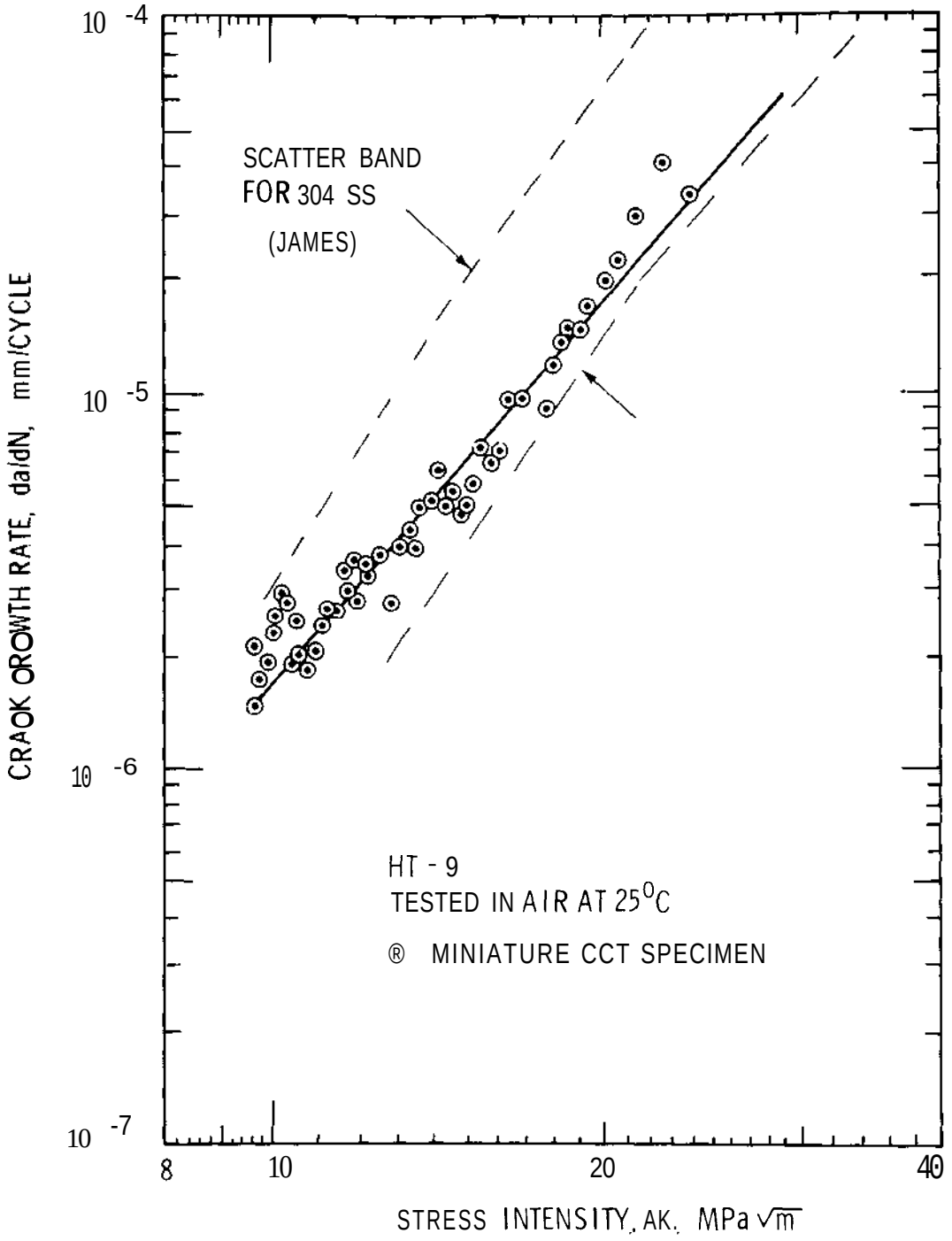

Figure 2.2.6: Crack Growth Rate as a Function of Wt% Nickel for Path B Alloys, SA +50% CW.

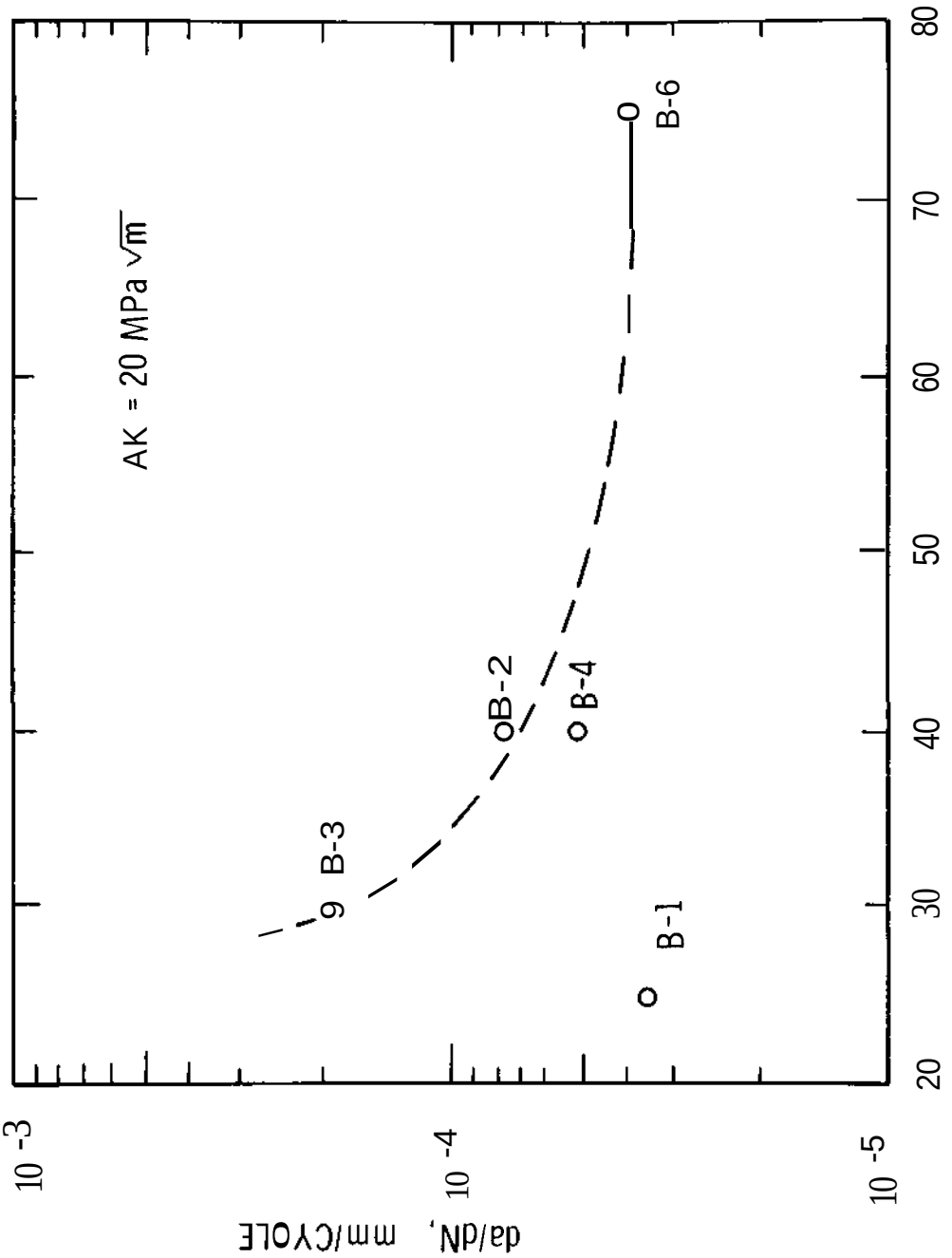

2.2.7: Comparison of HT-9 with 304SS.*

2.2.6 Future Work

The baseline study of candidate first wall materials will be extended to include other heat treated conditions and elevated temperature testing of Path A, B, and D alloys. This will include further investigation into the role of nickel content and microstructure in determining the FCP behavior of the Path B alloys. Testing will also be iniated on other Path C, titanium alloys; Path D, 9 Cr, 1 Mo steel; and Path A, PCA, alloys.

2.2.7 References

1. D. A. Mervyn, "Elevated Temperature Fatigue Crack Growth Testing Using Miniature Specimen Technique," ADIP Quarterly Progress Report, June 30, 1979.
2. J. L. Straalsund and D. A. Mervyn, "Adaptation of Electrical Potential Technique to Measure Fatigue Crack Growth," ADIP Quarterly Progress Report, December 31, 1978.
3. L. A. James, "Fatigue-Crack Growth in 20% Cold-Worked Type 316 Stainless Steel at Elevated Temperatures," Nuclear Technology, Vol. 16, October 1972.
4. P. Shahinian, "Creep-Fatigue Crack Propagation in Austenitic Stainless Steels," Trans. ASME, J. Pressure Vessel Technology, Vol. 98, 1976.
5. W. J. Mills, L. A. James, "Effect of Heat-Treatment on Elevated Temperature Fatigue-Crack Growth Behavior of Two Heats of Alloy 718," ASME Paper 78-WA/PVP-3.

2.3 ELEVATED TEMPERATURE FATIGUE CRACK PROPAGATION TESTING OF 2.54 nun THICK CT SPECIMENS -D. J. Michel and H. H. Smith (Naval Research Laboratory)

2.3.1 ADIP Task

Task I.B.I, Fatigue Crack Growth in Austenitic Alloys(Path A).

2.3.2 Objective

Experiments were performed to investigate the elevated temperature fatigue crack propagation performance of 2.54 mm thick compact tension specimens intended for post-irradiation studies of first wall materials.

2.3.3 Summary

Elevated temperature fatigue crack propagation tests were conducted to determine the nature of specimen thickness effects in preparation for postirradiation testing. The results show that the crack propagation rate in 2.54 mm (0.10 in.) thick Type 316 stainless steel was in agreement with results produced by conventional crack propagation specimens at 593°C.

2.3.4 Progress and Status

2.3.4.1 Introduction

The current magnetic fusion reactor design concepts indicate that the reactor will operate in a cyclic mode during its lifetime. Therefore, it is recognized that fatigue crack propagation (FCP) of first wall materials may be the design limiting factor in fusion systems. To assess the effects of neutron displacement damage and helium generation on FCP of first wall materials, postirradiation tests will be utilized to characterize selected materials and to establish the design data base. Since a first wall thickness of 2.52 mm (0.10 in.) has been proposed, initial experiments will be aimed toward FCP characterization of materials with this section thickness. This report describes elevated temperature experiments conducted to characterize FCP results from 2.54 mm specimens of Type 316 stainless steel.

2.3.4.2 Experimental Procedures

Testing of 2.54 mm thick compact tension (CT) specimens was performed in air at 593°C for comparison with results from both conventional CT specimens[1] and single-edge-notched (SEN) specimens[2]. Annealed Type 316 stainless steel plate material was utilized in specimen preparation. Details of testing procedures have been previously reported [1,2]. Briefly, the specimens were cycled using a servo-hydraulic test machine at a load ratio of 0.05 and a frequency of 0.17 Hz. The test temperature of 593°C was achieved by induction heating. Crack lengths were visually measured throughout the tests using traveling microscopes.

2.3.4.3 Results

The results obtained for the 2.54 mm thick (0.1 T) specimens are compared with results for conventional (1T and 0.5T) CT and SEN specimens in Fig. 2.3.1. The data for the 0.1T specimens show good agreement with results from both SEN and conventional CT specimens over the da/dN versus ΔK region investigated at 593°C. The results demonstrate that the 0.1T CT specimen will provide reproducible FCP results consistent with conventional CT and SEN specimens.

2.3.5 Conclusion

Fatigue crack popagation data from 2.54 mm (0.10 in) thick Type 316 stainless steel was found to be in agreement with data produced by conventional crack propagation specimens.

2.3.6 Future Work

Pre-irradiation testing of alloys for ORR irradiation in Experiment MFE-3 will be conducted in both air and vacuum environments at temperatures from 350 to 550° C to provide baseline data.

2.3.7 References

1. D. J. Michel, H. H. Smith, and H. E. Watson, "Effect of Hold Time on Elevated Temperature Fatigue Crack Propagation in Fast Neutron Irradiated and Unirradiated Type 316 Stainless Steel," in Structural Materials

for Service at Elevated Temperature in Nuclear Power Generation, A. 0. Schaefer, ed., American Society of Mechanical Engineers, New York, MPC-1, 1975, pp. 167-190.

2. D. J. Michel and H. H. Smith, "Effect of Neutron Irradiatioin on Fatigue Crack Propagation in Type 316 Stainless Steel at 649°C," NRL Memorandum Report 3936, Naval Research Laboratory, Washington, D. C., March 14, 1979.

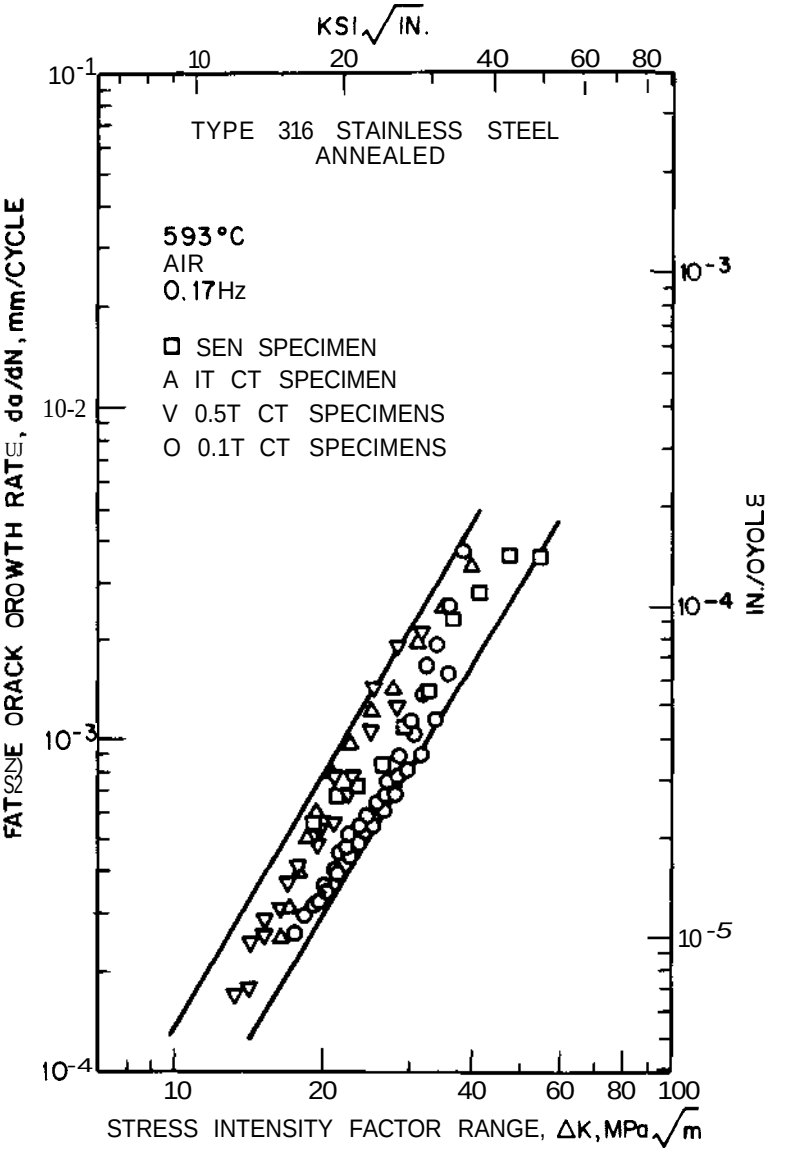

Figure 2.3.1 Comparison of Fatigue Crack Propagation Rates for 316 Stainless Steel for Several Specimen Types.

2.4 DESIGN AND CONSTRUCTION OF IRRADIATION EXPERIMENTS IN THE ORR USING SPECTRAL TAILORING AND REENCAPSULATION - K. Thoms, T. A. Gabriel, B. L. Bishop, R. A. Lillie, J. A. Horak, and M. L. Grossbeck (ORNL)

2.4.1 ADIP Task

ADIP Task I.A.2, Define Test Matrices and Test Procedures.

2.4.2 Objective

The objective of this work is to produce the neutronic, thermal, and mechanical design of experiments for material irradiation in the Oak Ridge Research Reactor (ORR) core. The ORR-MFE-4 experiments will operate with spectral tailoring to control the fast and thermal fluxes and thus the displacement and helium production rates. The capsules are also designed for both discharging specimens and reloading with irradiated specimens several times during the experiment lifetime.

2.4.3 Summary

The design for ORR-MFE-4 is now complete, and parts are being machined. Fine tuning calculations are being made to determine the optimum time for removing the first core piece. Neutronics calculations will continue as dosimetry data become available during the irradiation of ORR-MFE-4. Specimen fabrication is also under way.

2.4.4 Progress and Status

2.4.4.1 Neutronics

The two new 7-group neutron cross-section libraries generated for the VENTURE[1] code have been obtained by using the AMPX[2] code system. These libraries represent a subset of the 218-group Criticality Safety Reference Library (CSRL)[3] or, where necessary, the 227-group CSRL library.[4] The difference between the two libraries involves the weighting spectra used to collapse the fine group cross sections to the broad group cross sections. The weighting spectra were obtained by either including or excluding tantalum and tungsten from 1-D ANISN[1] calculations. Preliminary

comparisons between the new and the old libraries are in progress as a part of our effort to verify the new libraries. The VENTURE calculations obtained with the new libraries indicate only minor changes in fe-effective (about 1 to 2%) and in the neutron flux (about 10%). However, the analyses involving the verification of the new libraries are not complete.

Information on the core configuration anticipated for the first reactor irradiation of the spectral tailoring capsule is currently being gathered. As soon as these data have been finalized, VENTURE calculations will be performed to determine the amount of reactor time required before the first core piece has to be changed and before the first samples are to be removed from the capsule.

2.4.4.2 Fabrication

All components are now being machined; they will be delivered beginning November 1, 1979. Assembly will also begin at that time.

An apparatus for loading specimens for reencapsulation has been designed and agreed upon by the hot-cell operations staff.

2.4.4.3 Specimens

A procedure has been developed for heat treating the Path A Prime Candidate Alloy (PCA)[5] (see also Chap. 3.3 of this report). The alloy is now being rolled into sheet. Drawing and tube drilling are being investigated for the production of PCA tubing to be included in this experiment.

2.4.5 Conclusions

The ORR spectral tailoring experiment is proceeding on schedule. Construction is expected to begin on November 1, 1979, and to be completed in January 1980.

2.4.6 References

1. D. R. Vondy, T. B. Fowler, and G. W. Cunningham, *VENTURE, A Code Block for Solving Multigroup Neutron Problems Applying Fine-Diffusion-Theory Approximations to Neutron Transport*, ORNL-5062 (October 1975).

2. N. M. Greene et al., *AMPX: A Modular Code System for Generating Coupled Multigroup Neutron-Gamma Libraries from ENDF/B*, ORNL/TM-3706 (1976).

3. W. E. Ford, III, C. C. Webster, and R. M. Westgall, *A 218-Group Neutron Cross-Section Library in the AMPX Master Interface Format for Criticality Safety Studies,* ORNL/CSD-TM-4 (July 1976).

4. B. R. Diggs, W. E. Ford, III, and C. C. Webster, *Generation of ENDF/B-V CSEL Neutron Cross Sections, Progress Report No. 2*, UCC-ND-IC (August 14, 1979).

5. P. J. Maziasz, "Microstructural Design for Fusion First-Wall Applications and Recommendations for Thermal-Mechanical Preirradiation Treatments," *ADIP Quart. Prog. Rep. June SO, 1979,* DOE/ET-0058/6, pp. 48–56.

2.5 RESULTS OF PROTOTYPIC TESTING FOR THE MFE-5 IN-REACTOR FATIGUE CRACK PROPAGATION EXPERIMENT - A. M. Ermi (Hanford Engineering Development Laboratory).

2.5.1 ADIP Task

Task I.B.1, Fatigue Crack Growth in Austenitic Alloys (Path A).

2.5.2 Objectives

An apparatus to perform in-reactor fatigue crack propagation tests on the Path A Reference Alloy is being developed. Effects of dynamic irradiation on crack growth behavior will be evaluated by comparing the results with those of unirradiated and postirradiated tests.

2.5.3 Summary

Prototypic testing of key components of the in-reactor fatigue crack propagation experiment has been completed. A prototypic pressurization system, designed to actuate a specimen chain by cycling the pressure inside of a bellows, has been demonstrated. Chains of miniature center-cracked-tension specimens were tested on a conventional MTS machine to investigate the viability of chain testing. The results of each chain test adequately define one crack growth curve. When only the initial and final crack length values are known, the same crack growth curve can be constructed through statistical analysis.

2.5.4 Progress and Status

2.5.4.1 Introduction

Fatigue crack propagation (FCP) in the first wall of magnetic fusion reactors may be a limiting criterion governing reactor lifetimes. All previous studies of irradiation effects on FCP have been conducted out of reactor on materials pre-irradiated in the unstressed condition. The ORR-MFE-5 experiment is designed to investigate FCP during irradiation, where dynamic irradiation may effect crack growth characteristics.

2.5.4.2 In-Reactor Fatigue Machine Pressurization System

In order to perform the in-reactor FCP tests, a pneumatically actuated fatigue machine is being developed. A description of the apparatus and test plan was reported earlier.[1]

An integral part of the fatigue machine is the pneumatics systems, which will provide the pressure required to obtain the desired conditions of load, frequency and waveform. A schematic of the bellows pressurization system, showing only the key components, is illustrated in Figure 2.5.1. The chamber region of the fatigue machine surrounding the bellows will be kept at a constant pressure of up to 300 psig with high purity helium. The loading on the specimens is then achieved by cyclicly varying the helium pressure in the bellows. When the maximum bellows pressure is less than the chamber pressure, a tension-tension load will be transmitted to the specimen chain. Note that the load follows a path inverse to that of the bellows pressure.

A sawtooth waveform at a frequency of 1 cycle/min was selected for MFE-5. The waveform is achieved by usage of a flow controller during pressurization, and by using a series of throttling valves at the exit during the venting sequences. The three exit valves are set at specific flow rates for the range of pressures at which they are utilized. Thus, what would normally be an exponential pressure-time response using a single exit valve is linearized using three exit valves.

Operation of the pressurization system is as follows. After the chamber and bellows have been brought up to pressure, a timer is activated. This closes solenoid valve 1, opens solenoid valve 3, and changes the path of valve 2 from a-b to b-c. The bellows then vents at a rate determined by the throttling valve at 3. When the pressure in the bellows drops to some preset value, pressure switch B opens solenoid valve 4. Venting continues through the throttling valves at both 3 and 4. With a further drop in pressure, switch C opens valve 5, allowing additional flow through the throttling valve at 5. At some minimum pressure, switch A de-energizes all solenoid valves, returning them to their initial condition as shown in the diagram. Flow into the bellows is now regulated by

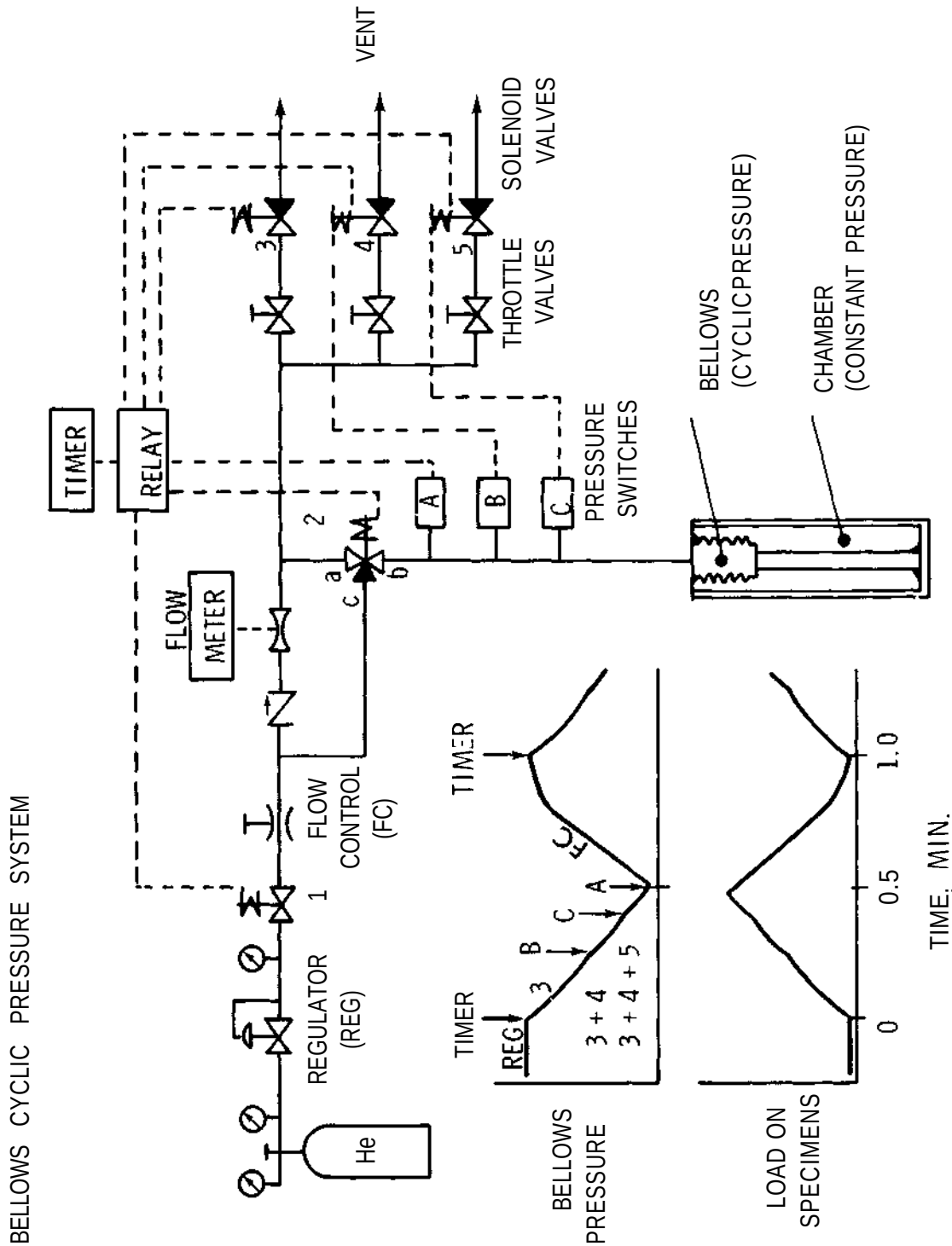

Figure 2.5.1: Schematic of Key Components of the Bellows Pressurization System.

the flow controller. At the end of the cycle, the timer triggers the start of the next cycle. The load, waveform and frequency can be adjusted by simply changing the operating pressures, throttling valves, timer and pressure swtiches.

Portions of a pressure-time plot obtained from the prototypic pressur-ization system is reproduced in Figure 2.5.2.

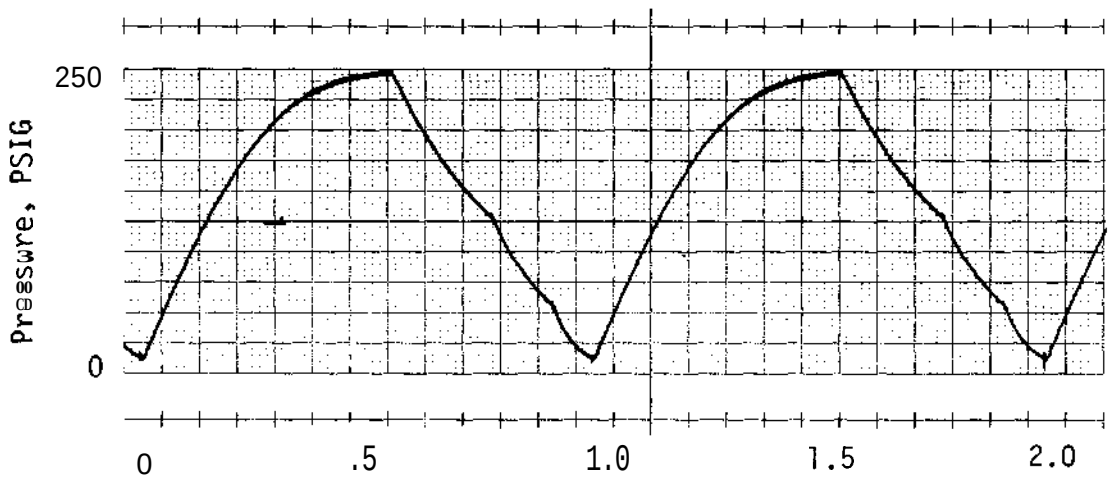

Figure 2.5.2 Pressure-Time Response of the Prototypic Pressurization System.

The output was taken from a pressure transducer located at the end of fifty feet of 1/8" tubing. The results indicate that the system does produce a satisfactory waveform for FCP testing. In particular, during the lower pressure portions of the cycle, the response is very good, resulting in the triangular waveform desired during peak loading.

2.5.4.3 Miniature CCT Specimen Chain Tests

The in-reactor FCP tests will be conducted on a chain of eight miniature center-cracked-tension (CCT) specimens.[2] The specimens will be precracked to five different initial crack lengths; one crack length will be duplicated and another triplicated. In preparation for the in-reactor FCP experiment, tests on a chain of annealled 316 stainless steel specimens (heat 81585) using a conventional MTS machine were conducted. The experimental conditions for two such tests are listed in Table 2.5.1.

Table 2.5.1 FCP Chain Tests
Experimental Conditions

Material:	Annealed 316 stainless steel	
Specimens:	Miniature center-cracked-tension	
Environment:	Room temperature air	
Test #:	Test 1	Test 2
. Chain Size:	5 specs.	4 specs.
. Stress Ratio, R:	0.05	0.50
. Frequency, sec^{-1}:	7.5	10.0
. Cycles, AN:	265,000	405,000

The five specimens in the first test were precracked to different crack lengths, and cycled until the specimen with the largest precrack completely separated. The crack lengths for all specimens were monitored every five minutes during the ten hour test using the electrical potential method.[3] In Figure 2.5.3, the crack length is plotted versus cycles for the five specimens. The curve was derived by horizontally shifting overlays of individual crack length versus cycles curves until one smooth curve was obtained.

The individual crack growth curves are plotted in Figure 2.5.4, exhibing a maximum factor of difference of 1.2 in crack growth rate for any given value of stress intensity range, well within the factor of 2 allowed by the ASTM.[4] From these results, or from the crack length versus cycles plot of Figure 2.5.3, it is possible to construct a single crack growth curve for the entire test. However, in the actual in-reactor and ex-reactor tests, it will not be possible to monitor the crack lengths since the specimens will be immersed in sodium. Only the initial and final crack lengths will be measured. A crack growth curve from this information can be determined by the following method.

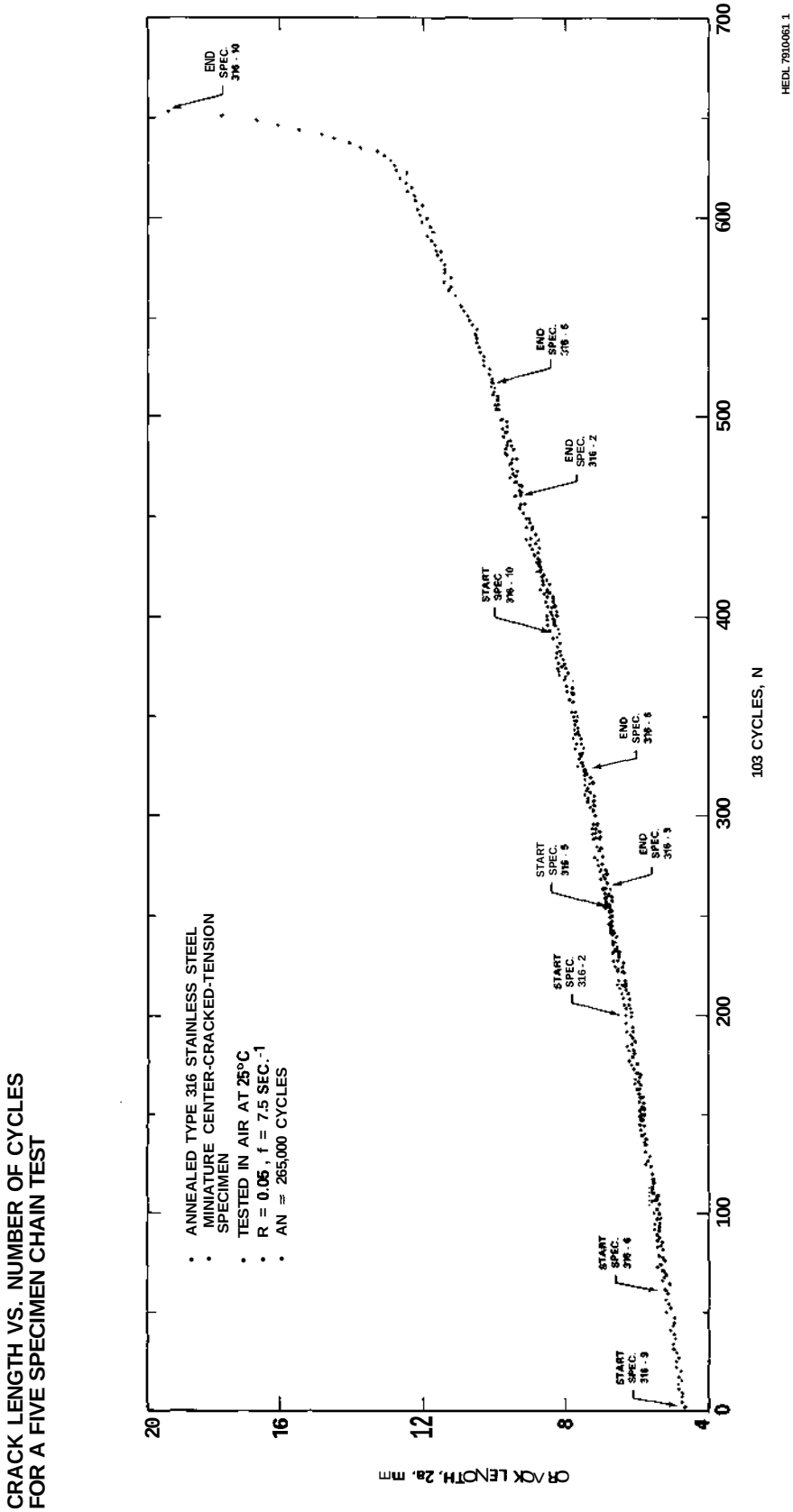

Figure 2.5.3: Crack Length Measurements for a Five Specimen Chain Test Using the Electrical Potential Method.

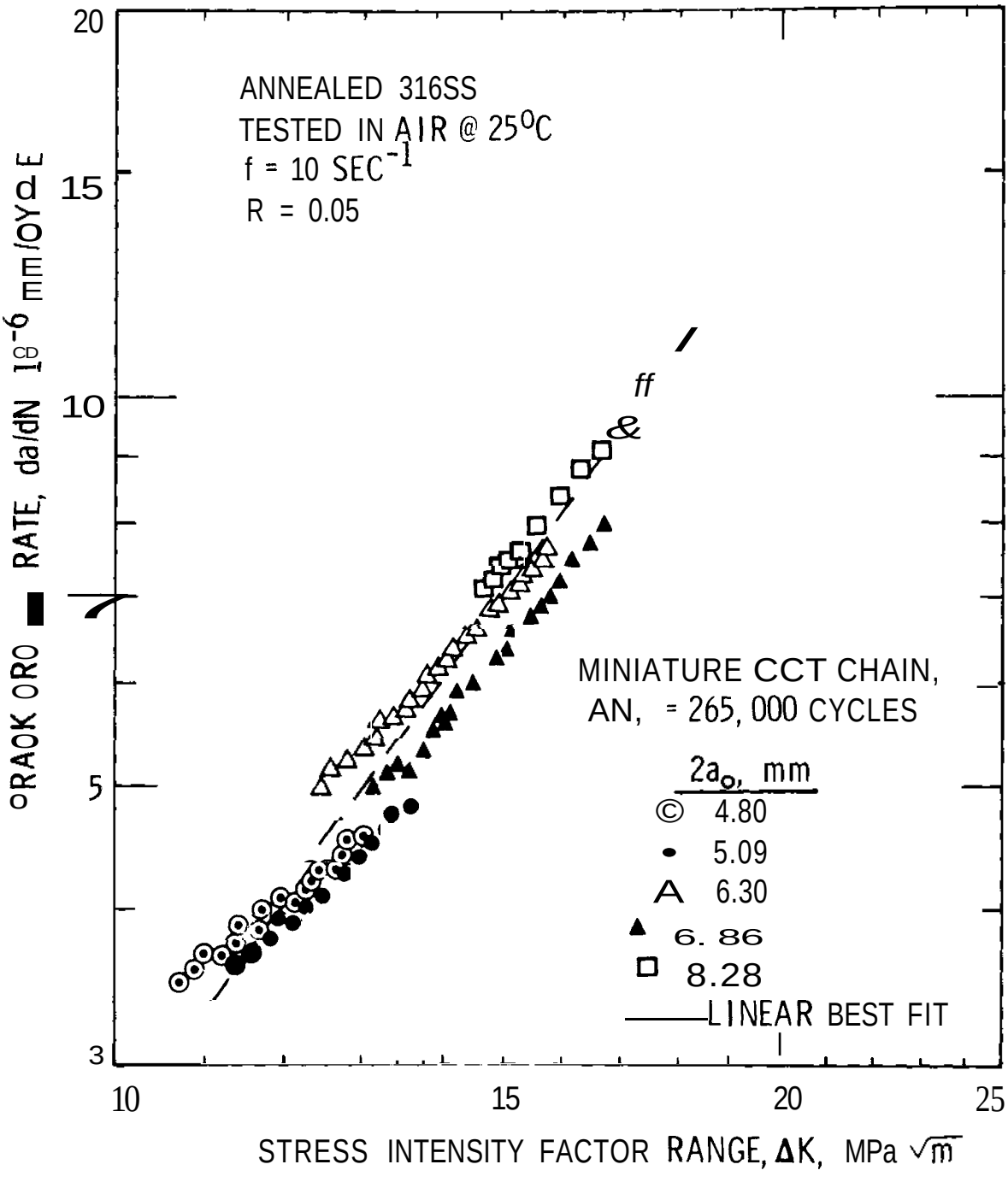

Figure 2.5.4: Crack Growth Curve for a Five Specimen Chain Test.

Consider the equation describing the Paris regime of the crack growth curve,

$$\frac{da}{dN} = \alpha \Delta K^{\beta} \qquad [1]$$

where $\frac{da}{dN}$ = crack growth rate,

ΔK = stress intensity factor range, and

α, β = constants

Solving for the coefficient a through numerical integration yields

$$\alpha = \frac{1}{AN} \sum_{a_o}^{a_f} \frac{\Delta a}{\Delta K(a)^{\beta}} \qquad [2]$$

where a_o = initial crack length,

a_f = final crack length, and

Δa = crack growth increment.

For purpose of calculation, Δa was chosen as $(a_f - a_o)/50$.

Since any one specimen will have an infinite number of a and 3 pairs (Figure 2.5.5), the next step is to determine some optimum values for a and 3 which best describes all specimens in the chain. Optimization of a and 3 for the test is initiated by assuming some value for 3 in [2] and calculating a value of a for each specimen. The average value of a is then compared to each individual a through the computation of an error function. The value of 3 is then incremented until the error is minimized for the desired amount of significant figures in 3.

Plots for five different selections of 3 for three specimens is given in Figure 2.5.6. The error function, defined as

$$\text{ERROR} = \sum_{i=1}^{n} (\alpha_i/\bar{\alpha} - 1)^2 \qquad [3]$$

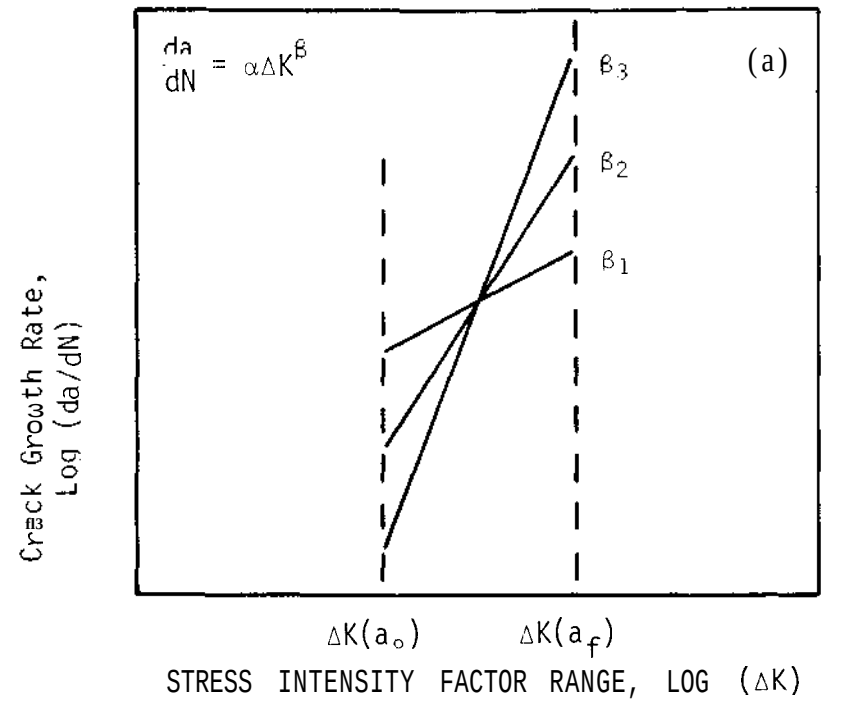

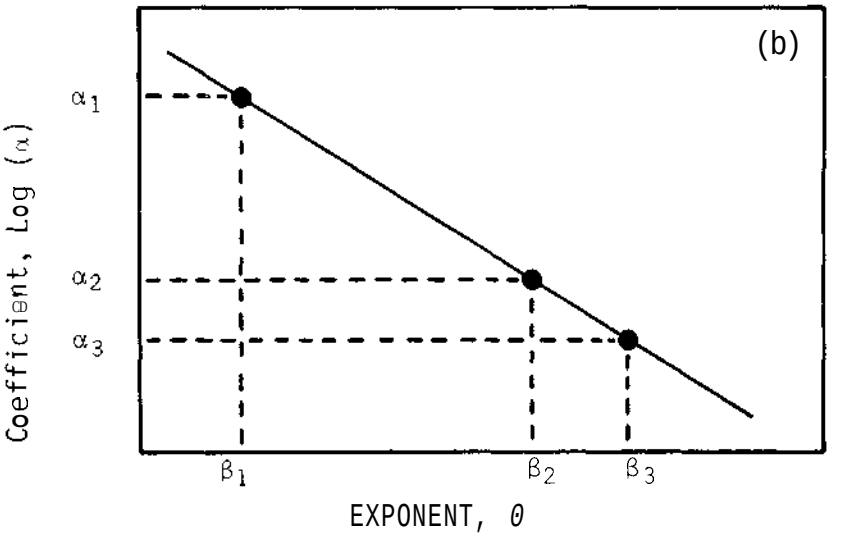

Figure 2.5.5: (a) Possible Crack Growth Curves, and
(b) Variations of a with 8 for a Single Specimen where only the Initial and Final Crack Lengths are Known.

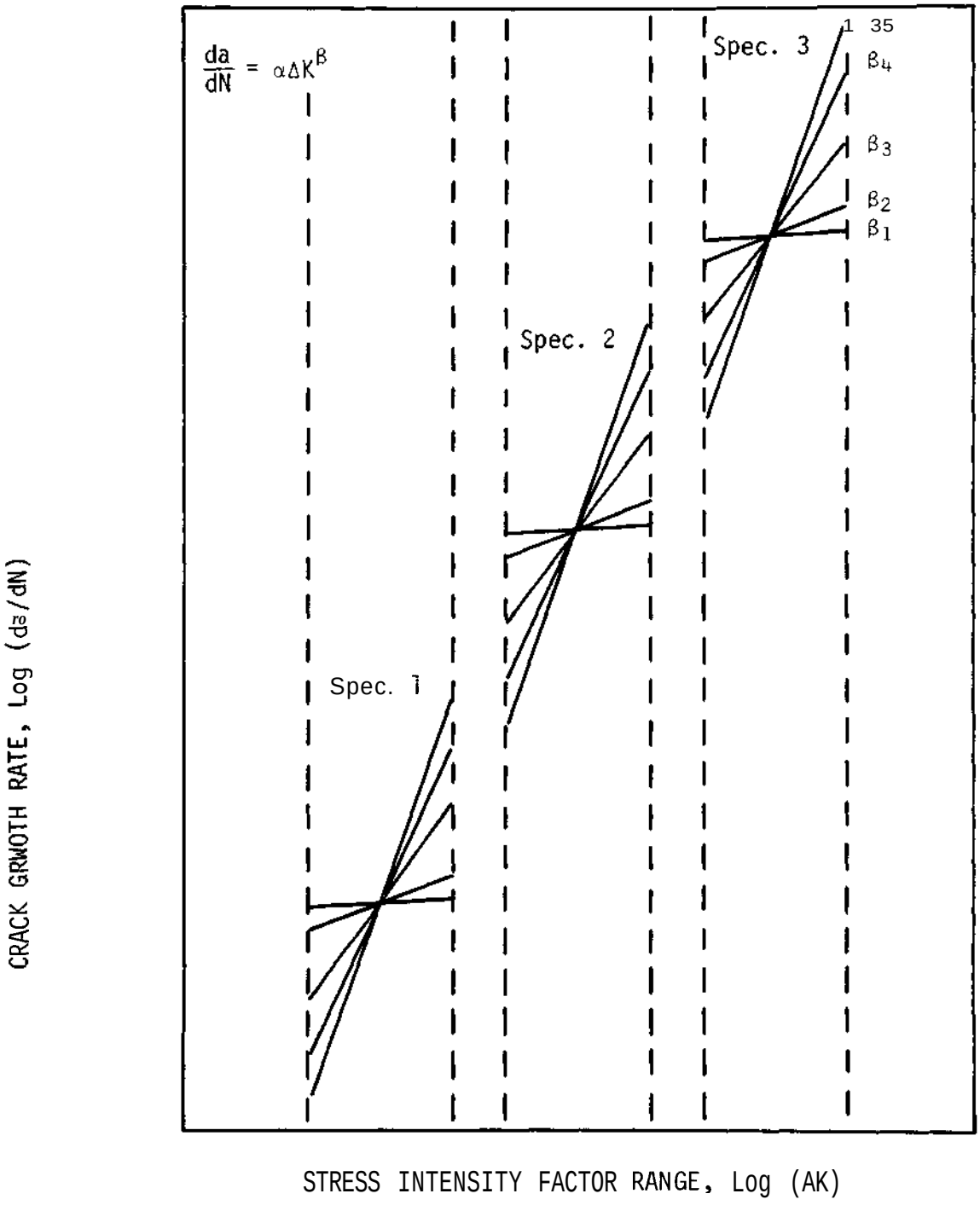

Figure 2.5.6: Various Crack Growth Curves for Three Specimens where only the Initial and Final Crack Lengths are Known.

is plotted versus 3 in Figure 2.5.7.a, and graphically illustrates the method of determining the optimum crack growth curve, Figure 2.5.7.b.

Application of this technique to the five specimen chain test results in the dashed curve in Figure 2.5.4. The curve was determined from the knowledge of only the initial and final crack lengths from the four specimens still intact, the fifth specimen having been separated. The method gives the desired result as long as (a) the actual crack growth rate is linear over the region of interest, and (b) all specimens are subject to the same test conditions. Violation of (a) can be handled by applying the technique to cover bilinear crack growth behavior. Violation of (b) is more difficult to deal with, and can best be handled by minimizing any variations in test parameters from specimen to specimen. Variations which cannot be eliminated must at least be investigated as to their effects on crack growth. The important parameter which will vary for the in-reactor FCP test is the total fluence. Specimens at the ends of the chain will receive roughly one-half the peak fluence experienced by specimens near the center of the chain. To minimize the effects of fluence, the specimens precracked to the five distinct initial crack lengths will be positioned in the high flux regions of the chain. The difference in fluence between any two specimens is reduced from a factor of 2 to a factor of about 1.3. The remaining three specimens, which have crack lengths duplicating others in the high flux region, will then serve to reflect any significant effects of fluence. In addition, the ex-reactor test, which will parallel the in-reactor test, will enable one-to-one comparisons between any irradiated specimen with an unirradiated specimen.

To further investigate chain performance, the test was continued using a different stress ratio. This permitted investigation of lower crack growth rates during chain testing, as well as the effects of R (min/max stress) on the overall FCP behavior. The results from both chain tests (R=0.05 and 0.50) are compared in Figure 2.5.8 where the data for all specimens at each R value is plotted together. Again, the reproducibility of the crack growth curve for R = 0.50 is evident since the data represents four specimens.

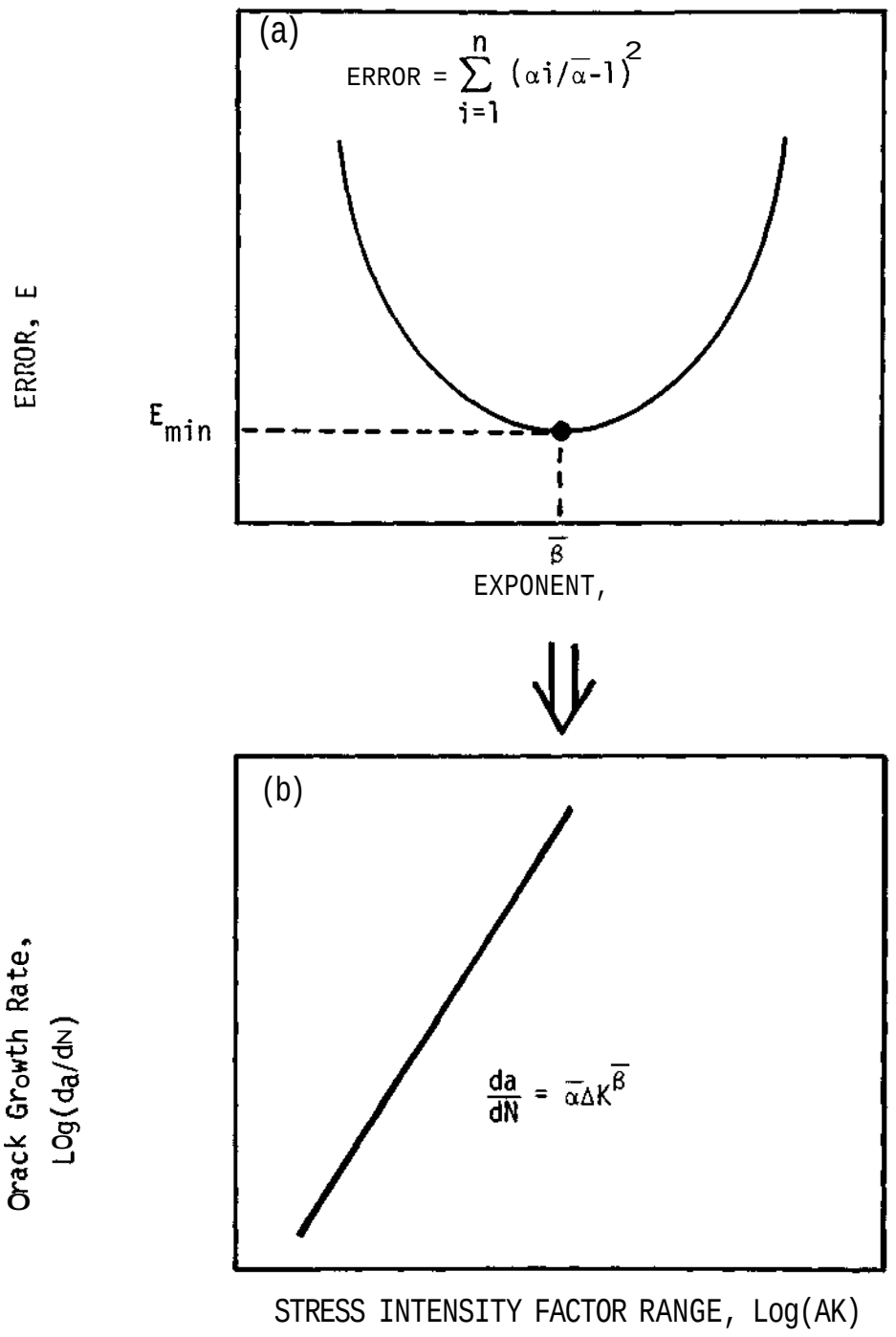

Figure 2.5.7: (a) Determination of the Best Values of a and 6, and
(b) The Best Crack Growth Curve for Several Specimens where only the Initial and Final Crack Lengths are Known.

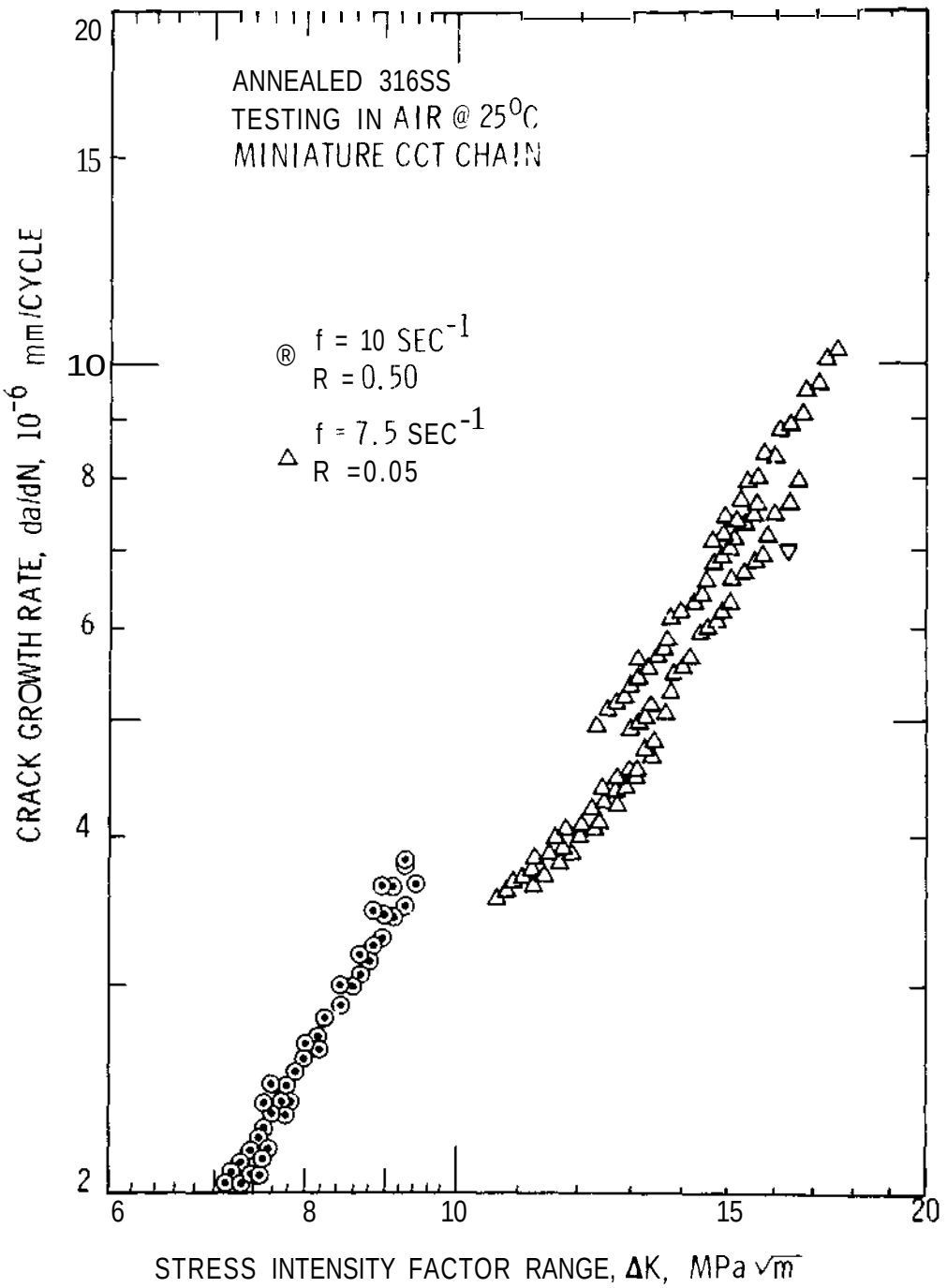

Figure 2.5.8: Crack Growth Curve for Two Chain Tests at Different Stress Ratios,

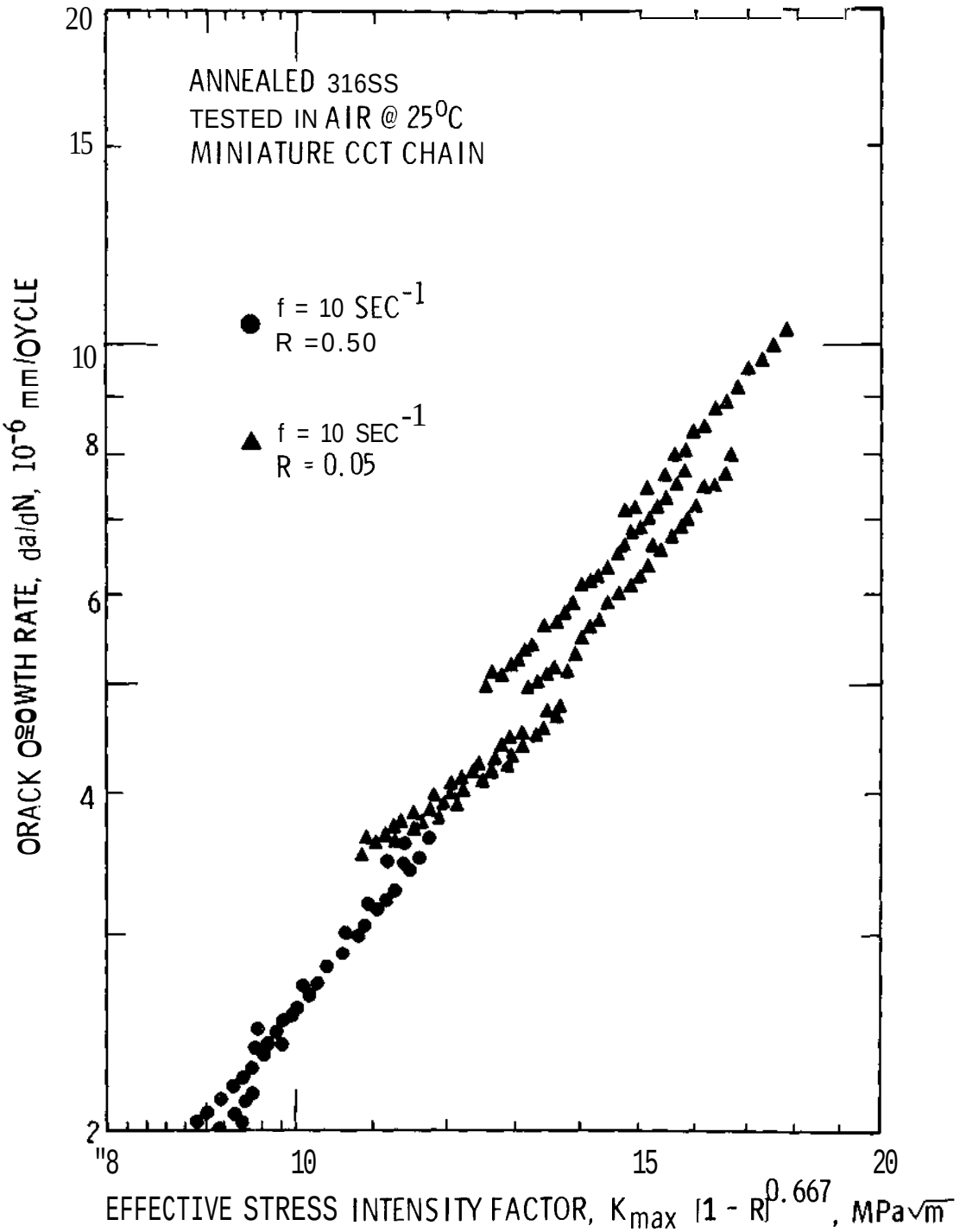

Figure 2.5.9: Crack Growth Rate Versus Effective Stress Intensity Factor for Two Chain Tests at Different Stress Ratios.

Effects of stress ratio on FCP have long been observed, prompting the development of various relationships to incorporate this effect. James[5] has reported that the use of the effective stress intensity factor, K_{eff}, instead of AK describes the effects of R for various austenitic stainless steels:

$$K_{eff} \quad {}_{max}[1-R]^{m} \qquad [4]$$

where m is a constant determined empirically. The crack growth rate is plotted versus K_{eff} in Figure 2.5.9 for the two chain tests in which a value of m = 0.667 adequately describes a single curve. From this result, it appears that the data is consistant with observations made on the larger conventional specimens. The overall results indicate that successful tests can be carried out on specimen chains at the various stress ratios, frequencies and crack growth rates reported above.

2.5.5 Conclusions

(a) A prototypic pressurization system which will provide tension-tension loading has been successfully demonstrated.

(b) Successful specimen chain tests were completed at frequencies of 7.5 and 10 sec^{-1}, and at stress ratios of 0.05 and 0.50.

(c) Crack growth curves can be constructed from only initial and final crack length information from specimen cahins.

2.5.6 Future Work

Fabrication of the prototypic fatigue machine to be tested at HEDL is 75% complete. An eight specimen chain test on the Path A Reference Alloy, 20% cold worked 316 SS, is being planned for the prototype. The experiment will be conducted in helium at room temperature. Four of the specimens in the chain will be wired to monitor crack growth using the electrical potential method.

2.5.7 References

1. A. M. Ermi, "Status of an In-Reactor Crack Growth Experiment," Sixth ADIP Quarterly Progress Report, 1979, DOE/ET-0058/6.
2. L. A. James, J. L. Straalsund and R. E. Bauer, "Optimization of Fatigue Crack Growth Testing for First Wall Materials Development Evaluations," presented at the First Topical Meeting on Fusion Reactor Materials, Miami Beach, January 29-31, 1979; HEDL-SA-1621.
3. J. L. Straalsund and D. A. Mervyn, "Adaptation of an Electrical Potential Technique to Measure Fatigue Crack Crowth," ADIP Quarterly Progress Report, December 31, 1978, DOE/ET-0058/4, pp. 4-9.
4. ASTM Designation E647-78T, Annual Book of ASTM Standards, Part 10 (1979) pp. 707.
5. L. A. James, "Fatigue-Crack Propagation in Austenitic Stainless Steels," Atomic Energy REview, 14, 1(1976) pp.53-57.

2.6 MINIATURE TENSILE TESTING - E. K. Opperman (Hanford Engineering Development Laboratory).

2.6.1 ADIP Task

Task 1.B.13, "Tensile Properties of Austenitic Alloys."

2.6.2 Objective

The objective of this work is to develop miniaturized tensile specimens and a compatible test machine in support of Fusion Materials Testing. The small specimen size is required in order to irradiate a statistically meaningful number of specimens in the limited volumes available for Fusion Materials Testing, such as RTNS-II and FMIT. A small, tabletop, tensile test machine was developed to accommodate miniature specimens by providing accurate and stable alignment with specimen size and handling consideration in mind.

2.6.3 Summary

The apparatus and techniques required to carry out postirradiation tensile tests on miniaturized wire specimens have been developed and tested. Results of tests on nine AISI 316 stainless steel wire specimens demonstrate that the test machine operates in a reproducible manner and that the specimen geometry yields results comparable to conventional specimens.

This report will briefly describe the apparatus, specimen geometry and preliminary test results.

2.6.4 Progress and Status

2.6.4.1 Introduction

The present day accelerator based fusion neutron sources, such as RTNS-II, and the Fusion Materials Irradiation Test Facility (FMIT), all have very limited irradiation volumes when compared to materials test reactors. In order to utilize small irradiation volumes, in a statistically meaningful manner, the use of small specimens sized to the flux volumes is required.

In response to these conditions, HEDL has developed techniques to fabricate miniature wire tensile specimens from various alloys and a tensile test machine specifically designed to load, grip and align small specimens. Any ultimate miniaturization of mechanical property specimens is limited by grain size considerations if "bulk specimen" results are desired.

2.6.4.2 Specimens and Test Machine

The miniature tensile specimens are fabricated by chemically milling a gage section from a .76 mm diameter wire. Figures 2.6.1 and 2.6.2 illustrate the size and shape of the miniaturized specimens. The overall length of each specimen is 13 mm with a nominal gage length of 4-6 mm and a minimum diameter of 0.25 mm. Specimens have successfully been fabricated from 316 stainless steel, pure nickel and titanium 6AL-4V.

Chemical milling techniques generally produce gage sections with gradually varying diameter profiles. Therefore, accurate measurement techniques are required in order to characterize the specimen geometry. Fig. 2.6.3 shows a specimen diameter profile from a chemically milled stainless steel specimen. The diameters were measured using a Zygo 110-A noncontacting laser telemetrix system. The diameter versus length values are computer processed for graphic display and to identify the "plastic gage length," or the length over which yield occurs during the tensile test.

The tensile machine has a horizontal load train consisting of a motor-driven roller slide in series with a load cell and specimen. Fig. 2.6.4 illustrates the overall machine. Displacement or strain is measured with two LVDT's mounted on each side of the specimen and co-planar with the specimen and screw drive axis. Fig. 2.6.5 shows the region surrounding the test specimen. The specimen is held or gripped between a pair of serrated, hardened-steel collets.

2.6.4.3 Preliminary Results

Initial tests were conducted on nine AISI 316 SS specimens and the results are presented in Table 2.6.1. The values of the ultimate tensile strength, yield stress, total elongation and reduction in area are comparable to reference values which indicate the wire specimens are giving

Fig. 2.6.1: Miniature tensile specimen.

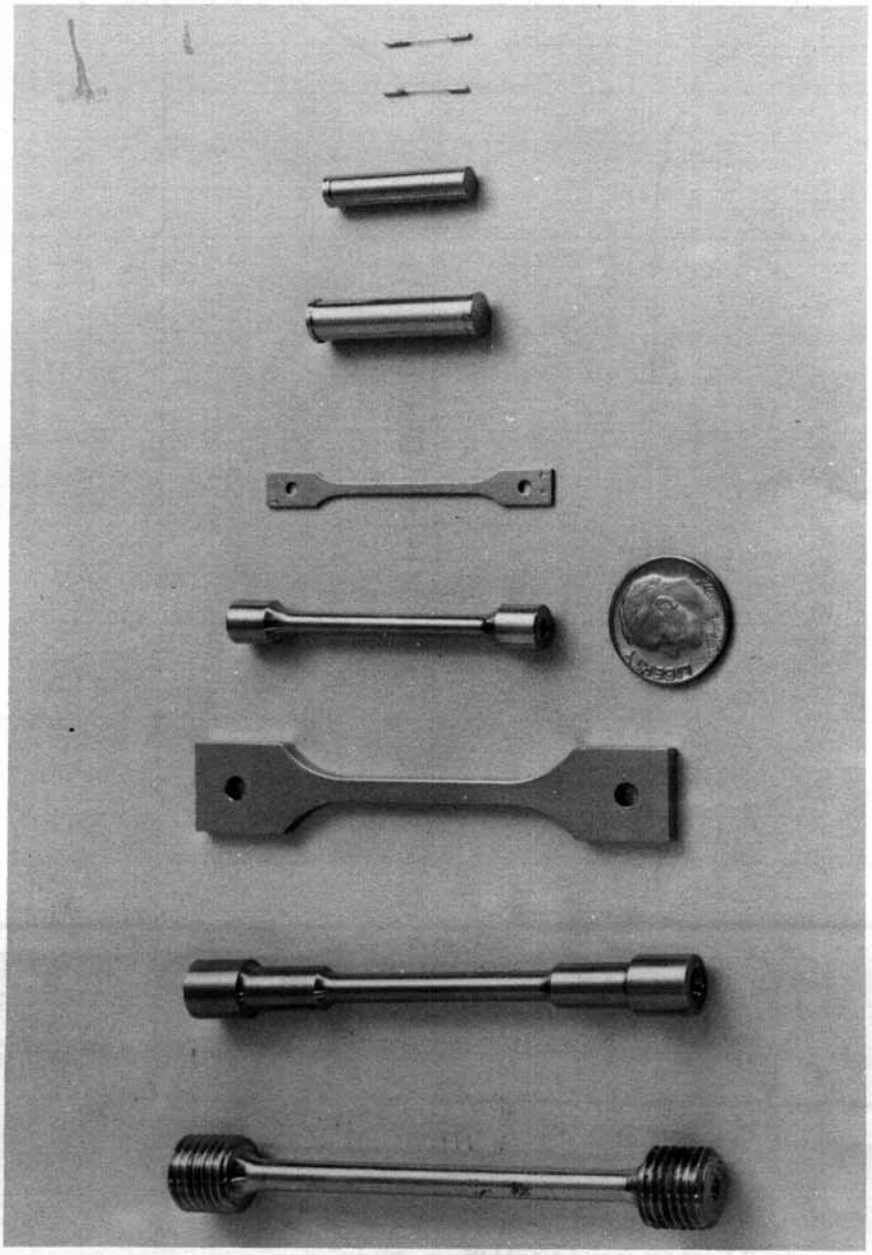

Fig. 2.6.2: Size of miniature tensile specimens relative to other small tensile and creep specimens.

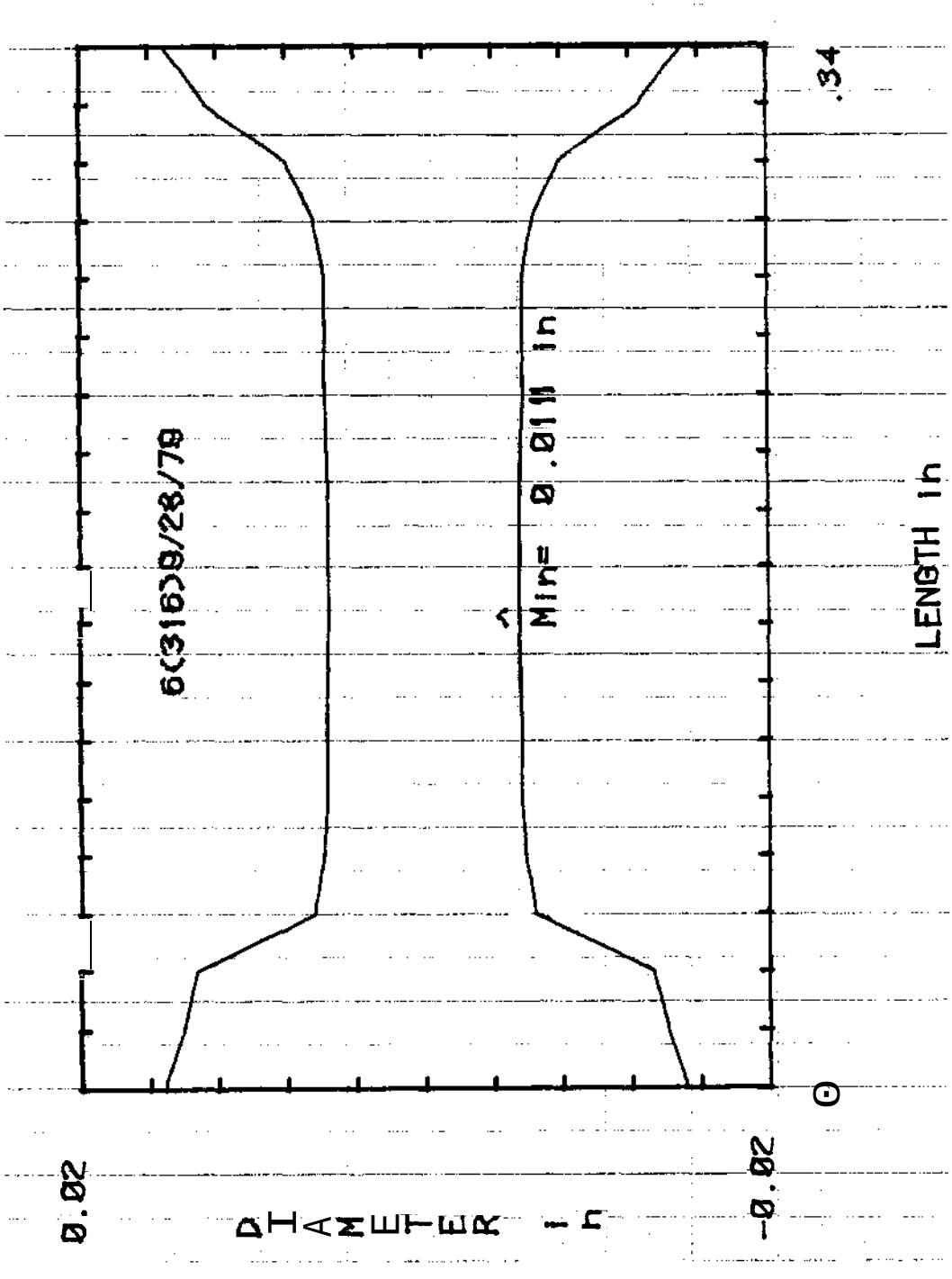

Fig. 2.6.3: Diameter profile of miniature tensile specimen.

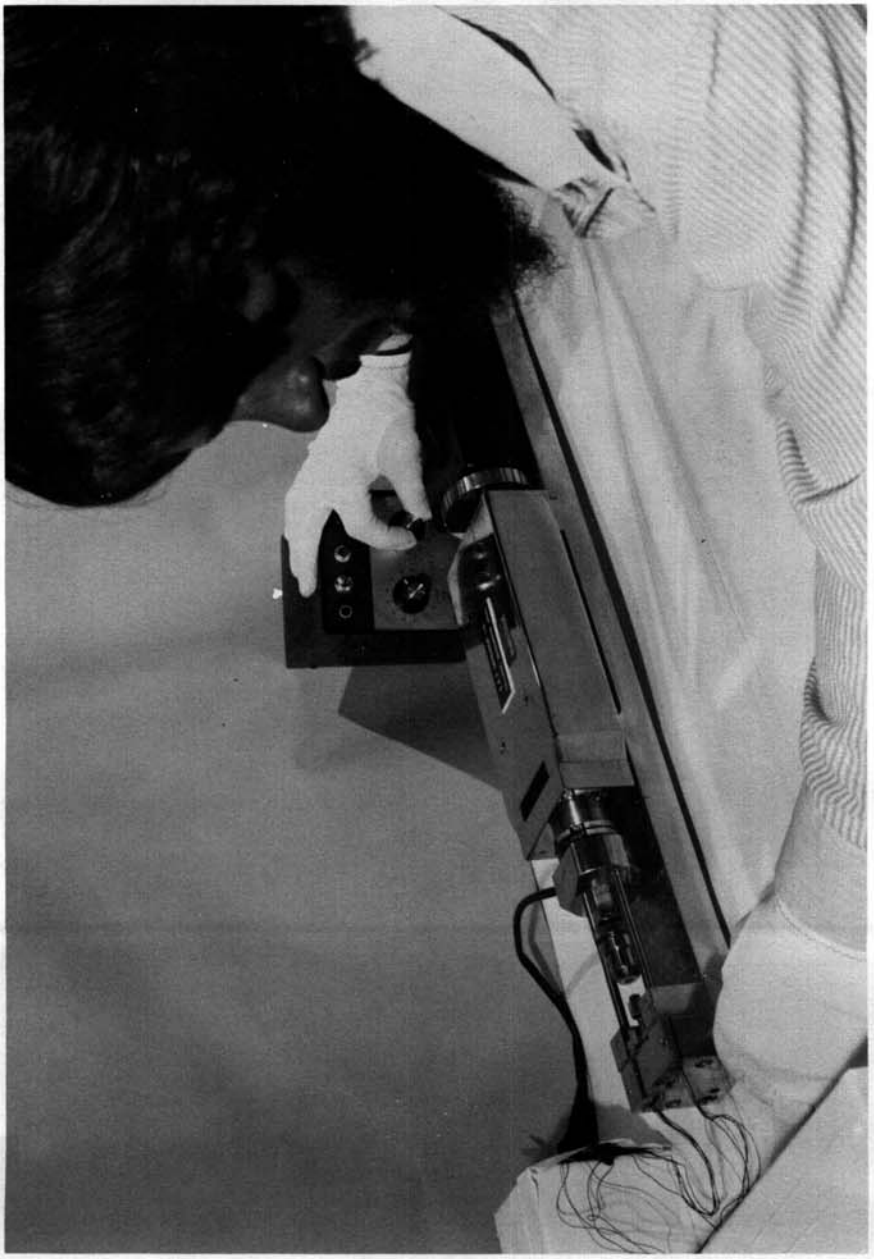

Fig. 2.6.4: Miniature tensile machine in operation.

Fig. 2.6.5: Test specimen being loaded into tensile machine.

Table 2.6.1

PRELIMINARY TENSILE RESULTS USING MINIATURE SPECIMENS

SPECIMEN* NO.	ULT TENSILE STRENGTH (MPa)	TOTAL ELONGATION (%)	YIELD STRESS (MPa)	GAGE LENGTH PLASTIC (mm)	MINIMUM DIAMETER (mm)	REDUCTION IN AREA (%)
316-1	731	31	558	3.91	.289	83.5
316-2	703	43	613	3.15	.267	82.0
316-3	690	38	586	2.92	.277	74.7
316-4	676	32	545	3.55	.244	78.1
316-5	669	28	565	5.84	.277	83.4
316-6	662	44	531	3.40	.282	87.3
316-7	593	25	517	2.92	.175	80.0
316-9	731	25	682	2.44	.251	78.4
316-10	627	29	545	3.91	.274	75.8
Average & Std. Deviation	676 ± (45)	32.8 ± (7.2)	572 ± (50)			80.3±(4.1)
NSM Value [1]	758-862	14-34	586-724			

*20% CW 316 SS (HT V87210)

bulk-specimen results. Bulk results were anticipated because of the relatively small grain size of the 20% CW material compared to the wire diameter. Fig. 2.6.6 shows an optical micrograph taken from the gage section of the specimen. The grain size is ASTM #7 (average diameter 0.04 mm), which results in 7~10 grains across the diameter. Fig. 2.6.6 also shows that the chemical milling technique results in a. round, symmetric specimen cross section.

The overall load versus strain plots for four of the specimens are shown in Fig. 2.6.7. The curves indicate a small amount of strain hardening following the onset of yield and good ductility. The ductility is also reflected in the reduction in area (RA) values listed in the table. These RA values were determined from optical micrographs in the fractured region. Fig. 2.6.8 shows the fracture to be a "cup and cone fracture," indicating a ductile material.

2.6.5 Conclusions

The feasibility of fabricating, handling and testing very small wire specimens was demonstrated. Results taken from nine AISI 316 SS specimens indicates that meaningful, bulk tensile properties can be obtained from miniaturized tensile specimens.

2.6.6 References

1. Hanford Engineering Development Laboratory, *Nuclear Systems Materials Handbook*, Vol. 1, Revision 6, (June 1, 1978).

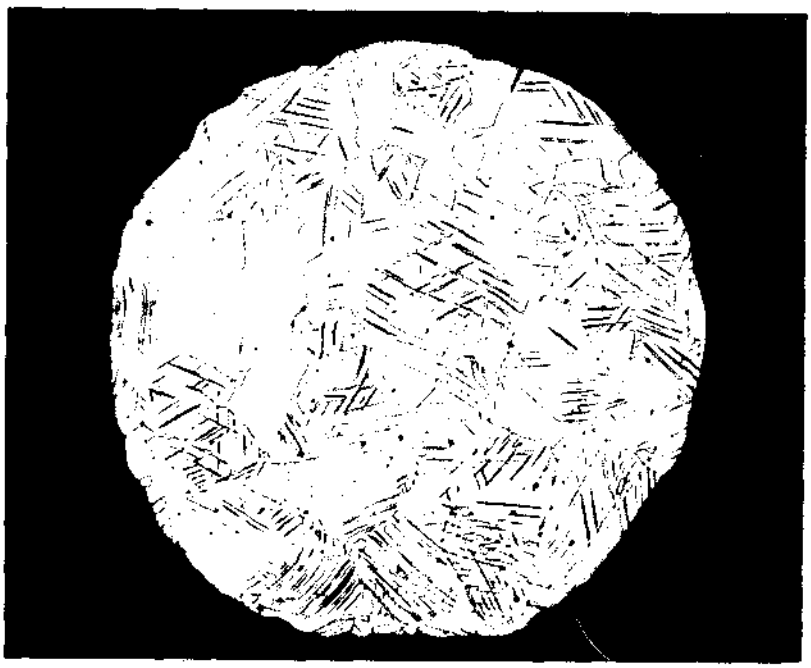

Fig. 2.6.6: Cross section of miniature tensile specimen (300X), grain size ASMT #7.

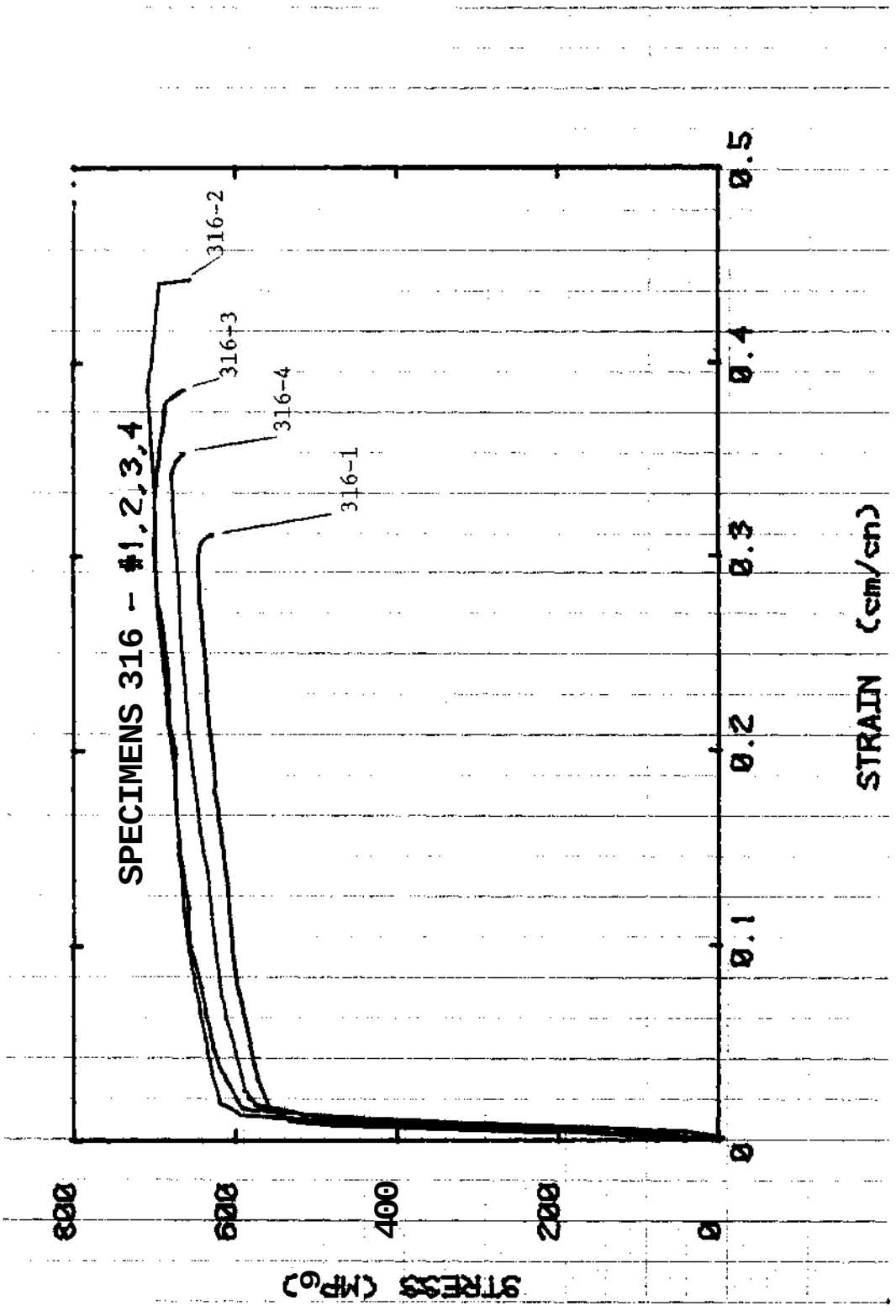

Fig. 2.6.7: Tensile curves for four specimens.

3. PATH A ALLOY DEVELOPMENT - AUSTENITIC STAINLESS STEELS

Path A alloys are those alloys generally known as austenitic stainless steels. The most common U.S. designations are AISI types 304, 316, 321, and 347. Primary considerations for selecting this class of alloys for further development are:

1. state-of-the-art production and fabrication technology;
2. extensive data on the effects of neutron irradiation on properties, which show the potential of these alloys for MFR applications;
3. compatibility with proposed coolants and breeding fluids;
4. evidence that for MFR conditions (He, dpa, temperatures) the properties are sensitive to composition and microstructure — thus showing potential for further development.

The strategy for development of these alloys has two related objectives:

1. to determine for a reference alloy the effects of irradiation on those properties most important to fusion reactor design;
2. to develop a Path A alloy that is optimized for fusion reactor applications.

The first objective will provide a data base for near-term reactor design and, most important, guidance as to which properties limit performance of this type alloy. Work on the reference alloy will provide direction for the actual alloy development efforts of the second objective. Type 316 stainless steel in the 20%-cold-worked condition appears to be the best choice as a reference alloy. It is the present reference cladding and duct alloy in the breeder reactor programs, and there are extensive data on the unirradiated mechanical properties, effects of heat treatment on properties, structure, and phase stability, and the effects of fast neutron irradiation on properties. The present technology of austenitic stainless steels, including understanding of the physical and mechanical properties and irradiation response, is such that alloy development efforts can move to optimization for use in fusion reactor applications. A Prime Candidate Alloy (PCA) (Fe—16%Ni—14% Cr—2% Mo—2% Mn—0.5% Si—0.2% Ti—0.05% C) has been selected by the ADIP task group. Efforts will now focus on optimizing the composition and microstructure of the PCA leading toward the selection of OPT-A1 (Program Plan designation of first optimized Path A alloy).

3.1 FATIGUE BEHAVIOR OF 20%-COLD-WORKED TYPE 316 STAINLESS STEEL AFTER IRRADIATION IN THE HFIR - M. L. Grossbeck and K. C. Liu (ORNL)

3.1.1 ADIP Task

ADIP Task I.B.5, Stress-Strain Controlled Fatigue of Austenitic Alloys.

3.1.2 Objective

This study evaluates the effects of simultaneous displacement damage and helium production during irradiation on the fatigue life of 20%-cold-worked type 316 stainless steel.

3.1.3 Summary

Work is now in progress to extend our previously reported fatigue data to the high-cycle regime. We have tested control specimens before testing irradiated specimens. Data from the high-cycle tests correlate well with low-cycle strain controlled data for control specimens.

3.1.4 Progress and Status

3.1.4.1 Introduction

Since a tokamak reactor operates in a cyclic mode, thermal stresses will result in fatigue in structural components, especially in the first wall and blanket. There has been limited work on fatigue in irradiated alloys[1] but none on irradiated materials containing irradiation-induced helium. To provide scoping data and to study the effects of irradiation on fatigue behavior, we studied the low-cycle fatigue properties of 20%-cold-worked type 316 stainless steel from the MFE reference heat.

Although ductility is primarily important in determining low-cycle fatigue life (strains producing $<10^5$ cycles to failure), strength is the prime factor in determining high-cycle fatigue life. Since irradiation typically embrittles and usually strenghtens materials, the expected result is to shorten low-cycle life and to extend high-cycle life in fatigue. The degradation of cyclic life in the low-cycle regime

has been confirmed by previous tests,[9] but the effect of irradiation on high-cycle life remains to be investigated. This investigation is currently in progress.

3.1.4.2 Experimental Procedure

Hourglass specimens with minimum gage diameters of 3.18 mm (0.125 in.) were irradiated in the High Flux Isotope Reactor (HFIR) in peripheral target positions, providing both a high rate of displacement damage and rapid helium production from capture of thermal neutrons by nickel. A helium gas gap controlled the temperature. The experiment was monitored by inclusion of low-melting alloys, as described previously.[9]

Tests were performed on a servo hydraulic testing system equipped for remote operation.[4] Specimens were tested in a vacuum at pressures from 10^{-5} to 10^{-4} Pa. The gage section of the specimen was maintained at 430°C ± 5°C, remaining constant within ±1°C during the test. Strain control for the low-cycle tests was achieved with a diametral extensometer with alumina blades and a linear variable differential transformer (LVDT). The diametral signal in turn was converted to an equivalent axial strain through a strain computer for machine control. A fully reversed ramp function was used. Specimens were cycled to complete separation.

Strain control at a rate of 4×10^{-3}/s was used until a stable hysteresis loop was established. Control was then transferred to load, and the strain rate was increased to 4×10^{-2}/s.

3.1.4.3 Results

Six specimens have been tested with the strains and loads shown in Table 3.1.1. Results correlate well with previous low-cycle data. The above data will be compared with similar data from irradiated specimens.

3.1.5 Conclusions

Data on unirradiated material for high-cycle fatigue have been obtained. Load control tests using a strain rate of a factor of 10 greater than used for low-cycle tests appear to be useful and correlate well with the high strain rate strain controlled tests. Irradiated specimens will now be tested under similar conditions.

Table 3.1.1. High-Cycle Fatigue Life of Unirradiated 20%-Cold-Worked Type 316 Stainless Steel at 430°C[a]

Specimen	Controlled Strain Range (%)	Controlled Load (kN)	Stress (MPa)	Cycles to Failure
G11	0.6	16	500	113,485
G13	0.5	15	470	207,475
G14	0.5	15	470	112,045
G16	0.4	14	430	346,641
G17	0.4	12	370	358,390
G19	0.3	9.0	280	767,150

[a]Tests in vacuum.

3.1.6 References

1. J. M. Beeston and C. R. Brinkman, "Axial Fatigue of Irradiated Stainless Steels Tested at Elevated Temperatures," pp. 419–50 in *Irradiation Effects on Structural Alloys for Nuclear Reactor Applications*, Am. Soc. Test. Mater. Spec. Tech. Publ. 484, American Society for Testing and Materials, Philadelphia, 1970.
2. M. L. Grossbeck and K. C. Liu, "Low-Cycle Fatigue Behavior of 20%-Cold-Worked Type 316 Stainless Steel," *ADIP Quart. Prog. Rep. June SO, 1979*, DOE/ET-0058/6, pp. 42-47.
3. M. L. Grossbeck and M. J. Kania, "HFIR Irradiation of Hourglass Fatigue Specimens," *ADIP Quart. Prog. Rep. June SO, 1978*, DOE/ET-0058/2, pp. 20–35.
4. K. C. Liu and M. L. Grossbeck, "Status of Fatigue Testing Facility," *ADIP Quart. Prog. Rep. June SO, 1978*, DOE/ET-0058/2, pp. 54–59.

3.2 FABRICATION OF HOMOGENEOUS PATH A PRIME CANDIDATE ALLOY - P. J. Maziasz and T. K. Roche (ORNL)

3.2.1 ADIP Tasks

ADIP Tasks I.A.5, Perform Fabrication Analysis, and I.D.I, Materials Stockpile for MFE Programs.

3.2.2 Objective

The objective of this work was to produce final specimen material (in this case sheet) with a uniform grain size, microstructure, and distribution of titanium. A proper fabrication sequence is necessary to produce homogeneous material for subsequent thermal-mechanical treatments designed to bring about designed preirradiation microstructures.

3.2.3 Summary

Previous work identified initial inhomogeneity in the as-received Path A Prime Candidate Alloy (PCA) plate stocks (and probably other finished forms as well). Fabrication experiments indicated that hot working had produced titanium-rich MC precipitation and that although initially fine and uniform, this phase could coarsen during further hot working. Solution treating to dissolve titanium-rich MC precipitate particles requires temperatures above 1150°C. The Ti(C,N)S and titanium-rich MN particles dissolve only at temperatures near melting, if at all. Homogenization before fabrication is essential. Our investigations addressed and solved all the problems encountered when producing final form material for specimens [0.25-mm-thick transmission electron microscope (TEM) discs punched from sheet]. Sheet 0.5 mm thick was also fabricated for thermal aging response studies of the Path A PCA.

3.2.4 Progress and Status

An inhomogeneous microstructure was found[1] in as-received finished 13.0-mm-thick PCA plate stock. This discovery resulted in the development of treatments for obtaining homogeneous starting material and the development of a fabrication route to produce homogeneous final specimen material.[2]

Fabrication of AISI type 316 and other 300 series austenitic stainless steels is relatively easy, with many methods of producing the same final product.[2] Such ease of fabrication is one of the advantages of using this class of alloy. The addition of titanium to type 316 transforms it into a potentially precipitation-hardenable material with better high-temperature stability. The precipitate phase is a titanium-rich MC that though potentially beneficial to the microstructure leads to loss of some of the freedom of fabrication. Inhomogeneous distributions of the MC particles can result if proper control of fabrication variables is not exercised. The inhomogeneous precipitate particle distributions will result in nonoptimum properties.[4] Thus, greater care is required for fabricating austenitic stainless steels containing titanium. The required fabrication schedule is simple enough that this remains an attractive feature of these alloys.

The fabrication sequence used to produce 0.5-mm-thick sheet for TEM specimens is presented in Fig. 3.2.1. The TEM discs were used to investigate the thermal-mechanical response of the Path A PCA for preirradiation microstructural design, and the results are discussed in Chap. 3.3 of this report. Three branches from the main flow diagram (between steps 3 and 4, 5 and 6, and 10 and 11) indicate problems that were encountered. Figures 3.2.2, 3.2,3, and 3.2.4 detail the investigations initiated to solve those problems. We developed solutions that resulted in fabrication sequences capable of producing homogeneous specimen material. The results from our investigation shown in Fig. 3.2.2 have been presented and discussed[1] and will be summarized here. The material had fine titanium-rich MC particles along dislocation cell walls as well as macroscopic variations in grain size associated with stringering of MC particles. The initial "homogenization" at 1150°C in step 2 was probably not adequate to completely dissolve titanium-rich MC because the solvus is about 1150°C.[1] Subsequent processing of the material (Fig. 3.2.2) was observed to coarsen and to redistribute the MC particles, leading to an inhomogeneous microstructure resembling that observed in the as-received plate (step 5, Fig. 3.2.1). Homogenization resulted from 1 h at 1200°C, but hot working reprecipitated MC. Cold working produced stringers in the unhomogenized

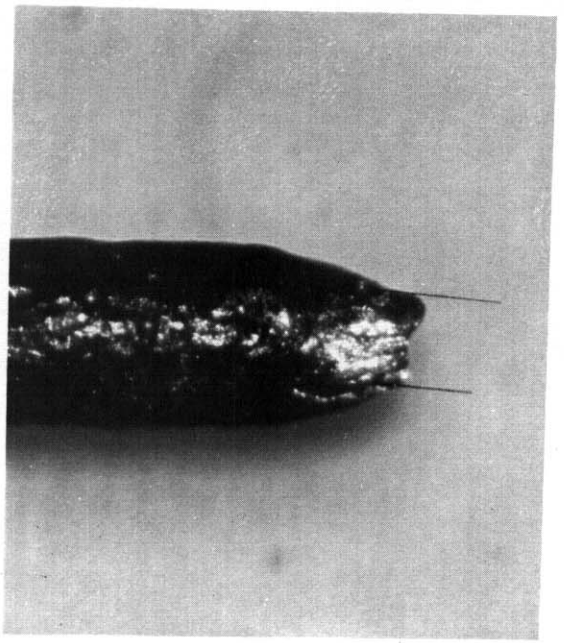

Fig. 2.6.8: Micrograph of the fractured region (100X).

ORNL DWG 79 18723

FABRICATION *OF* THE PATH A PRIME CANDIDATE ALLOY

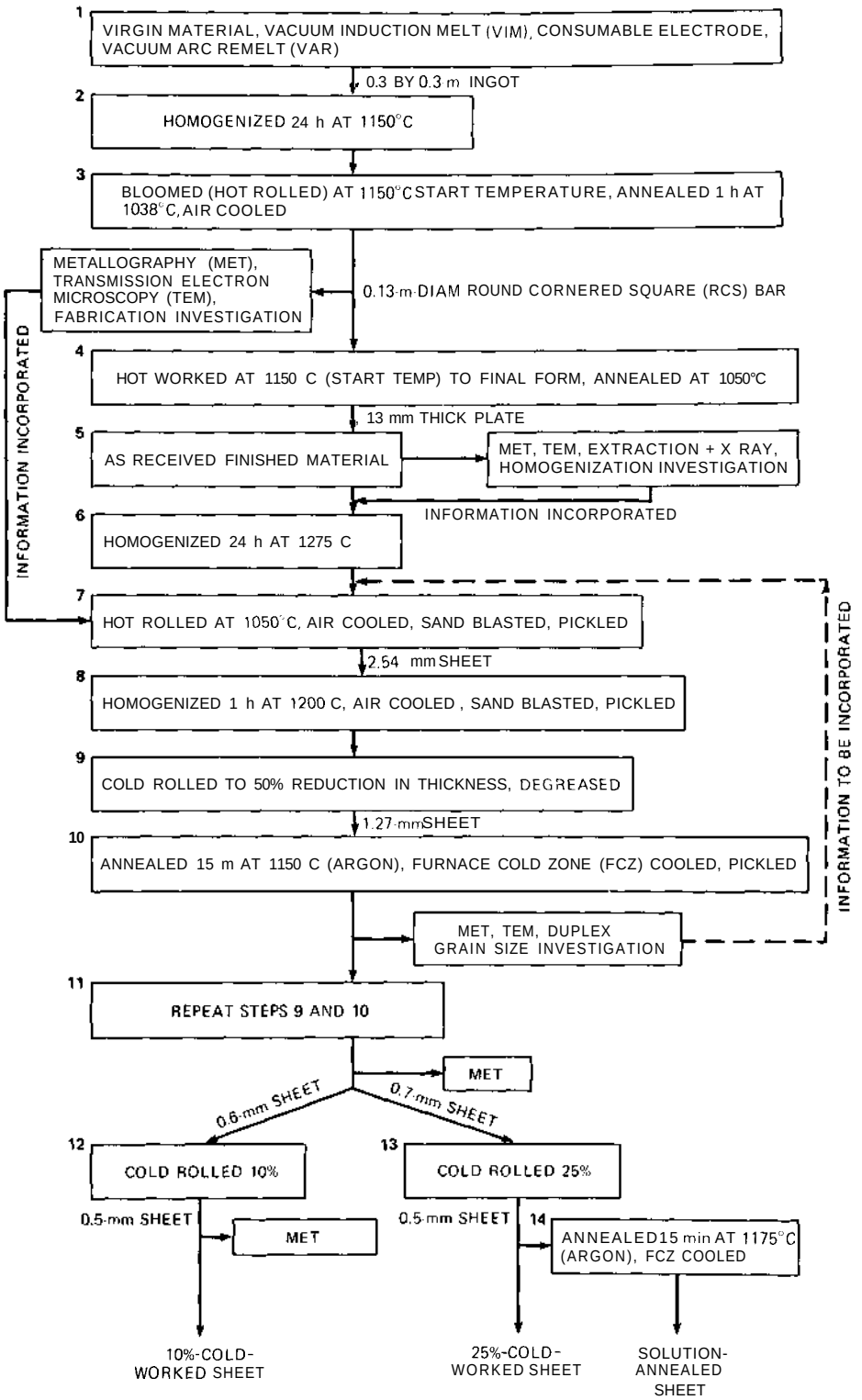

Fig. 3.2.1. Flow Chart of the Fabrication Sequence Used to Produce Path A Prime Candidate Alloy (PCA) 0.5-mm-Thick Sheet for Transmission Electron Microscopy Specimens.

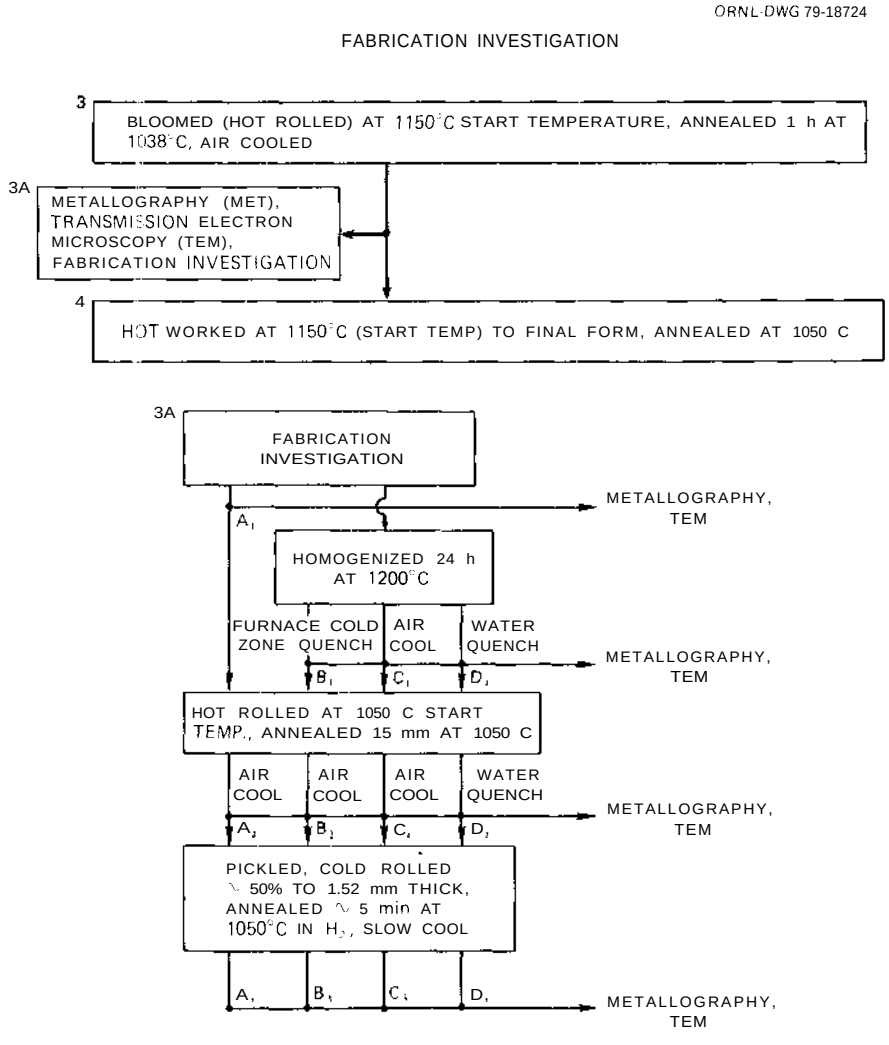

Fig. 3.2.2. Details of the Fabrication Analysis Prompted by Observations of Stringers and Fine Undissolved Titanium-Rich MC Particles Between Steps 3 and 4 and in Fig. 3.2.1.

material. This investigation showed that the initial material must be homogenized, that hot working was acceptable at 1050°C (starting temperature), and that fine MC precipitate particles should be dissolved by solution treating at 1150 to 1200°C before each cold deformation step to prevent stringering.

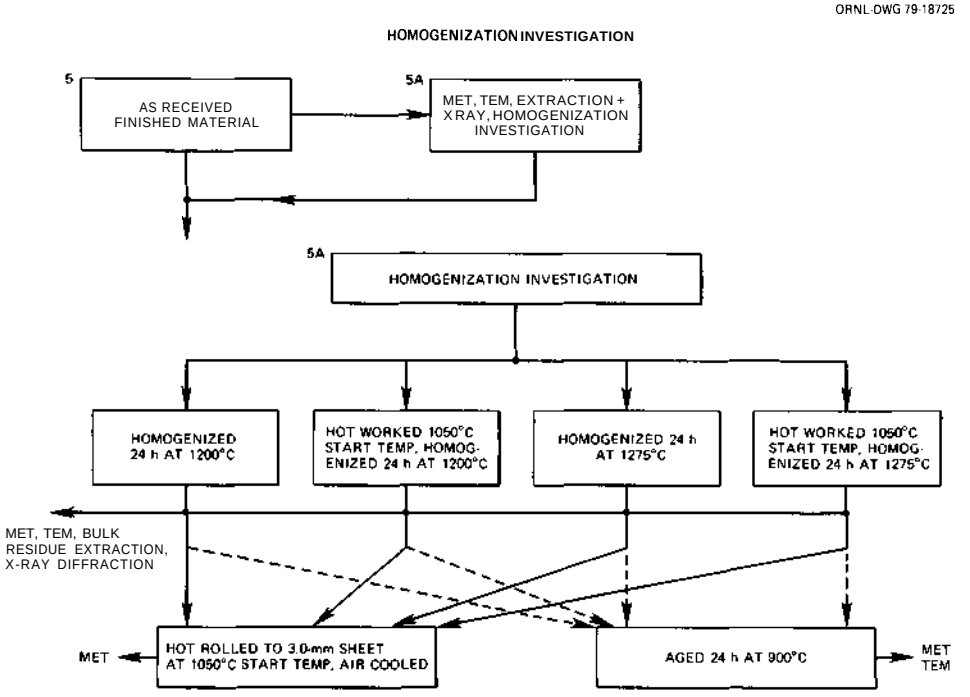

Fig. 3.2.3. Details of the Homogenization Treatment Investigation Prompted by Inhomogeneous MC Particle Distributions Observed in the As-Received PCA Material.

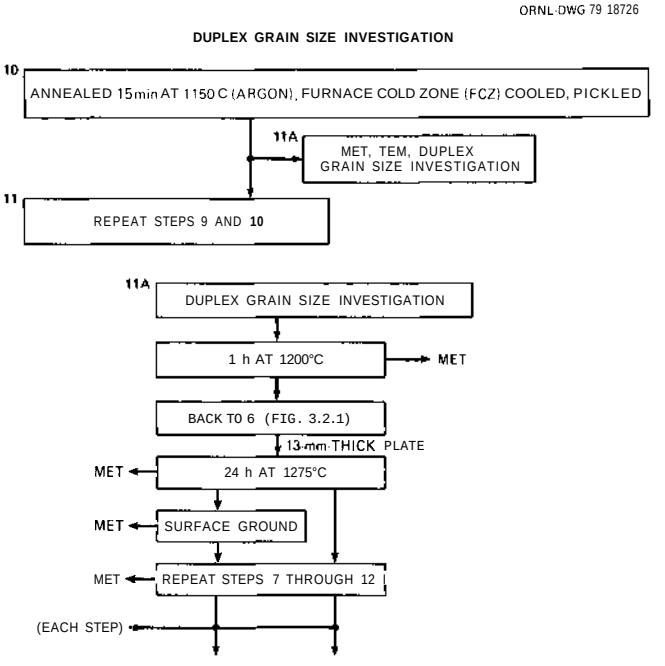

Fig. 3.2.4. Details of the Investigation to Find the Cause of the Near-Surface Stringer of Particles Resulting in a Duplex Grain Size after Recrystallization Following Cold Working.

The homogenization investigation shown in Fig. 3.2.3 (see step 5, Fig. 3.2.1) was initiated to overcome severe macro- and microscopic inhomogeneity (see Fig. 3.2.5) of titanium-rich MC and hence titanium content. The fabrication investigation in Fig. 3.2.2 showed how a microstructure like this could develop from improper homogenization. Figure 3.2.3 shows the homogenizing treatments investigated, including long times (24 h) at high temperatures. We also considered breaking up the stringers through hot work before homogenization.

Several tests were used to evaluate the level of homogenization achieved. The ability to dissolve the titanium-rich MC particles was revealed by optical metallography (Fig. 3.2.6), transmission electron microscopy (TEM) (Fig. 3.2.7), and bulk precipitate extraction with weighing and x-ray diffraction analysis of the residue (Table 3.2.1).

The subsequent tests of aging at 900°C for 24 h (Figs. 3.2.8 and 3.2.9) or processing by hot working following homogenization (Fig. 3.2.10) revealed the level of redistribution of titanium achieved by homogenization.[4,5] Figures 3.2.6 and 3.2.7 showed that all homogenization treatments were able to dissolve fine MC and most of the coarser MC particles and that the 1275°C treatment appears to dissolve slightly more MC than the 1200°C treatment. This is confirmed by the weights of extracted residues in Table 3.2.1. These also confirm that the hot working did little to improve the homogeneity and was therefore unnecessary. Figures 3.2.8, 3.2.9, and 3.2.10 reveal that the reprecipitated MC particles are reasonably uniform so that homogenization was successful. Therefore, we selected a homogenization treatment of 24 h at 1275°C. However, as will be pointed out later, this is a severe treatment for time, temperature, and protective atmosphere requirements and would not have been necessary if proper homogenization had been carried out by the vendor earlier in the processing.

We proceeded with fabrication of sheet, starting at step 7 of Fig. 3.2.1 after homogenization. The fabrication sequence steps were selected based on our fabrication variable shown in Fig. 3.2.2.1 We homogenized the material 1 h at 1200°C after hot working as a precaution to ensure that MC particles formed during hot working would be dissolved before the first cold-work step.

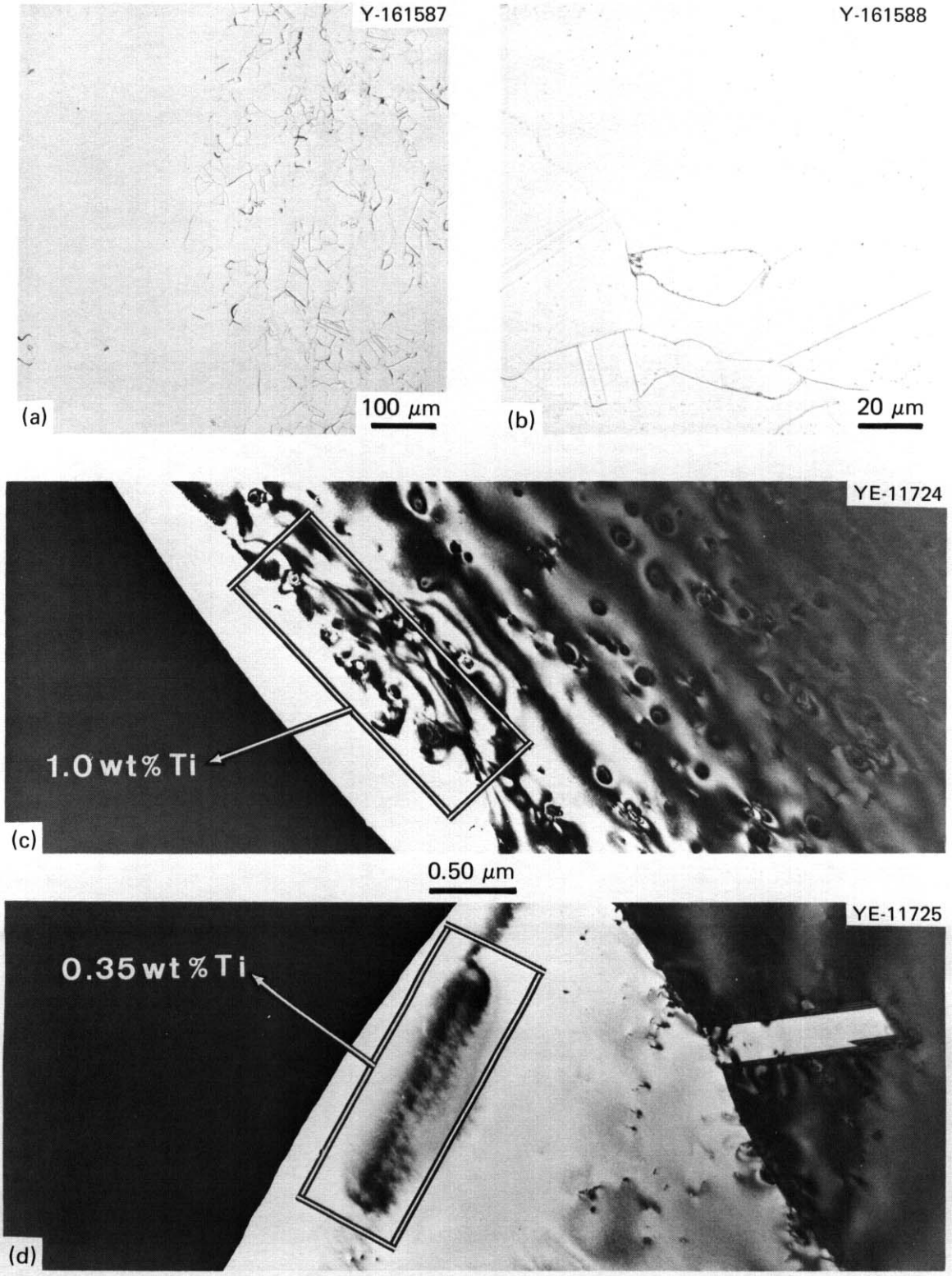

Fig. 3.2.5. Microstructure of the As-Received 13-mm-Thick Plate. Optical metallography reveals gross variations in grain size and stringers of MC precipitates in (a) and (b). Transmission electron microscopy of adjacent portions of thin area shows variation in titanium-rich MC particle concentration. Microanalysis with x-ray energy dispersive spectroscopy (EDS) shows the corresponding variation in average titanium concentration.

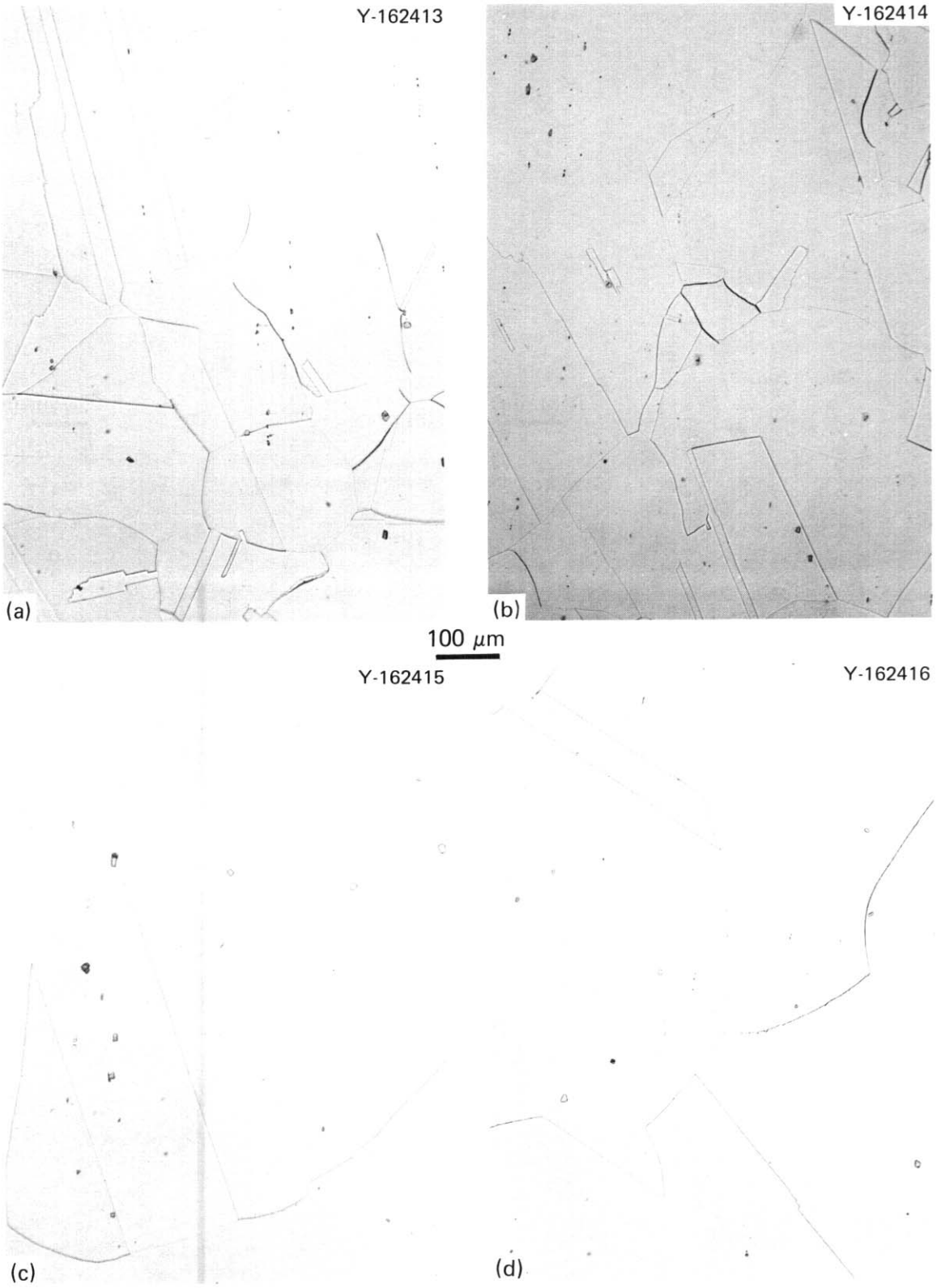

Fig. 3.2.6. Optical Metallography of the Homogenized Microstructures After (a) 24 h at 1200°C, (b) Hot Work at 1050°C (Starting Temperature) plus 24 h at 1200°C, (c) 24 h at 1275°C, and (d) Hot Work at 1050°C (Starting Temperature) plus 24 h at 1275°C. Slightly better particle dissolution is achieved at 1275°C.

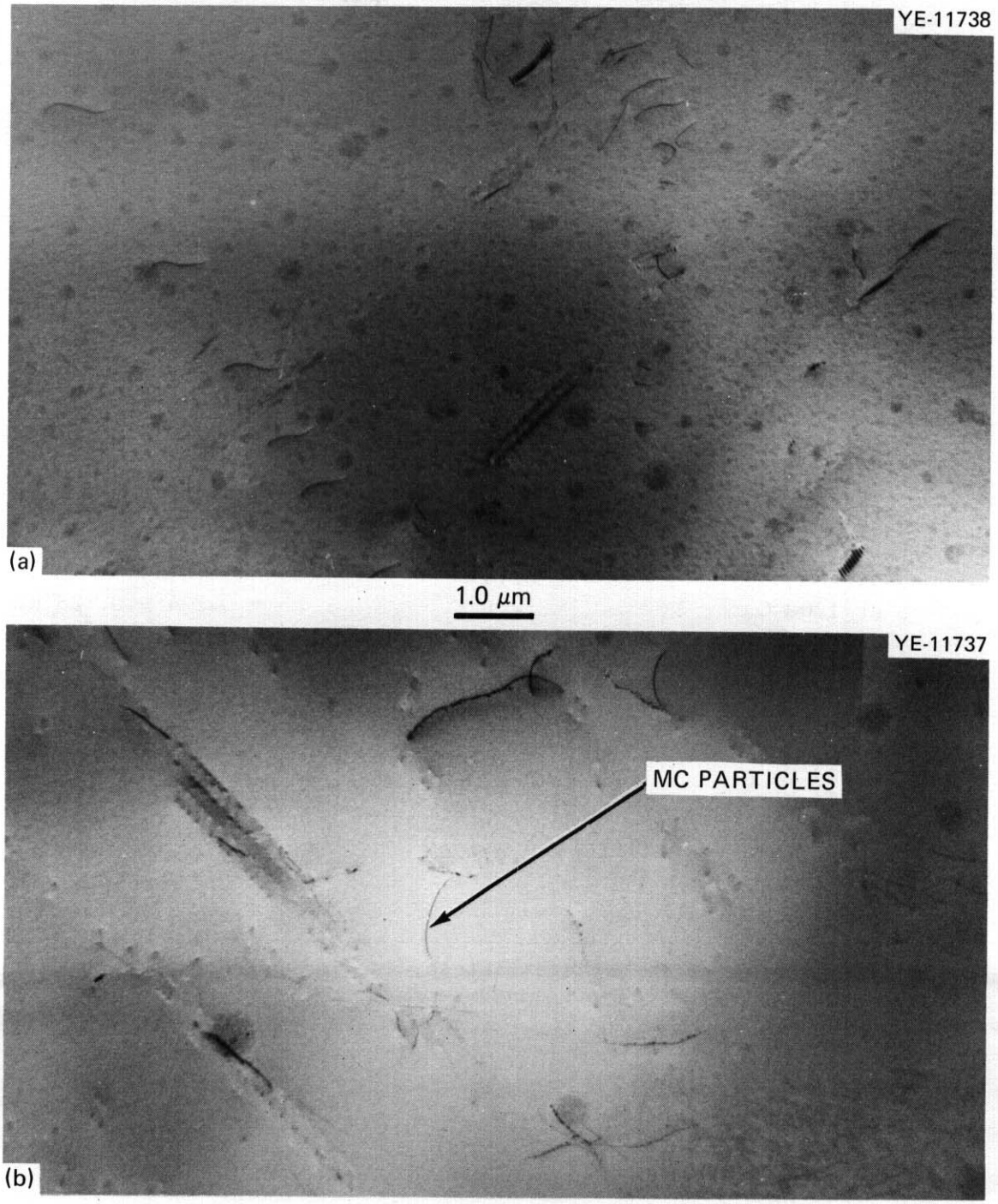

Fig. 3.2.7. Transmission Electron Microscope Micrographs of Path A Prime Candidate Alloy (PCA) After Homogenization at 1275°C for 24 h. Views (a) and (b) are adjacent areas. (a) No titanium MC particles. (b) Occasional, fine MC particles on dislocations produced during cooling. However, this is a considerable improvement over the as-received material.

Table 3.2.1. Amount of Precipitate in Extracted Residue for Selection of an Adequate Homogenization Treatment

Condition	Amount of Precipitate (wt %)	Composition from X-Ray Diffraction Analysis
As received	0.16 ± 0.03	(Ti,Mo) (C,N)[a] a_0 = 0.224 - 0.228 nm
As received + 24 h at 900°C	0.45	Not measured
Homogenized 24 h at 1200°C	0.10	(Ti,Mo) (C,N) a_0 = 0.224 – 0.228 nm
Hot worked (1050°C) + homogenized 24 h at 1200°C	0.12	(Ti,Mo) (C,N) a_0 = 0.224 – 0.228 nm
Homogenized 24 h at 1275°C	0.08	(Ti,Mo) (C,N) a_0 = 0.224 - 0.228 nm
Hot worked (1050°C) + homogenized 24 h at 1275°C	0.07	(Ti,Mo) (C,N) a_0 = 0.224 – 0.228 nm

[a] Ti(C,N)S, a blocky orange paticle, is also present. It neither grows nor dissolves at these temperatures.

2. P. J. Maziasz, "Microstructural Design for Fusion First-Wall Applications and Recommendations for Thermal-Mechanical Preirradiation Treatments," *ADIP Quart. Prog. Rep. June 30, 1979,* DOE/ET-0058/6, pp. 48–56.
3. D. E. Strohecker, A. F. Gerds, H. J. Henning, and F. W. Boulger, *Deformation Processing of Stainless Steel,* NASA TM X-53569 (Oct. 21, 1966).
4. D. N. Braski and J. M. Leitnaker, "Homogenization of Ti-Hastelloy-N," *Metall. Trans.* 10A: 427 (1979).
5. J. M. Leitnaker and J. Bentley, "Precipitate Phases in Type 321 Stainless Steel After Aging 17 Years at ~600°C," *Metall. Trans.* 8A: 1605–13 (1977).
6. J. M. Leitnaker and R. E. Gehlbach, *Thermodynamics of Precipitation Reactions in Titanium-Modified Stainless Steel,* ORNL/TM-4543 (July 1974).

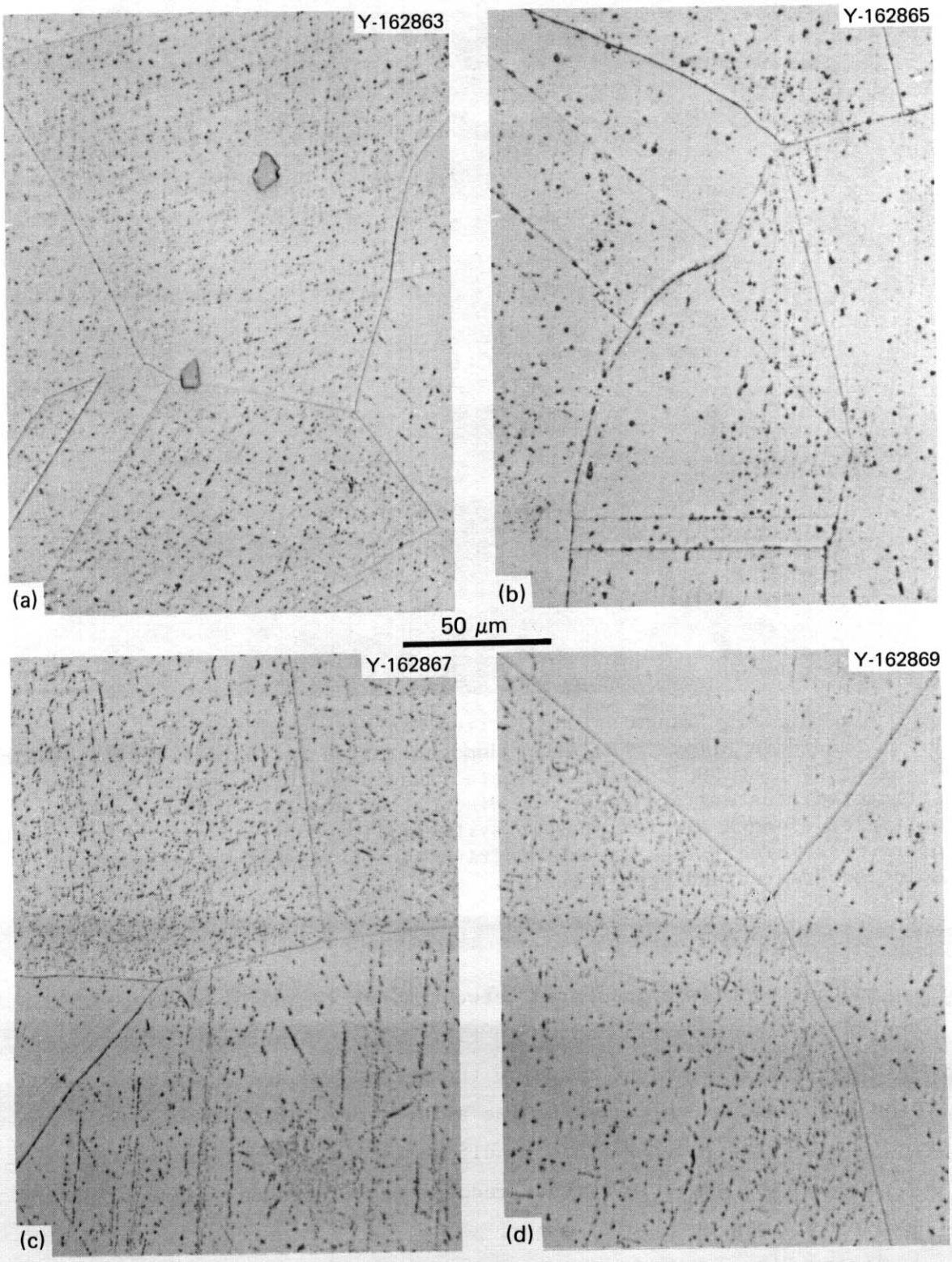

Fig. 3.2.8. Optical Metallography of the Microstructures Produced by Aging 24 h at 900°C After the Following Homogenization Treatments: (a) 24 h at 1200°C, (b) Hot Work at 1050°C (Starting Temperature) plus 24 h at 1200°C, (c) 24 h at 1275°C, and (d) Hot Work at 1050°C (Starting Temperature) plus 24 h at 1275°C.

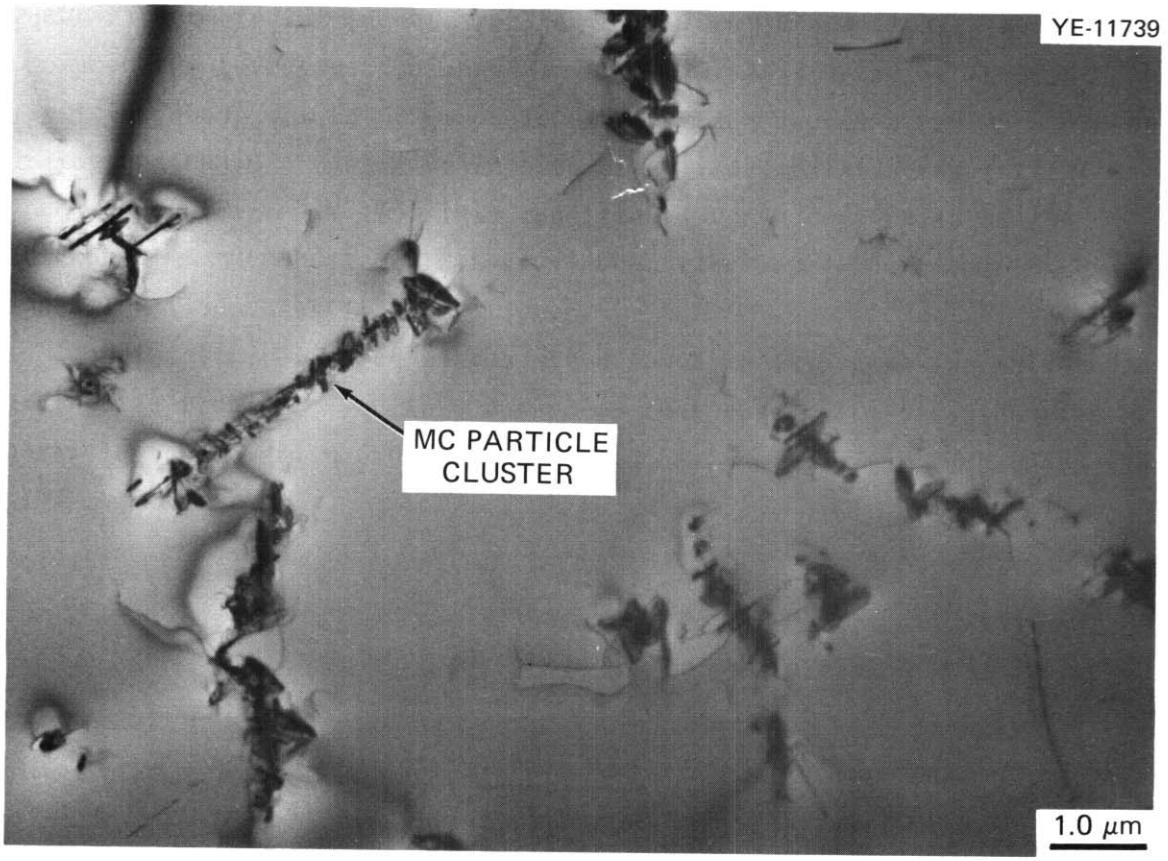

Fig. 3.2.9. Transmission Electron Microscope Micrograph of Path A Prime Candidate Alloy (PCA) After Homogenization of 24 h at 1275°C, Followed by Aging 24 h at 900°C to Precipitate Titanium-Rich MC Particles. The stringered clusters are caused by dislocation generation from growing particles along a particular slip system followed by nucleation and growth of new particles. The spacial distribution of clusters is typical of solution-treated and aged material.

Another problem encountered between steps 10 and 11 of Fig. 3.2.1 prompted the investigation shown in Fig. 3.2.4. A stringer of fine particles about 0.1 to 0.2 mm below the surface caused a string of small grains and hence a duplex grain size after recrystallization in 1.27-mm-thick sheet (Fig. 3.2.11) This condition is seen to persist as the thickness of the sheet is further reduced with repeated cold rolling and annealing (15 min at 1150°C) steps.

Again, Fig. 3.2.4 shows the steps taken in investigating this duplex grain size problem. We first suspected that these were titanium-rich MC particles that were not dissolved at 1150°C, but the fact that there was

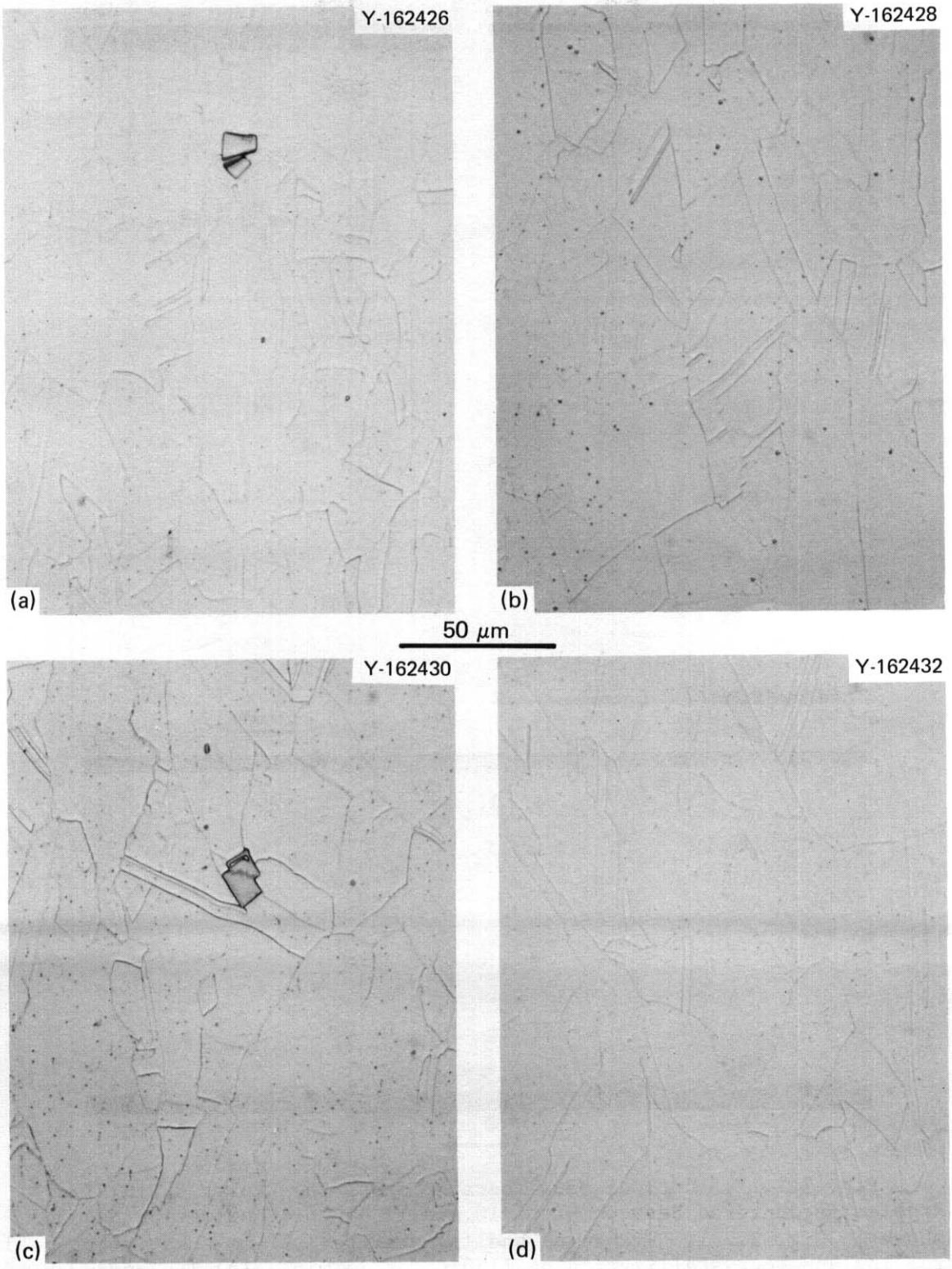

Fig. 3.2.10. Optical Metallography of Microstructures Produced by Hot Working at 1050°C from 13- to 3.3-mm-Thick Sheet After the Following Homogenization Treatments: (a) 24 h at 1200°C, (b) Hot Work at 1050°C (Starting Temperature) plus 24 h at 1200°C, (c) 24 h at 1275°C, and (d) Hot Work at 1050°C (Starting Temperature) plus 24 h at 1275°C.

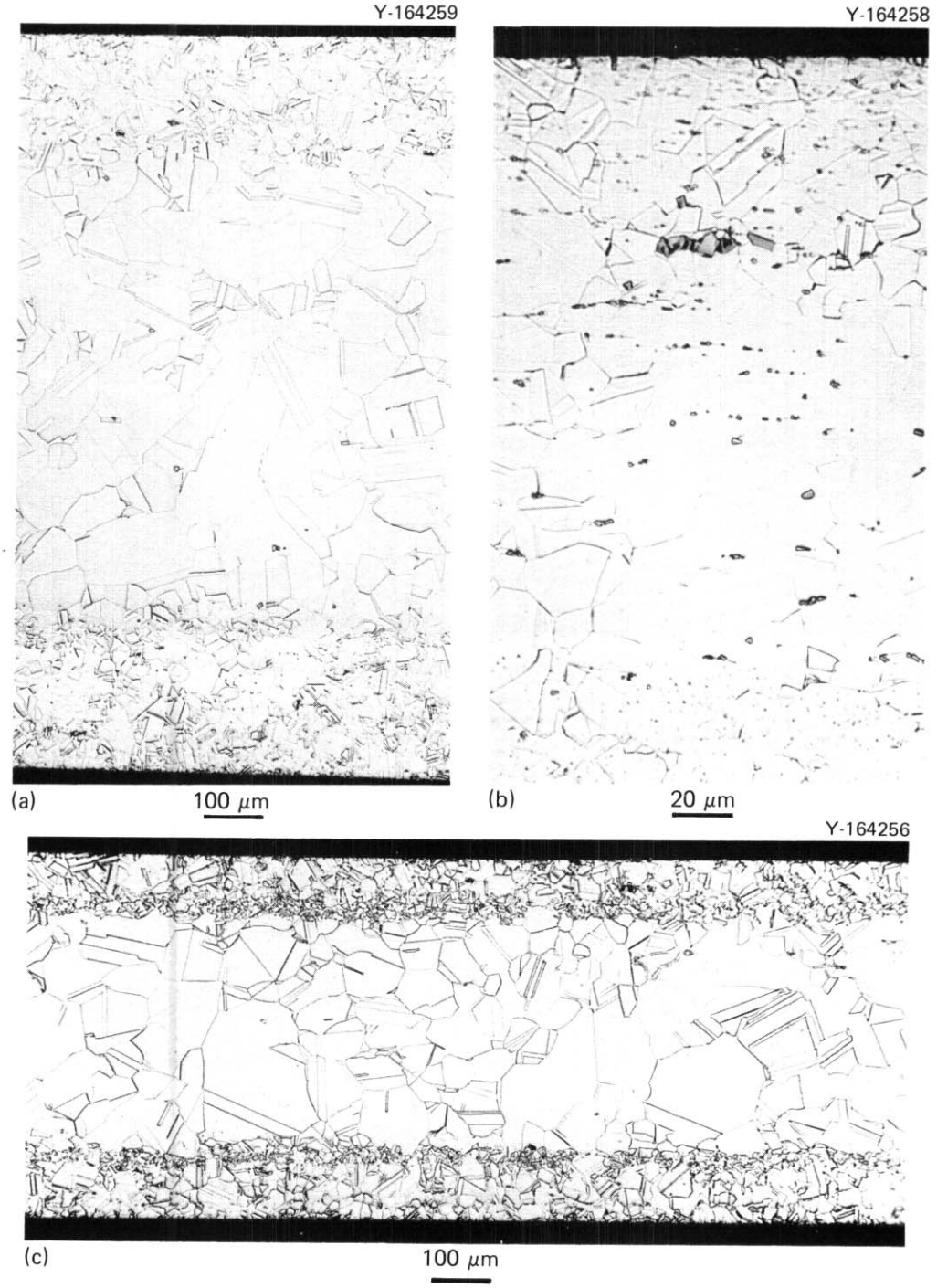

Fig. 3.2.11. Optical Metallography Shows the Duplex Grain Size Problem Encountered Between Steps 10 and 11 of the Fabrication Sequence shown in Fig. 3.2.1. Views (a) and (b) are the 1.27-mm-sheet after cold rolling and recrystallization at 1150°C for 15 min. (a) The stringer of fine grains is parallel but beneath the rolling surface. (b) The fine particles of titanium-rich nitrides are responsible for the duplex grain size. (c) The problem persists as the material is cold rolled and recrystallized to 0.6-mm-thick sheet.

no change after 1 h at 1200°C seemed to indicate that they were nitride rather than carbide particles. At temperatures below about 1150°C, two potentially competing chemical reactions are:

$$[Ti]_\gamma + [C]_\gamma \rightarrow [TiC]_\gamma ,$$

and

$$[Ti]_\gamma + [N]_\gamma \rightarrow [TiN]_\gamma ,$$

where []y refers to those species dissolved in austenite. The amounts of product and reactants that can coexist at equilibrium are given by

$$\Delta G^\circ = AH - TAS , \quad (1)$$

and

$$\Delta G^\circ = -RT \ln \frac{a_{TiC}}{a_{Ti} a_C} , \quad (2)$$

where *a* represents activities, and other terms have their usual thermodynamic definitions. Similar equations can be written for the TiN reaction. Leitnaker and Gehlbach[6] calculated these reactions in type 316 austenitic stainless steels. From their work,

$$\Delta G^\circ_{1473\ K}(TiC) = -184.5\ kJ - (-11.8\ J/mol\ K)(1473K) = -167\ kJ , \quad (3)$$

and

$$\Delta G^\circ_{1473\ K}(TiN) = -337.6\ kJ - (-82.6 J/mol\ K)(1473\ K) = -216\ kJ . \quad (4)$$

Clearly we can see that the nitride is the more stable phase on a free energy basis. (The nitride value disagrees with that given by Leitnaker and Gehlbach[6] because of a numerical error in their calculation.) But the equilibrium amount of each phase is also determined by the activities of titanium, carbon, and nitrogen in the alloy. For carbon

$$C(graphite) \rightleftharpoons [C]_\gamma , \quad (5)$$

$$\Delta G_C = 4.52 \times 10^4\ J - (61.8\ J/mol\ K)T = RT \ln a_C , \quad (6)$$

and

$$\ln a_C = (4.52 \times 10^4 - 61.8T)/RT .$$

This result indicates that for a given concentration of carbon, the activity decreases as the temperature increases. Nitrogen and titanium behave similarly so that at some temperature TiC or TiN will dissolve, as observed. Because of the larger negative enthalpy of formation, this corresponds to TiN dissolving at a higher temperature than TiC for equal carbon and nitrogen concentrations. This temperature is about 1150°C for the titanium-rich MC in the Path A PCA for about 0.25 to 0.3 wt % Ti and 0.05 wt % C but is above the melting point of type 316 for the titanium-rich MN. Thus at: the homogenization temperature of 1275°C, the reactions become

$$[Ti]_\gamma + [C]_\gamma \leftarrow [TiC]_\gamma ,$$

and

$$[Ti]_\gamma + [N]_\gamma \rightarrow [TiN]_\gamma .$$

If nitrogen is available titanium-rich MN will form at 1275°C because the titanium concentration increases as the MC dissolves. The equilibrium pressure of nitrogen for this reaction is in the order of 10^{-5} to 10^{-6} Pa so that for higher pressures nitriding will proceed at some rate determined by the kinetics of the reaction. Equipment limitations required use of an air furnace and a protective layer around the steel. However, even this was not adequate, and considerable nitriding occurred beneath the surface oxide scale. This can be seen in the as-homogenized material in Fig. 3.2.12(a). The nitriding was eliminated by grinding this material off the billet, and a cross section through the ground surface is shown in Fig. 3.2.12(b). The unground billet then received exactly the same treatment as the ground billet. Figure 3.2.13 shows that the unground billet duplicated the duplex grain size shown in Fig. 3.2.12, while surface grinding had eliminated the problem. However, care must be taken with grinding because the depth of penetration varies from sample to sample. If the nitride particles are not completely removed, they still stringer during fabrication. The final 0.5-mm sheet had some near-surface stringers, but the bulk of the interior of the material was acceptable and homogeneous. Transmission electron microscope discs were punched from this material and were used to examine the thermal aging response of the microstructure. Electropolishing and thinning during specimen

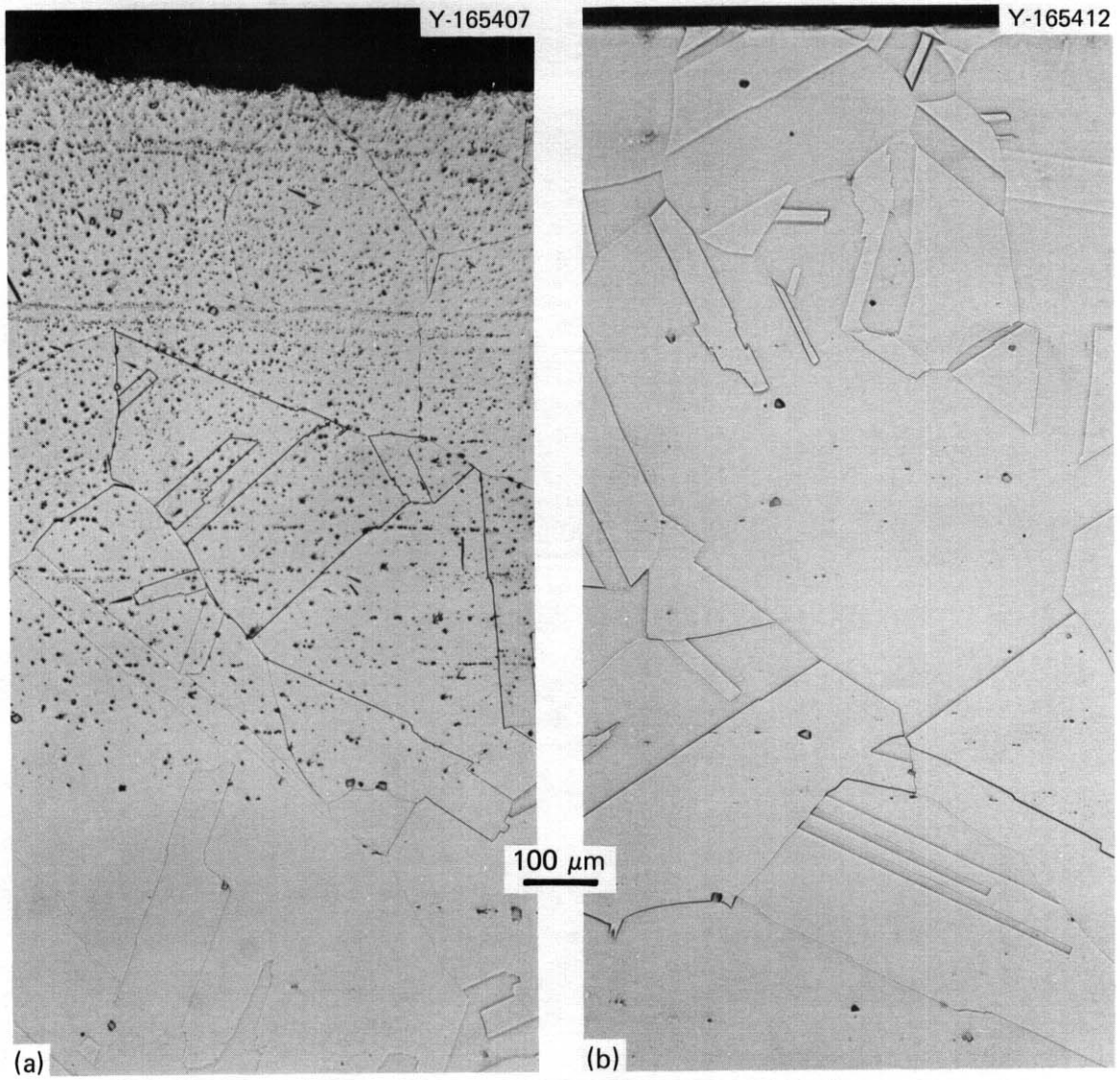

Fig. 3.2.12. Optical Metallography of a Cross Section Through the Rolling Surface of a Billet of 13-mm-Thick Plate Stock After Homogenization at 1275°C for 24 h in an Air Furnace. The rolling surface is shown at the top of the figure. (a) The particles are titanium-rich nitrides. (b) These particles are removed by surface grinding of the rolling billet after homogenization.

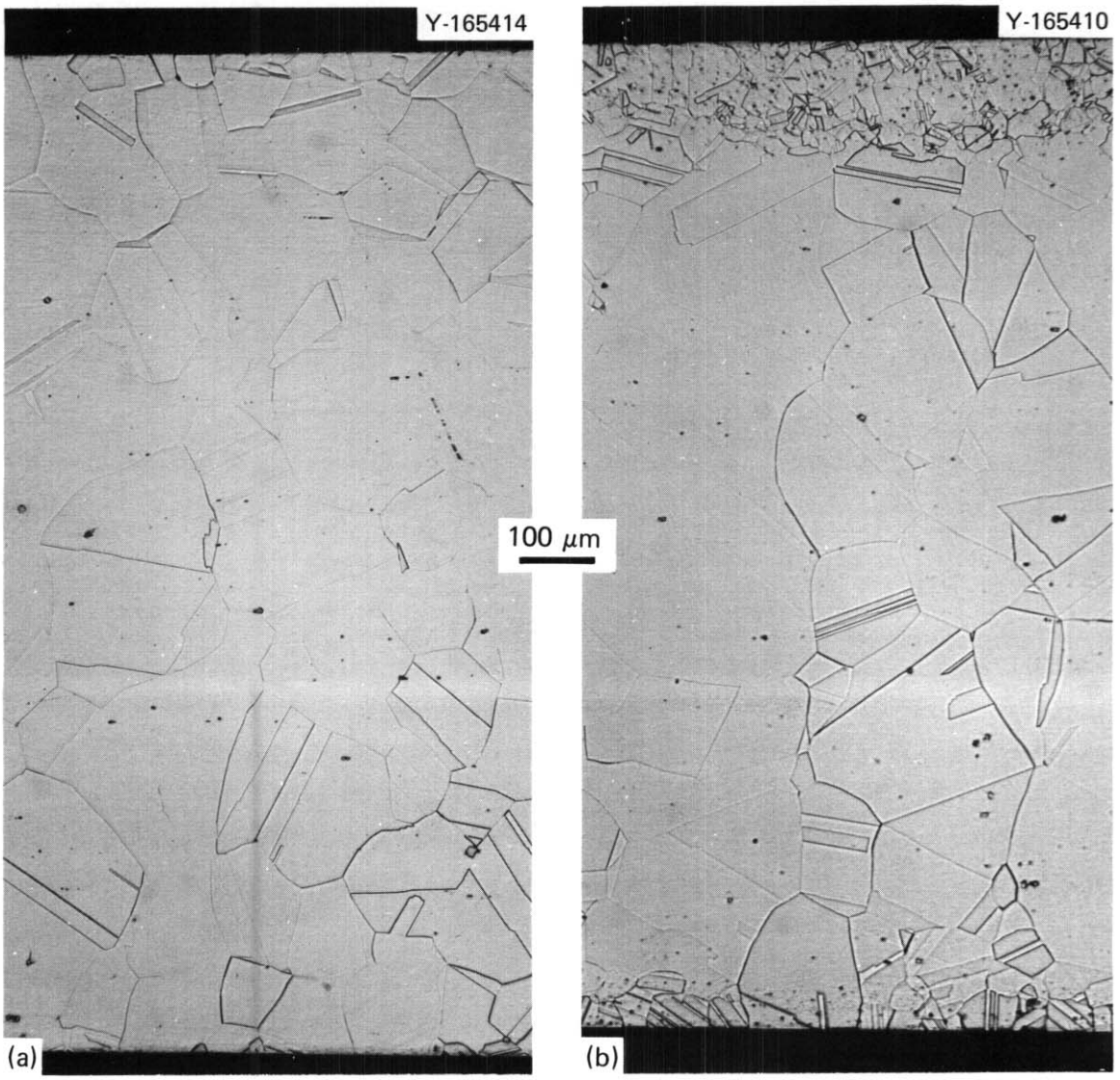

Fig. 3.2.13. Subsequent Fabrication of Both Ground and Unground Rolling Billets to Step 10 in the Fabrication Sequence of Fig. 3.2.1. (a) Structure indicates that a uniform, homogeneous microstructure can be produced by surface grinding plus proper fabrication. (b) Sheet fabricated from unground rolling billet. Similarity to the microstructure shown in Fig. 3.2.11(a) indicates that the problem was nitriding of the surface during homogenization.

preparation removed the surface material, and thus the aging response should be unaffected. However, specimens for future irradiation experiments will be fabricated with a schedule incorporating all the solutions to the various problems.

3.2.5 Conclusions

A successful fabrication sequence produced homogeneous specimen material from the as-received Path A PCA. The problems encountered and their solutions are as follows:

1. The as-received material was too inhomogeneous for microstructural design. The solution was to homogenize the alloy for 24 h at 1275°C.

2. Fabrication at elevated temperatures produces initially fine titanium-rich MC particles that can coarsen and redistribute upon further deformation. Heating to at least 1150°C is required to redissolve MC. The solution was hot worked at 1050°C (starting temperature) with 1 h at 1200°C to rehomogenize it before cold working. Each cold-work step was followed by annealing at 1150 to 1175°C to redissolve MC particles precipitated during recrystallization.

3. Stringers of fine titanium-rich nitride particles developed below the rolling surface and caused a duplex grain size upon recrystallization after cold rolling. The particles formed at the surface during homogenization for 24 h at 1275°C in a poorly controlled atmosphere. The solution for this material was to grind the surface after homogenization to remove the nitrides. However, better results are expected if large pieces are homogenized to reduce surface area, if some type of sacrificial encapsulation is included, or if the air is replaced with static inert gas or vacuum.

The fabrication principles discussed above should be applicable to other product forms and similar modified austenitic stainless steels as well. However, with proper precautions fabrication of the modified alloys can still be fairly easy and straightforward.

3.2.6 References

1. P. J. Maziasz and T. K. Roche, "Microstructural Characterization of As-Received Prime Candidate Alloy and Examination of Microstructural Sensitivity to Fabrication and Processing Variables," *ADIP Quart. Prog. Rep. Mar. 31, 1979,* DOE/ET-0058/5, pp. 36–62.

3.3 TIME-TEMPERATURE-PRECIPITATION CURVE DETERMINATION OF THE PATH A PRIME CANDIDATE ALLOY FOR MICROSTRUCTURAL DESIGN - P. J. Maziasz, B. L. Cox, T. K. Roche, and E. E. Bloom (ORNL)

3.3.1 ADIP Tasks

ADIP Tasks I.A.5, Fabrication Analysis, and I.C.I, Microstructural Stability.

3.3.2 Objective

The primary objective of this work is to examine the short-term thermal aging responses of the Path A Prime Candidate Alloy (PCA) at several cold-worked levels (0, 10, and 25%) to determine whether the conceptually designed preirradiation microstructures can be produced in the PCA. This data can also be compared to types 316 and titanium-modified 316 austenitic stainless steel to indicate differences in the PCA microstructural response. Finally, this information can be used to understand the observed fabrication behavior and to define the final thermal-mechanical steps of specimen material fabrication.

3.3.3 Summary

Thermal aging of the Prime Candidate Alloy (PCA) with no cold working and with 10 and 25% cold working for time-temperature-precipitation (TTP) curve determination shows that MC precipitate particle distribution, either at the grain boundary or in the matrix, is considerably more sensitive to initial dislocation density than to either time or temperature. Fine spacial and size distributions of matrix MC precipitate particles can be achieved in 25%-cold-worked PCA after as little as 5 min at 750°C. The formation of MC precipitate particles helps control phase instability by retarding intragranular precipitation of $M_{23}C_6$, eta, and Laves phases in the PCA as in titanium-modified type 316 stainless steel. The increase in nickel and decrease in chromium of the PCA relative to titanium-modified type 316 also appear to retard intergranular $M_{23}C_6$ and/or eta phase formation, thus allowing titanium-rich MC to replace them as the grain boundary phase in the PCA. Occasional Laves phase particles precipitate at the grain boundaries of the PCA, as they also do in

titanium-modified type 316. These differences in response of the PCA relative to titanium-modified type 316 forced us to reevaluate the conceptual preirradiation microstructural design. However, the ease of MC precipitation and the variety of particle distributions available, together with better resistance to formation of undesirable phases, make the PCA superior to types 316 or titanium-modified 316 stainless steel. Thermal-mechanical treatments have been developed to yield the designed preirradiation microstructures.

3.3.4 Progress and Status

We previously specified[1] the desirable preirradiation microstructures for the PCA, which were based upon the results of High Flux Isotope Reactor (HFIR) irradiation of solution-annealed and 20%-cold-worked types 316 and titanium-modified 316 austenitic stainless steel. These microstructures and the recommended thermal-mechanical treatments necessary to create them were based upon the assumption that the PCA thermal aging response resembled that of titanium-modified type 316. The suggested microstructures are listed and described in Table 3.3.1. The chemical compositions of types 316 and titanium-modified 316 and the PCA are listed in Table 3.3.2. Though both titanium-modified type 316 and the PCA contain more titanium (0.23 to 0.25 wt %) than type 316 stainless steel (<0.05 wt %), their concentrations of most of the other intentionally added alloying elements are similar. The PCA is higher in nickel and lower in chromium than type 316. The free-precipitation thermal aging response of solution-annealed, 10 and 25%-cold-worked PCA should give information about possible microstructural variations and about how to achieve desired microstructural features.

Details of the fabrication of 0.5-mm sheet are given in Chap. 3.2 of this report. Transmission electron microscope (TEM) discs 3.0 mm in diameter were punched from either 10 or 25%-cold-worked material. Solution-annealed material was produced by annealing 25%-cold-worked discs in argon at 1175°C for 15 min. The aging matrix for all three microstructural conditions covers temperatures from 600 to 1100°C in increments of 50°C with times from 5 min to 166 h. Selected samples expected to be relevant to microstructural design have been examined.

Table 3.3.1. Suggested Preirradiation Microstructures for Titanium-Modified Austenitic Stainless Steels

A. Simple microstructure with "free" precipitation resulting from:
   1. solution annealing,
   2. 5 to 10% cold working, or
   3. 20 to 25% cold working.

B. Microstructures with intragranular titanium-rich MC, no grain boundary precipitation, and an MC precipitate particle density of:
   1. 1×10^{20} particles/m^3,
   2. 1×10^{21} particles/m^3, or
   3. 1×10^{22} particles/m^3.

C. Microstructures with intragranular titanium-rich MC, grain boundary $M_{23}C_6$ and/or eta phase, and an MC precipitate particle density of:
   1. 1×10^{20} particles/m^3,
   2. 1×10^{21} particles/m^3, or
   3. 1×10^{22} particles/m^3.

D. Microstructures with intragranular and grain boundary titanium-rich MC and an intragranular MC precipitate particle density of:
   1. 1×10^{20} particles/m^3,
   2. 1×10^{21} particles/m^3, or
   3. 1×10^{22} particles/m^3.

Table 3.3.2. Composition of Three Austenitic Stainless Steels

Alloy	Content, wt %[a]										
	Cr	Ni	Mo	Mn	C	Ti	Si	P	S	N	B
316	18.0	13.0	2.58	1.90	0.05	0.05	0.80	0.013	0.016	0.05	0.0005
316+Ti	17.0	12.0	2.50	0.5	0.06	0.23	0.40	0.01	0.013	0.0055	0.0007
PCA	14.0	16.2	2.3	1.8	0.05	0.24	0.4	0.01	0.003	0.01	0.0005

[a]Balance iron.

Discs were thinned to electron transparency by standard methods. Both the matrix and the grain boundaries were examined for evidence of precipitation and for phase identification.

Partial TTP curves for solution-annealed, 10 and 25%-cold-worked PCA material are shown in Figs. 3.3.1, 3.3.2, and 3.3.3, respectively. In the solution-annealed material grain boundary precipitation of titanium-rich MC began early compared to matrix precipitation. Figure 3.3.4 shows the

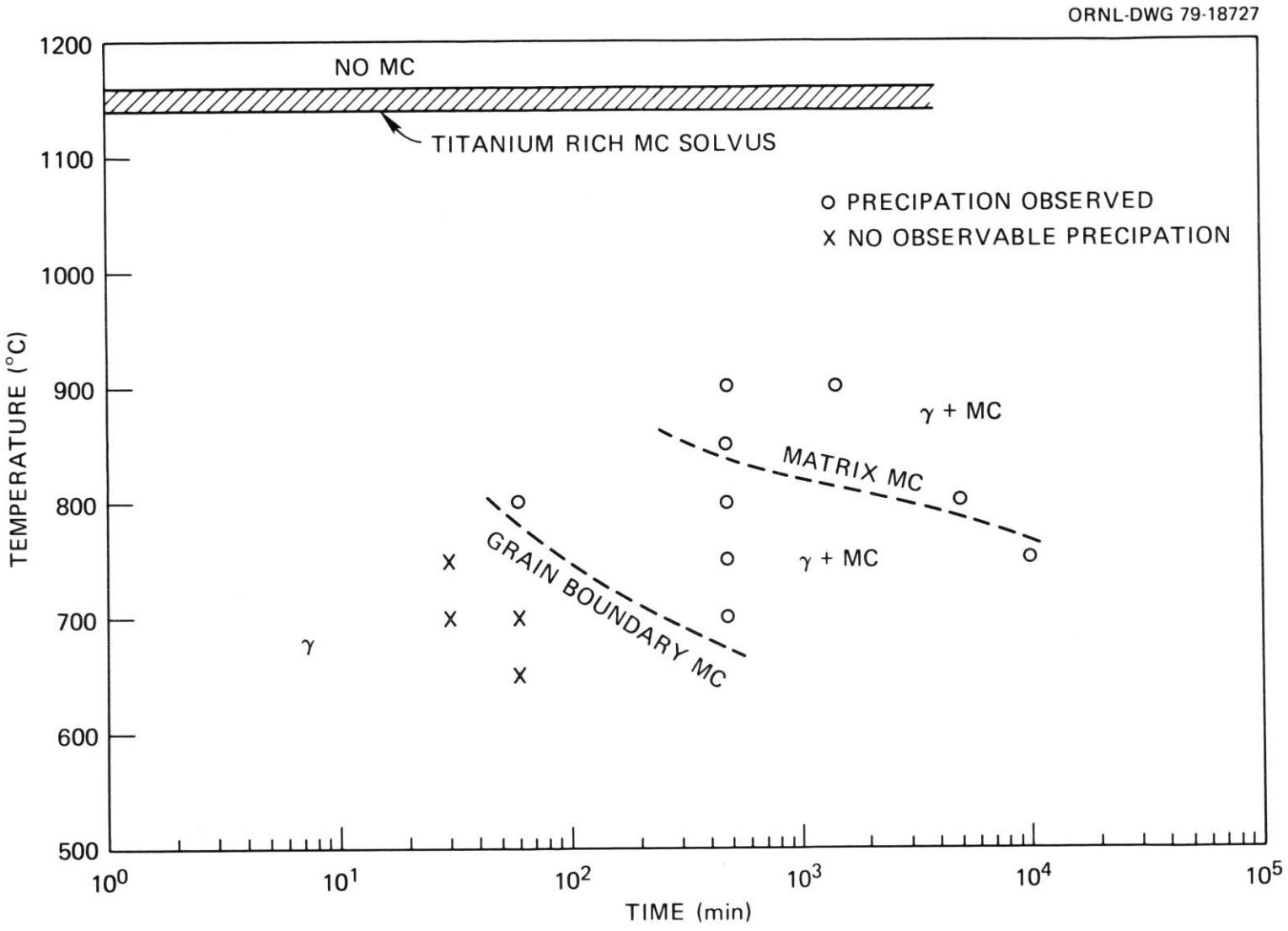

Fig. 3.3.1. Time-Temperature-Precipitation (TTP) Curve for Path A Prime Candidate Alloy (PCA) that Has Been Solution Annealed 15 min at 1175°C.

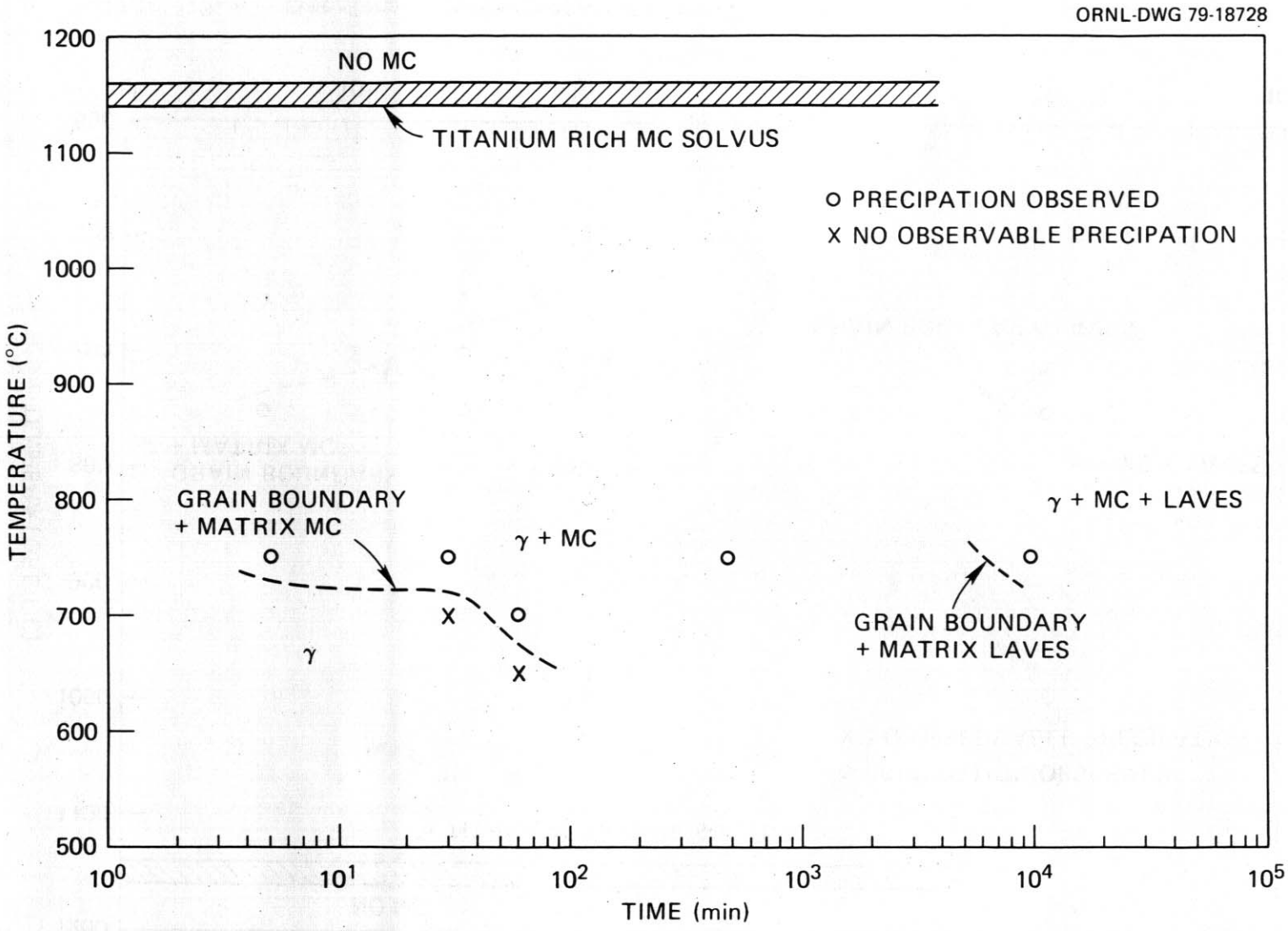

Fig. 3.3.2. Time-Temperature-Precipitation (TTP) Curve for Path A Prime Candidate Alloy (PCA) that Has Been 10% Cold Worked (Rolling).

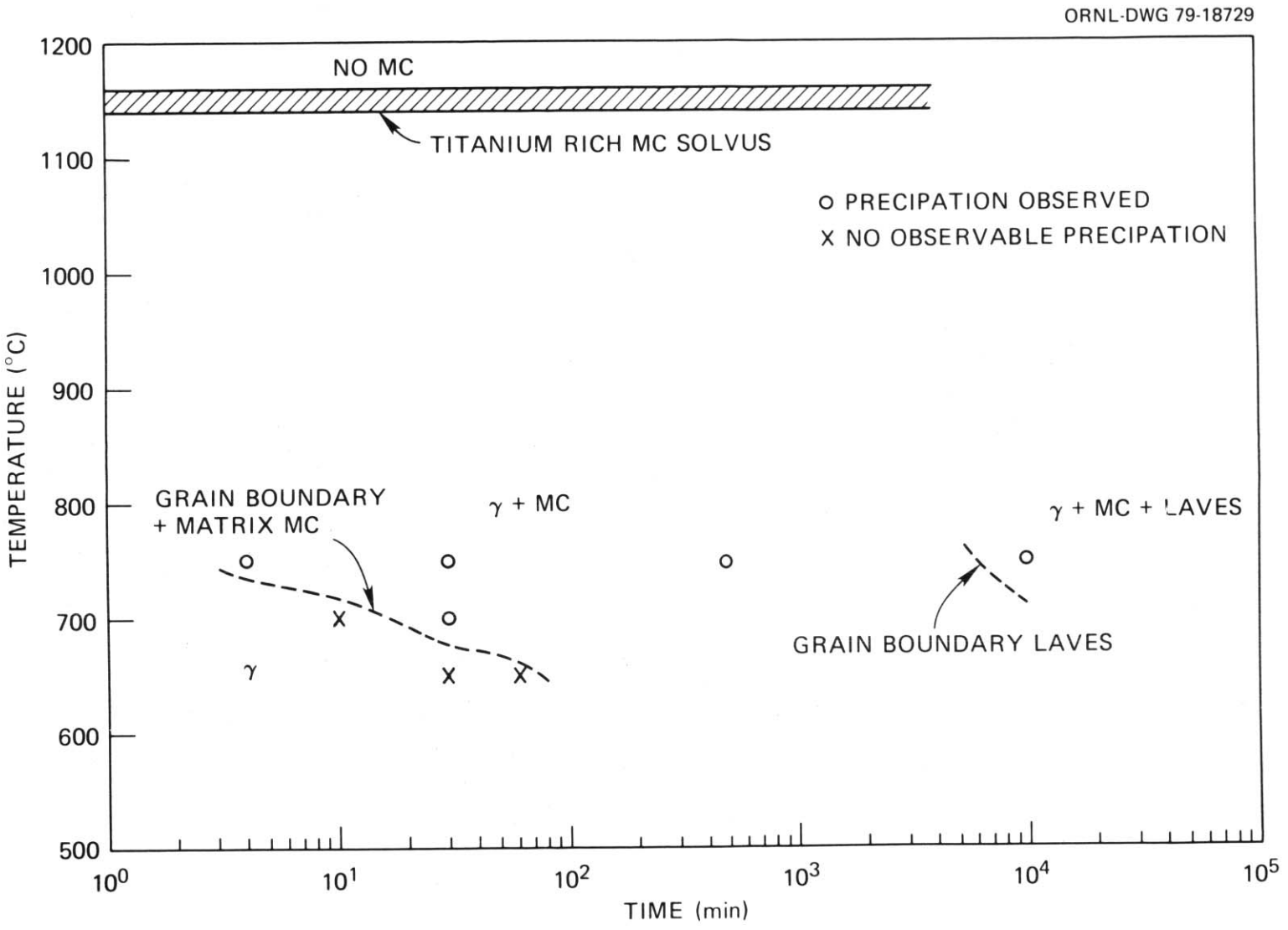

Fig. 3.3.3. Time-Temperature-Precipitation (TTP) Curve for Path A Prime Candidate Alloy (PCA) that Has Been 25% Cold Worked (Rolling).

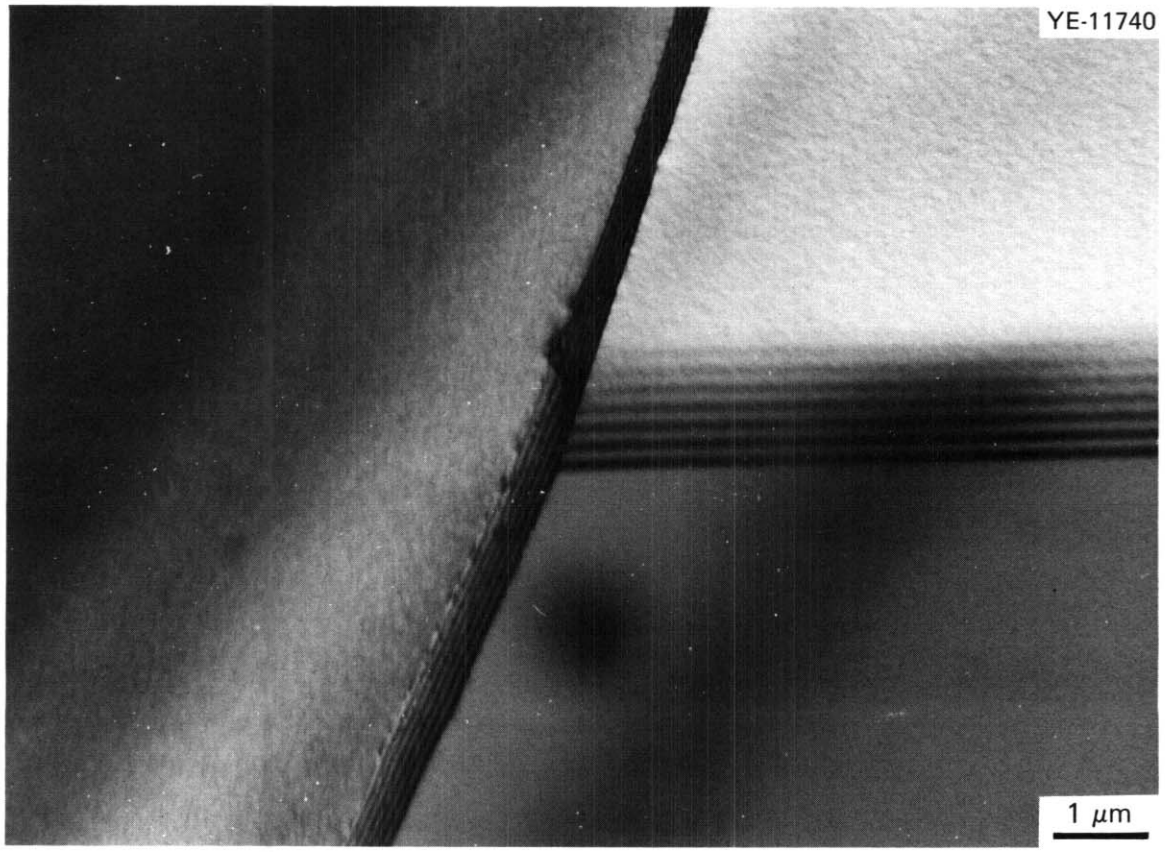

Fig. 3.3.4. Prime Candidate Alloy (PCA) that Has Been Solution Annealed 15 min at 1175°C and Aged 60 min at 700°C Shows No MC Precipitation.

grain boundary condition before MC precipitation in solution-annealed 0.5-mm-thick sheet. A few randomly distributed MC particles remain after annealing, but matrix precipitation is not visible. Figure 3.3.5 shows several grain boundaries containing MC particles after aging 8 h at 700, 800, and 900°C. The size increases abruptly and the density decreases with aging temperature from 700 to 800°C. The density then increases with little change in size with aging temperatures from 800 to 900°C. After 8 h at 700°C the grain boundary MC particles are about 10 nm, and at 900° they are 30 to 80 nm. The grain boundary particles coarsen little with increasing aging times up to about 100 h. The particles are generally epitaxial with one grain and grow into that grain. There appears to be considerable misfit strain between the particles and their associated grain.

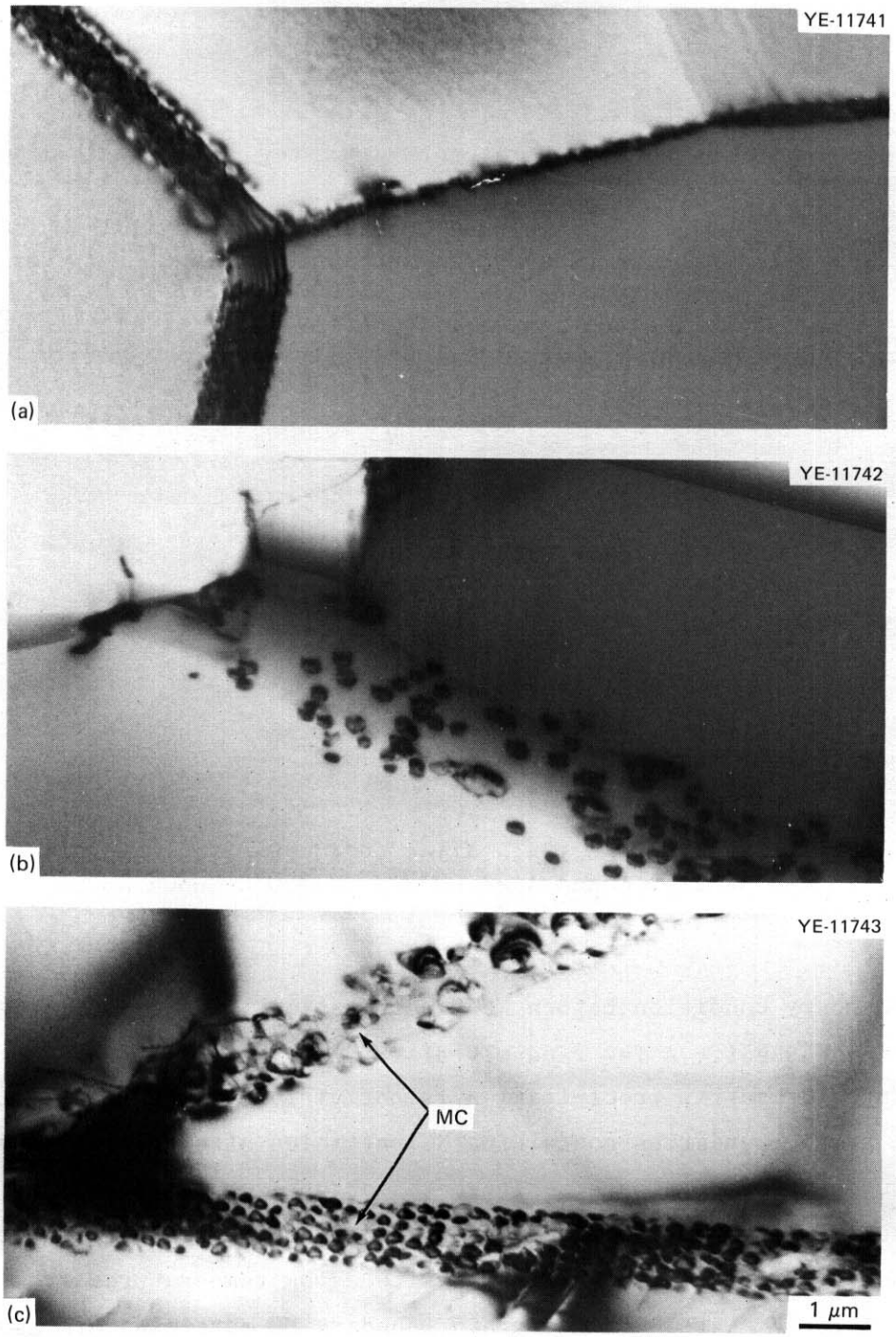

Fig. 3.3.5. Grain Boundary MC Precipitation in Solution-Annealed (15 min at 1175°C) Prime Candidate Alloy (PCA) after Aging for 8 h at: (a) 700, (b) 800, and (c) 900°C. With temperatures from 700 to 800°C, high-density fine particles change to fewer, coarser particles. The particle density again increases with little size change from 800 to 900°C.

Figure 3.3.6 shows matrix precipitation of MC in solution-annealed PCA material after aging at 800°C for 100 h and at 900°C for 8 h. Particles that range from 150 to 400 nm form clusters that decrease in size and increase in number density as temperature increases. It is well known[2] that MC precipitate particles usually nucleate on dislocations. Precipitate particle growth requires vacancies to accommodate the approximately 21% difference in lattice parameter for the same face-centered cubic crystal structure while maintaining an epitaxial orientation relationship. The particles can punch out dislocations, and climb of these dislocations can supply needed vacancies.

Figures 3.3.2 and 3.3.3 show that precipitation of titanium-rich MC particles is considerably enhanced by cold working before aging. For 25%-cold-worked PCA both matrix and grain boundary precipitation occur after 5 min at 750°C. Precipitation of MC in 25%-cold-worked material is only slightly enhanced relative to 10%-cold-worked material. The grain boundary and matrix MC precipitate almost simultaneously for the temperatures and times examined. Fine MC precipitate particles can only be detected by combined bright-field and dark-field imaging in the TEM. After very short-time aging of 25%-cold-worked PCA at 700 to 750°C, the matrix MC precipitate particle density is about 2×10^{22} particles/m^3, and the particle size appears no more than 1 nm, as shown in Figs. 3.3.7 and 3.3.8. After aging 25%-cold-worked PCA at 750°C for 166 h, both the precipitate particle and dislocation densities are slightly reduced and the matrix dot MC particles range from about 1 to 4 nm, as shown in Fig. 3.3.9. The grain boundary particle size is about 2 to 20 nm in 25%-cold-worked PCA and nearly the same size as matrix dot MC particles (1 to 2 nm) for grain boundaries in 10%-cold-worked PCA [compare Fig. 3.3.8(b) and 3.3.10(d)]. The matrix MC precipitate particle distributions are similar for 10 and 25%-cold-worked PCA, but the grain boundary MC precipitate particles are coarser in the 25%-cold-worked material. The structures in both appear quite stable for aging temperatures up to 750°C and times up to about 166 h. The precipitate particle size and distribution depend little on temperature. Figure 3.3.10 shows the distribution of MC in 10%-cold-worked PCA aged for 30 min at 750°C. The primary difference between annealed and cold-worked materials is the dislocations for nucleation of

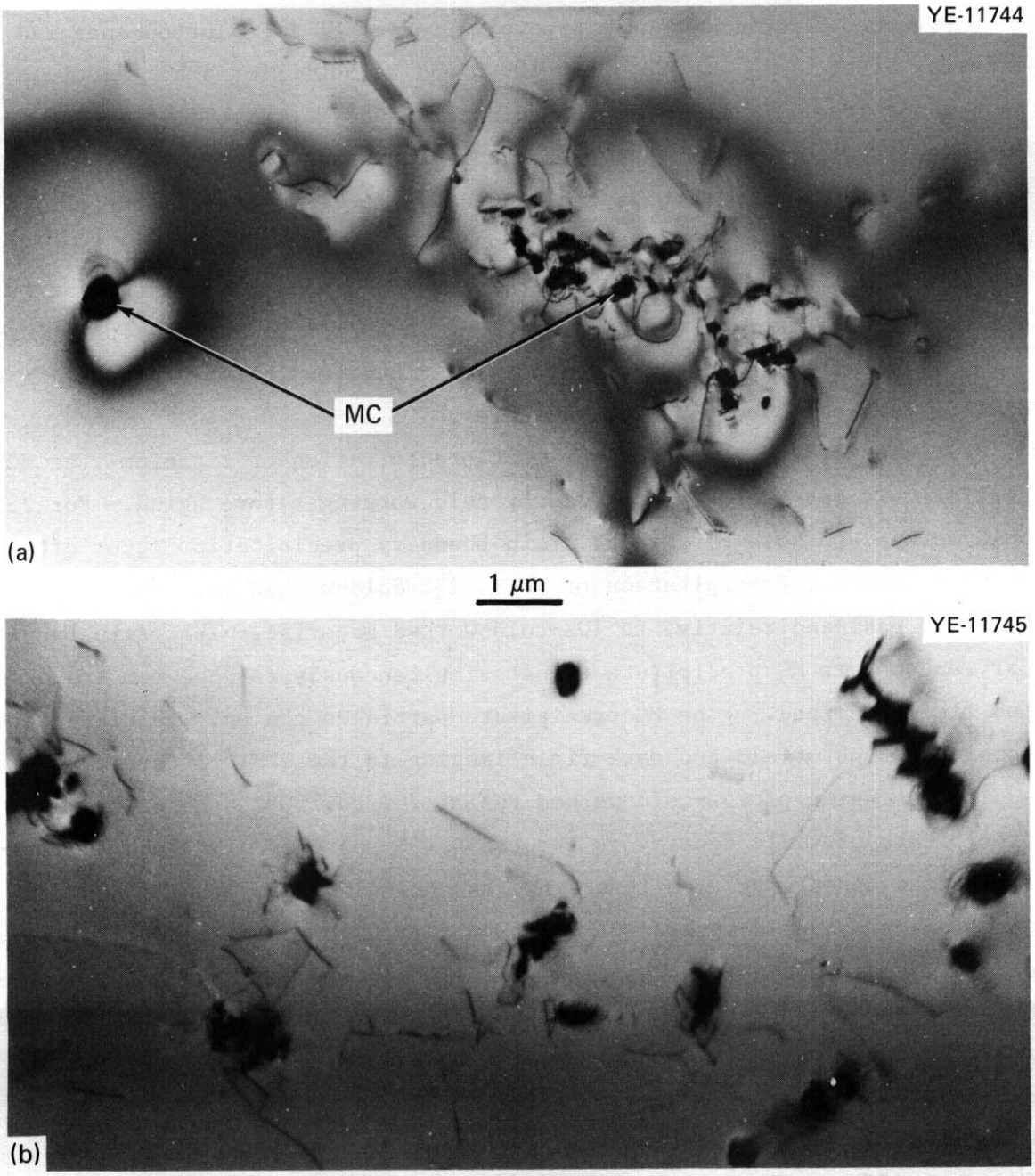

Fig. 3.3.6. Matrix MC Precipitation in Solution-Annealed (15 min at 1175°C) Prime Candidate Alloy (PCA) Thermally Aged at: (a) 800°C for 100 h and (b) 900°C for 8 h. The particles are similar in size and tend to cluster. The cluster size decreases and number density increases with increasing temperature.

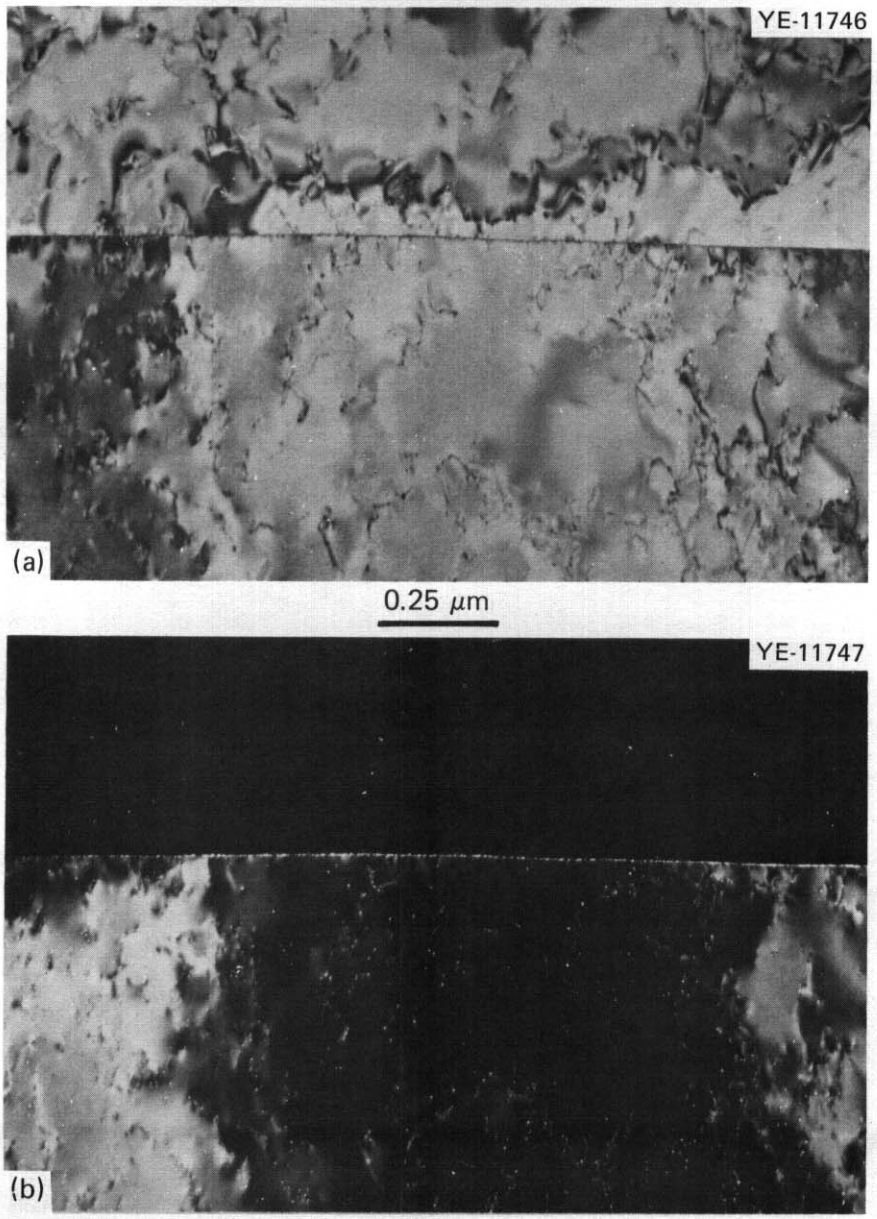

Fig. 3.3.7. The 25%-Cold-Worked Prime Candidate Alloy (PCA) After Thermal Aging at 700°C for 30 min. (a) Bright field with (111) matrix reflection. (b) Dark field with (111) MC reflection. Note the fine MC particles at the boundary and in the matrix.

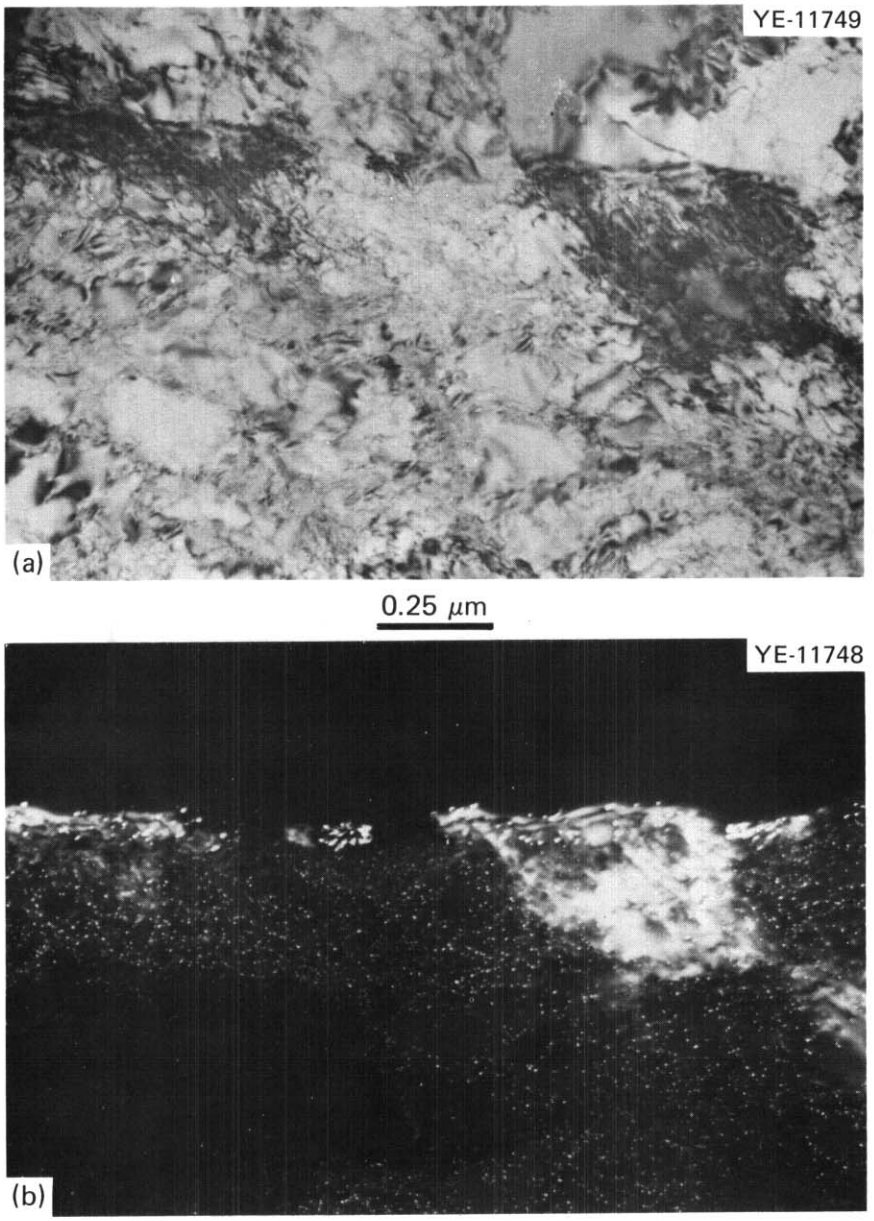

Fig. 3.3.8. The 25%-Cold-Worked Prime Candidate Alloy (PCA) After Thermal Aging at 750°C for 5 min. (a) Bright field with (111) matrix reflection. (b) Dark field with (111) MC reflection.

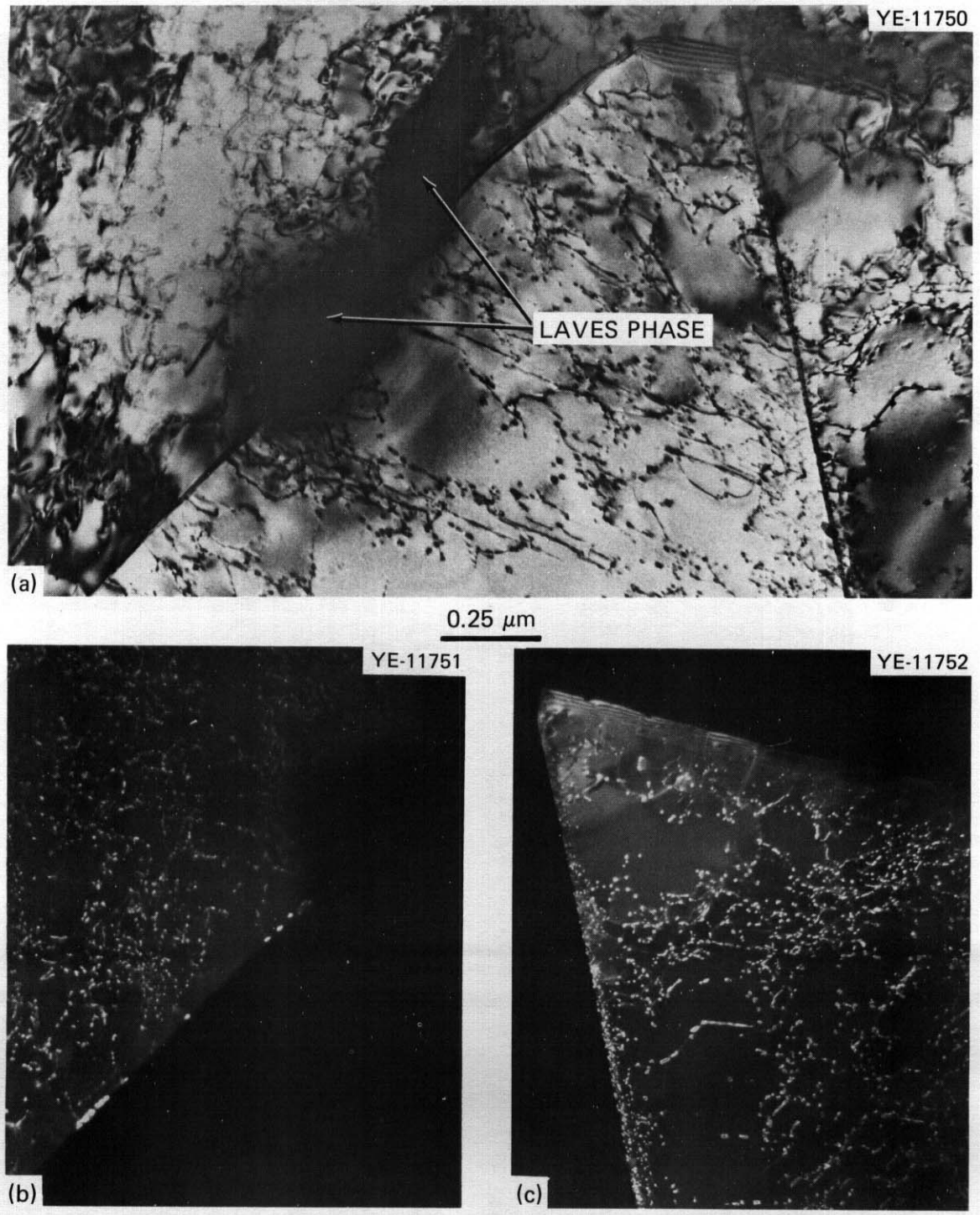

Fig. 3.3.9. The 25%-Cold-Worked Prime Candidate Alloy (PCA) Thermally Aged at 750°C for 166 h. (a) Bright field with (111) matrix reflection in the two outer left and right grains. (b) and (c) Dark fields with (111) MC reflection. The MC precipitate particle size and density varies from boundary to boundary, and Laves phase has begun to appear at the grain boundaries.

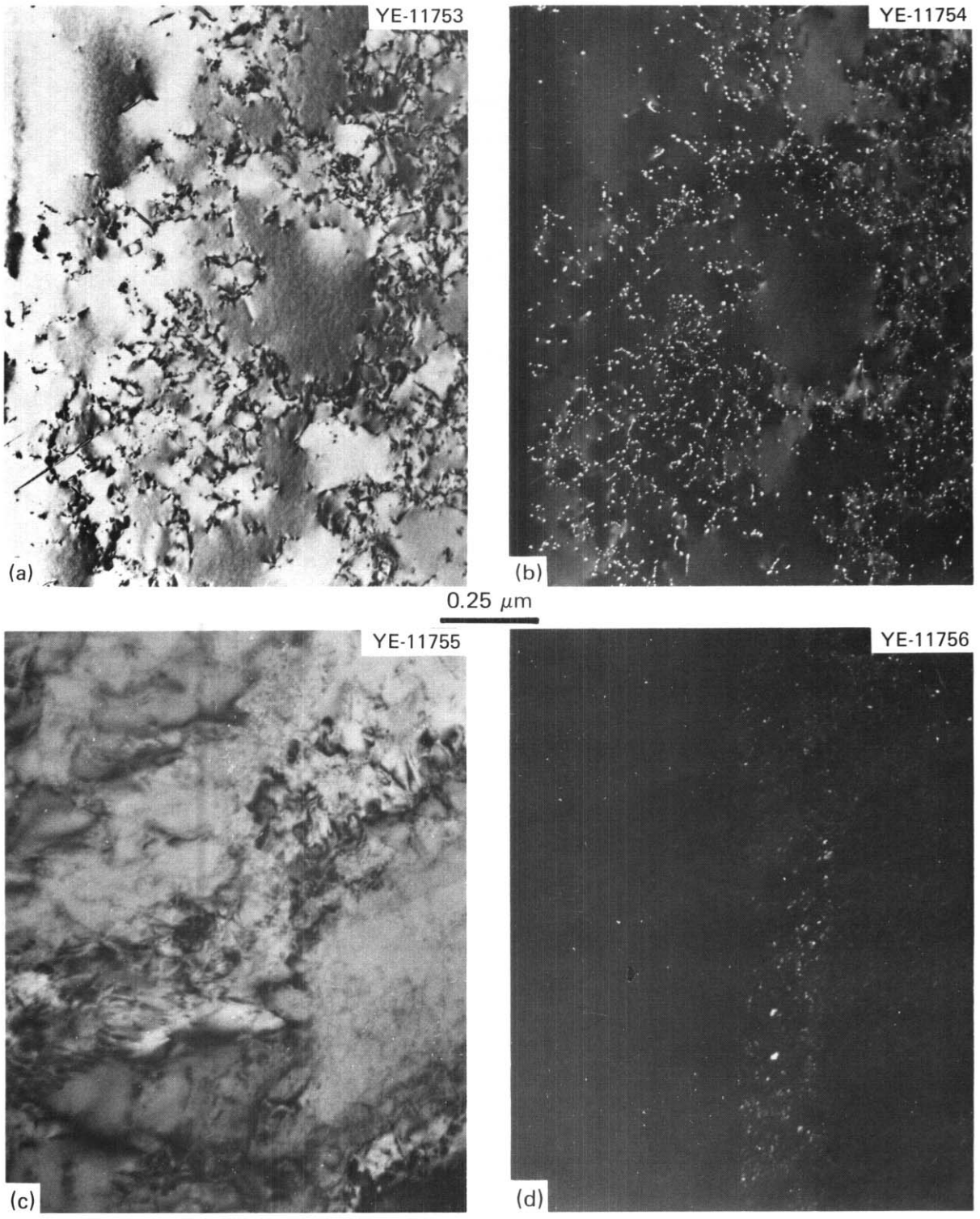

Fig. 3.3.10. The 10%-Cold-Worked Prime Candidate Alloy (PCA) Thermally Aged at 750°C for 30 min. (a) Bright field of matrix with (200) matrix reflection. (b) Dark field of matrix with (200) MC reflection. (c) Bright field of grain boundary with (200) matrix reflection. (d) Dark field of grain boundary with (200) MC reflection. Note the very fine MC particles at the boundary.

the particles. Upon aging solution-annealed material, dislocation generation and climb on a given slip system within the grain followed by new nucleation lead to the stringer-like clusters of MC particles. The grain-to-grain uniformity and spacial distribution of MC particles in a particular grain are considerably enhanced if abundant nucleation sites are available from cold deformation before aging.

After aging 10%-cold-worked PCA at 750°C for 166 h, grain boundary and matrix Laves phase appear, and the matrix dot particles coarsen, as seen in Fig. 3.3.11.

It is significant that the grain boundary phases produced in the PCA are not the same as those in either types 316 or titanium-modified 316 stainless steel. The 20%-cold-worked types 316 and titanium-modified 316 after thermal aging at 700°C for 2770 h are shown in Fig. 3.3.12. Generally, in type 316, $M_{23}C_6$, and/or eta phase precipitate particles are found at the grain boundaries.[3-5] Grain boundaries in titanium-modified type 316 contain both M23C6, in agreement with literature data (ref. 6), and Laves phase precipitate particles [see Fig. 12(b)], which have generally not been observed by others. The typical MC matrix dot denuded zone[7] is observed in titanium-modified type 316. Matrix dot precipitation of MC in the grains drastically reduces the formation of Laves and $M_{23}C_6$, and/or eta phase. The composition change of lower chromium and higher nickel in the PCA relative to type 316 appears to have retarded $M_{23}C_6$ and/or eta, thus allowing grain boundary MC to precipitate. Adamson[8] indicates that MC and $M_{23}C_6$ formation at the grain boundaries are also competing processes in niobium-stabilized Fe—20% Cr—25% Ni. The lack of grain boundary M23C6 and/or eta phase also eliminates the MC grain boundary denuded zone, and the MC precipitation is uniform up to the boundary in cold-worked PCA. The thermal aging phase stability of the PCA is superior to titanium-modified type 316 stainless steel.

With our knowledge of the thermal aging behavior of the PCA after various mechanical treatments, we can reexamine the suggested pre-irradiation microstructures in Table 3.3.1. The assumption that the PCA behaved like titanium-modified type 316 is valid for the intragranular MC precipitation response, but not for the intergranular response. Therefore, microstructure series C in Table 3.3.1 is no longer possible. Grain boundary MC always precipitates before or at the same time as matrix dot MC, so that microstructure series B is no longer possible either.

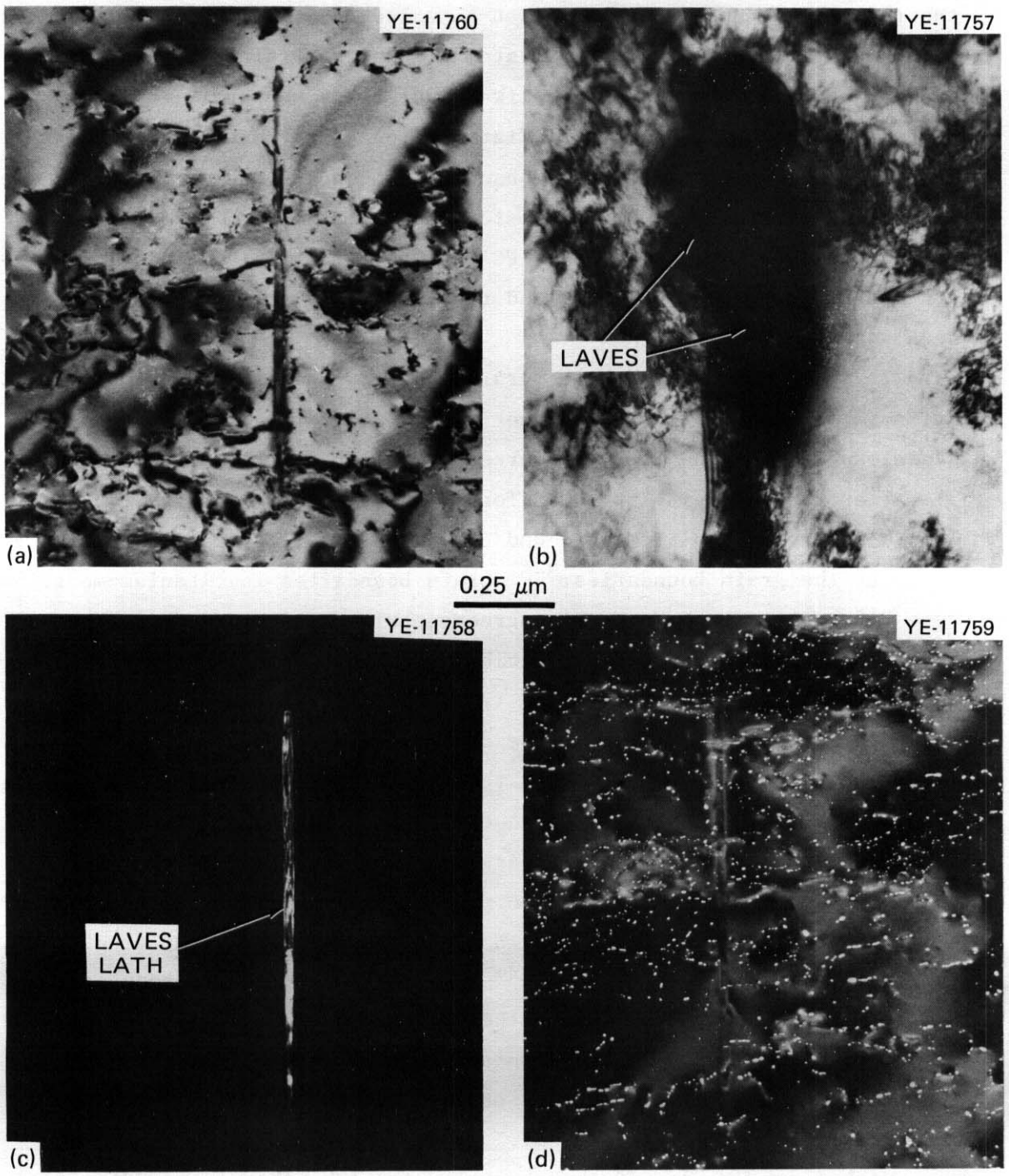

Fig. 3.3.11. The 10%-Cold-Worked Prime Candidate Alloy (PCA) Thermally Aged at 750°C for 166 h. (a) Bright field with multibeam condition near $\langle 0\bar{1}1 \rangle$. (b) Grain boundary showing Laves phase particles. (c) Dark field using (01.2) Laves reflection. (d) Dark field showing matrix dot MC with (200) MC reflection.

the particles. Upon aging solution-annealed material, dislocation generation and climb on a given slip system within the grain followed by new nucleation lead to the stringer-like clusters of MC particles. The grain-to-grain uniformity and spacial distribution of MC particles in a particular grain are considerably enhanced if abundant nucleation sites are available from cold deformation before aging.

After aging 10%-cold-worked PCA at 750°C for 166 h, grain boundary and matrix Laves phase appear, and the matrix dot particles coarsen, as seen in Fig. 3.3.11.

It is significant that the grain boundary phases produced in the PCA are not the same as those in either types 316 or titanium-modified 316 stainless steel. The 20%-cold-worked types 316 and titanium-modified 316 after thermal aging at 700°C for 2770 h are shown in Fig. 3.3.12. Generally, in type 316, $M_{23}C_6$, and/or eta phase precipitate particles are found at the grain boundaries.[3-5] Grain boundaries in titanium-modified type 316 contain both $M_{23}C_6$, in agreement with literature data (ref. 6), and Laves phase precipitate particles [see Fig. 12(b)], which have generally not been observed by others. The typical MC matrix dot denuded zone[7] is observed in titanium-modified type 316. Matrix dot precipitation of MC in the grains drastically reduces the formation of Laves and $M_{23}C_6$, and/or eta phase. The composition change of lower chromium and higher nickel in the PCA relative to type 316 appears to have retarded $M_{23}C_6$ and/or eta, thus allowing grain boundary MC to precipitate. Adamson[8] indicates that MC and $M_{23}C_6$ formation at the grain boundaries are also competing processes in niobium-stabilized Fe—20% Cr—25% Ni. The lack of grain boundary $M_{23}C_6$ and/or eta phase also eliminates the MC grain boundary denuded zone, and the MC precipitation is uniform up to the boundary in cold-worked PCA. The thermal aging phase stability of the PCA is superior to titanium-modified type 316 stainless steel.

With our knowledge of the thermal aging behavior of the PCA after various mechanical treatments, we can reexamine the suggested pre-irradiation microstructures in Table 3.3.1. The assumption that the PCA behaved like titanium-modified type 316 is valid for the intragranular MC precipitation response, but not for the intergranular response. Therefore, microstructure series C in Table 3.3.1 is no longer possible. Grain boundary MC always precipitates before or at the same time as matrix dot MC, so that microstructure series B is no longer possible either.

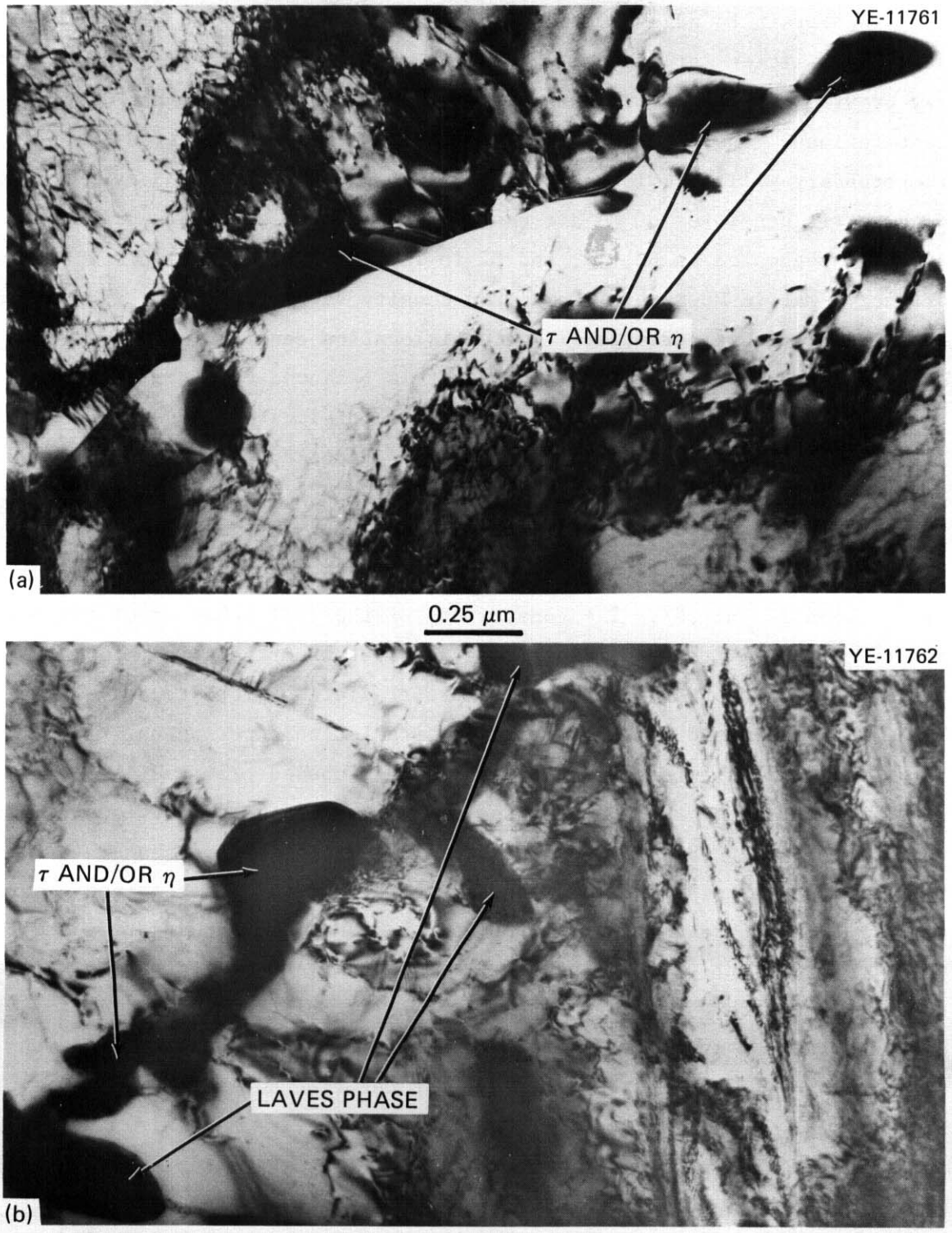

Fig. 3.3.12. Grain Boundary Precipitation after Thermal Aging at 700°C for 2770 h in (a) 20%-Cold-Worked Type 316 and (b) 20%-Cold-Worked Titanium-Modified Type 316. Note the appearance of grain boundary Laves in the titanium-modified alloy.

That grain boundary MC precipitates with such ease and variety offers new possibilities for microstructural design. It was suspected[1] that this may provide the best helium trapping for the grain boundary and its adjacent regions. The elimination of the matrix MC denuded zone adjacent to the boundary will also lessen helium reaching the grain boundary. Low and high matrix densities of MC are easy to obtain, but an intermediate density (as suggested in B2, C2, and D2 in Table 3.3.1) is more difficult to produce. Matrix MC particle size and density vary little with temperature and time but change drastically with dislocation density. Dislocation multiplication appears to saturate as it is balanced by dynamic recovery resulting from cross slip and climb, and the dislocation density increases little as plastic flow continues. This is evidenced by the similarity of matrix precipitation in 10 and 25%-cold-worked PCA material (compare Figs. 3.3.9 with 3.3.11). The optimum cold-work level resulting in the desired matrix MC density with the least impetus to recrystallize may well lie between 10 and 25%. The constraints of the real behavior of the PCA can be combined with principles from the first preirradiation microstructural design[1] to obtain a new set of preirradiation microstructures. These will be tested in future reactor irradiation experiments.

Table 3.3.3 lists our revisions of the proposed preirradiation microstructures for the PCA. Series A has been explained previously[1] and remains the same. Series B compares the effect of a large change in intragranular precipitate particle density and size for a constant, coarse distribution of grain boundary MC particles. Microstructures B2 and C compare the effect of changing the grain boundary MC precipitate particle distribution with a constant fine MC matrix dot distribution. Microstructure D evaluates the effect of increasing the dislocation density in the cell structure common to most deformed materials (see Fig. 3.3.10). Table 3.3.4 lists suggested thermal-mechanical treatments to produce the desired microstructures based upon the time-temperature-microstructural information from this work. Microstructure B1 can be visualized by combining Fig. 3.3.5(b) with Fig. 3.3.6(b). Microstructure B2 can be visualized by combining Fig. 3.3.5(b) with the matrix portion of Fig. 3.3.8. Microstructure C is shown in Fig. 3.3.8. Innovative microstructure D is shown to be possible in Fig. 3.3.13, but the time at

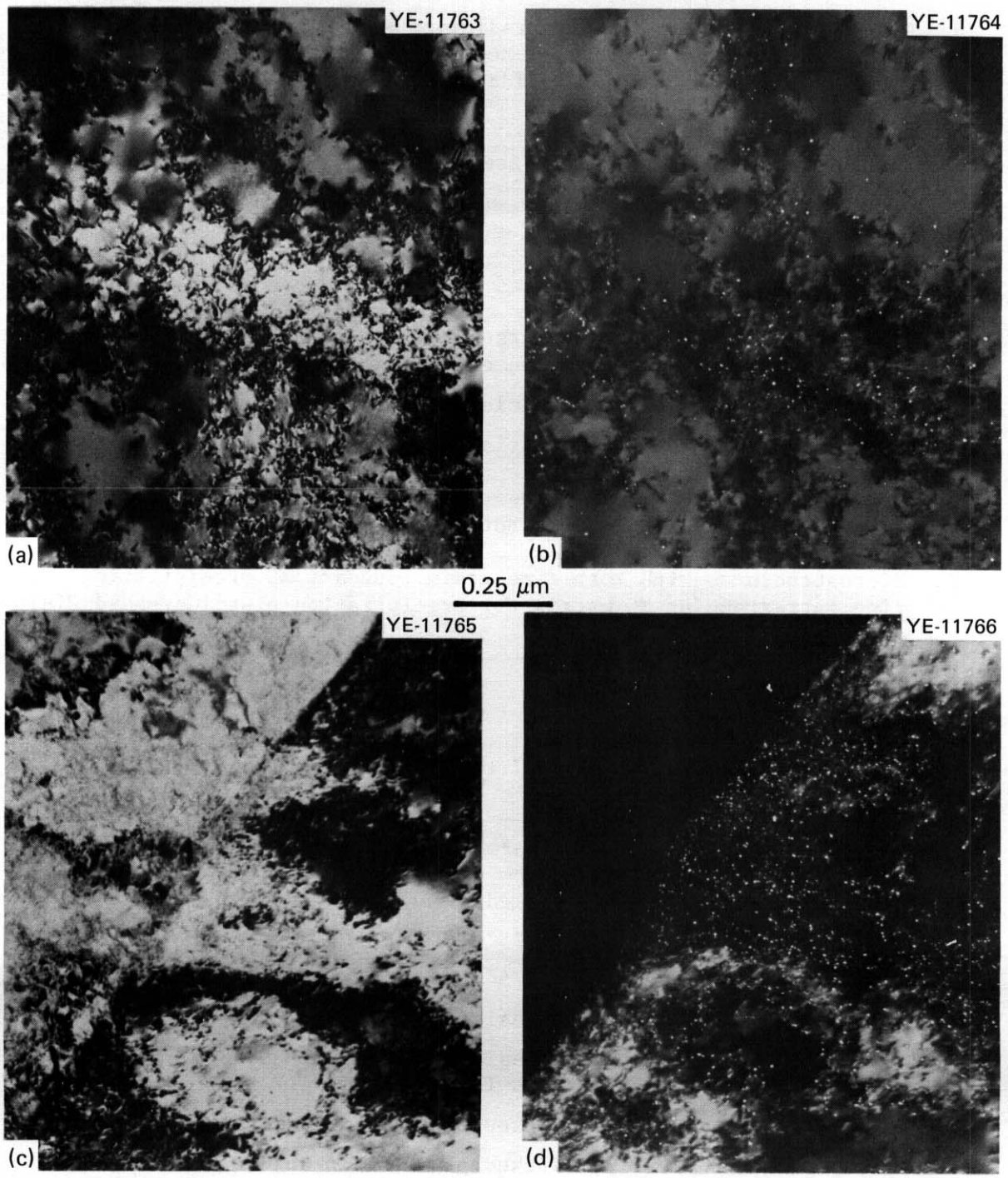

Fig. 3.3.13. The 10%-Cold-Worked Prime Candidate Alloy (PCA) Thermally Aged 15 min at 750°C and then 10% Cold Worked. (a) Bright field. (b) Dark field showing MC precipitation in the matrix. (c) and (d) bright and dark fields, respectively, showing MC precipitation at the grain boundary. Note that (a) and (b) show dislocations in the cells without precipitation, which is not observed in Fig. 3.3.10.

Table 3.3.3. Proposed Preirradiation Microstructures That can be Achieved by Thermal-Mechanical Treatment of the Prime Candidate Alloy (PCA)

A. Simple microstructures with "free" precipitation resulting from:
1. solution annealing,
2. 5 to 10% cold working, or
3. 20 to 25% cold working.
B. Microstructures with both coarse grain boundary MC precipitation and intragranular MC precipitation consisting of:
1. coarse particles or particle clusters, or
2. fine matrix dot precipitation.
C. Microstructures with both fine grain boundary MC precipitation and fine intragranular MC matrix dot precipitation.
D. Microstructures with both fine grain boundary MC precipitation and fine intragranular MC matrix dot precipitation plus increased dislocation density.

Table 3.3.4. Recommended Thermal-Mechanical Treatments to Produce Proposed Preirradiation Microstructures

Microstructure[a]	Thermal-Mechanical Treatment
A1	25% cold worked plus 15 rain at 1175°C
A2	15 min at 1175°C plus 10% cold worked
A3	15 min at 1175°C plus 25% cold worked
B1	Solution annealed plus 8 h at 800°C plus 8 h at 900°C
B2	Solution annealed plus 8 h at 800°C plus 25% cold worked plus 15 min at 750°C
C	25% cold worked plus 15 min at 750°C
D	10% cold worked plus 30 min at 750°C plus 10% cold worked

[a]Letter and number codes refer to microstructures defined in Table 3.3.3.

temperature should be increased from 15 min (as shown) to 30 min. These thermal-mechanical treatments are combined with an improved fabrication sequence[2] (see Chap. 3.2 of this report) to provide a realistic fabrication schedule in the production of specimen material (see Fig. 3.3.14). We must emphasize that achieving the required microstructures is possible only with homogeneous starting material. Recent data on titanium-modified 316 irradiated in the HFIR indicate that fine MC precipitate particles effectively trap helium at temperatures from 475 to 600°C and that precipitation of undesirable phases is also suppressed. This is illustrated in Fig. 3.3.15. No other phase behaves the way titanium-rich MC does in the austenitic stainless steels. These observations lend confidence to the performance expectations of the microstructures proposed above.

The final processing steps required to produce 0.5-mm-thick specimen material with the design microstructures are shown in Fig. 3.3.14. These fabrication sequences continue from the 0.5-mm sheet produced by the processing discussed in Chap 3.2 of this report. All the final processing steps are straightforward, and no additional discussion is required.

3.3.5 Conclusions

1. Thermal aging of the PCA both without cold working and with 10 and 25% cold working reveals that:
   a. intragranular MC precipitate particle size and spatial distribution are very sensitive functions of dislocation density, changing from coarse, clustered particles to fine matrix dot precipitate particles as the dislocation density increases;
   b. MC precipitation is considerably enhanced in both temperature and time for 10 or 25%-cold-worked PCA compared to solution-annealed material;
   c. grain boundary precipitation of MC particles always occurs before matrix precipitation in solution-annealed material but occurs nearly simultaneously in cold-worked material; and

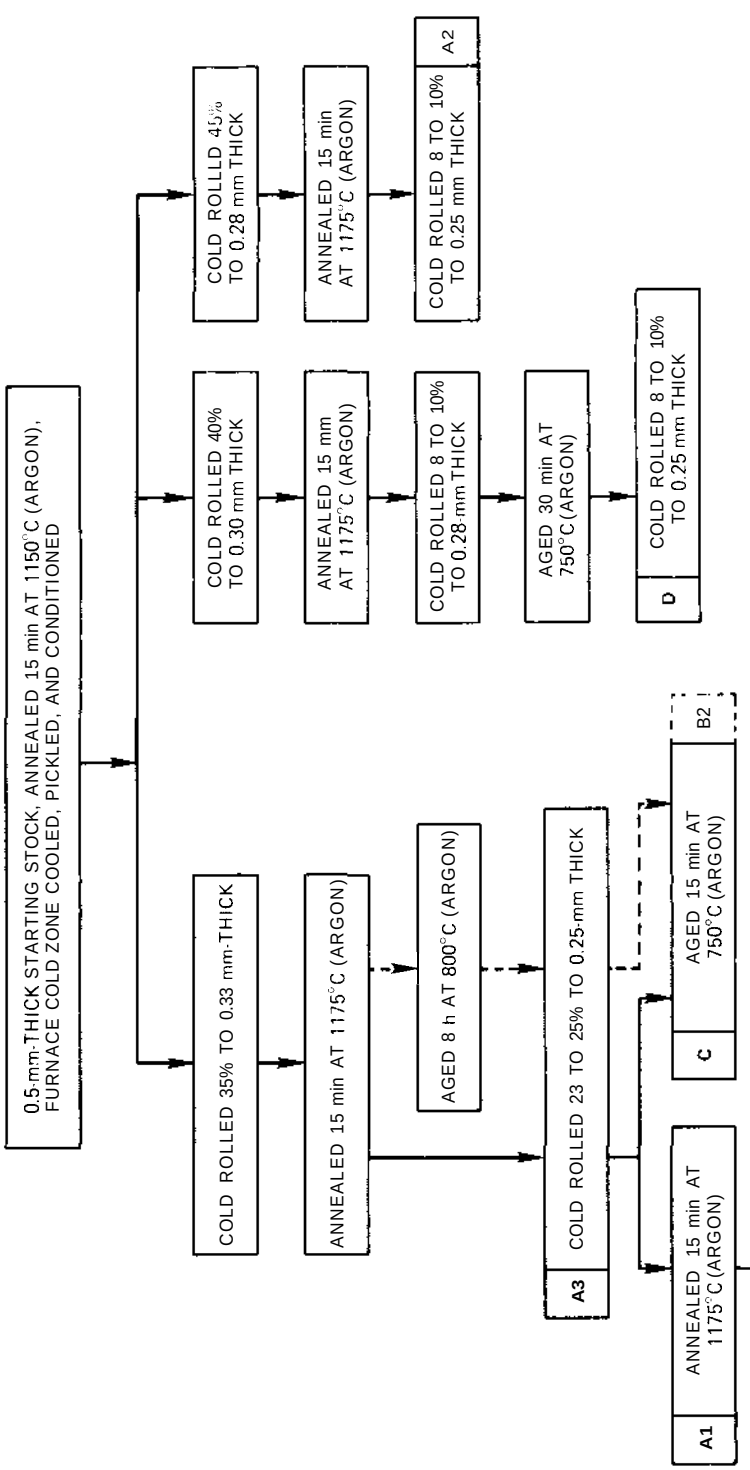

Fig. 3.3.14. Final Processing Steps to Produce Designed Microstructures of the Path A Prime Candidate Alloy (PCA). Production of the 0.5-mm starting stock is discussed in Chap. 3.2 of this report. Number and letter codes refer to the proposed preirradiation microstructures listed in Table 3.3.3.

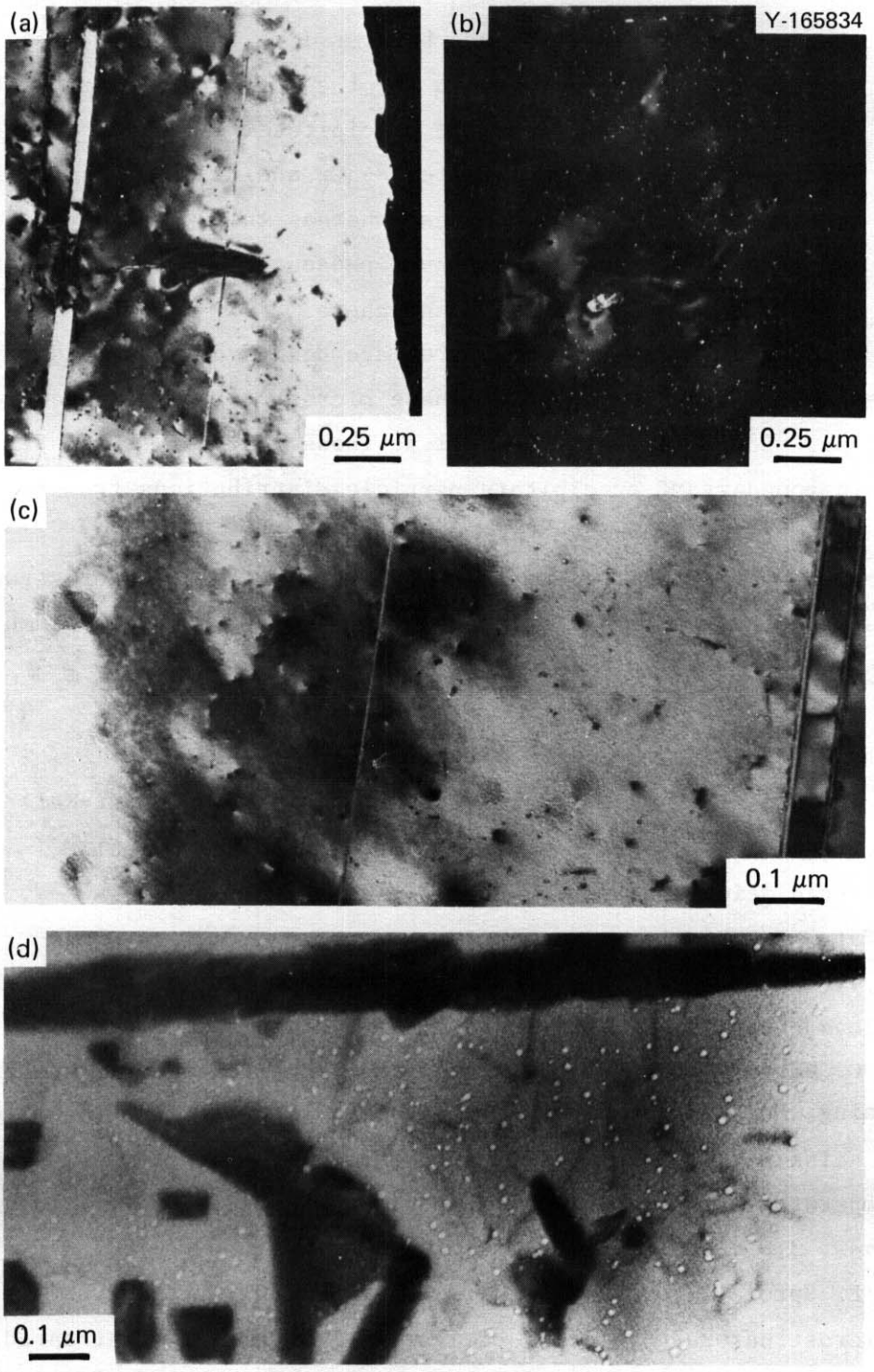

Fig. 3.3.15. Comparison of 20%-Cold-Worked Types 316 and Titanium-Modified 316 Stainless Steel After HFIR Irradiation at 475°C to a Neutron Fluence of 12.0 dpa and 540 at. ppm He. (a), (b), and (c) Titanium-modified type 316. (a) and (b) Bright and dark fields, respectively, of the titanium-rich matrix MC precipitate particles. (c) All the very small cavities are attached to the interfaces of tiny MC particles. (d) The much coarser cavity distribution and considerable precipitation of eta and Laves in type 316.

d. the assumption that the PCA behaves like titanium-modified type 316 stainless steel is valid for the intragranular but not the intergranular portion of the precipitate response. Titanium-modified type 316 precipitates $M_{23}C_6$ and/or eta phase and Laves phase at the grain boundaries, whereas the PCA precipitates MC particles with occasional Laves phase in cold-worked material after about 100 h at 700°C and above.

2. New preirradiation microstructures are designed to take advantage of the capabilities of the PCA. These microstructures include several "simple microstructures" as well as those that vary the matrix and grain boundary MC precipitate particle distributions from coarse to fine.
3. Thermal mechanical treatment to achieve the desired microstructures are given and can be incorporated into the fabrication sequence to produce specimen material.

3.3.6. References

1. P. J. Maziasz, "Microstructural Design for Fusion First-Wall Applications and Recommendations for Thermal-Mechanical Preirradiation Treatments." *ADIP Quart. Prog. Rep. June SO, 1979*, DOE/ET-0058/6, pp. 48-56.
2. D. V. Edmonds and R.W.K. Honeycombe, "Precipitation in Iron-Base Alloys," pp. 121–60 in *Precipitation Processes in Solids,* K. C. Russell and H. I. Aaronson, Eds., American Institute of Mining, Metallurgical, and Petroleum Engineers, New York, 1978.
3. B. Weiss and R. Stickler, "Phase Instabilities During High Temperature Exposure of 316 Austenitic Stainless Steel," *Metall. Trans.* 3:851-66 (1972).
4. J. E. Spruiell, J. A. Scott, C. S. Ary, and R. L. Hardin, "Microstructural Stability of Thermal-Mechanically Pretreated Type 316 Austenitic Stainless Steel." *Metall. Trans.* 4:1533–44(1973).
5. P. J. Maziasz, "The Formation of Diamond-Cubic Eta (η) Phase in Type 316 Stainless Steel Exposed to Thermal Aging or Irradiation Environments," *Scr. Metall.* 13:621–26 (1979).

6. A. S. Grot and J. E. Spruiell, "Microstructural Stability of Titanium-Modified Type 316 and Type 321 Stainless Steel," *Metall. Trans.* 6A:2023–30 (1975).

7. J. M. Silcock and A. W. Denham, "Precipitation of NaCl-Type Carbides in Austenite and Their Behaviour in the Neighborhood of Grain Boundaries," pp. 59–64 in *The Mechanism of Phase Transformations in Crystalline Solids*, Monograph and Report Series 33, The Institute of Metals, London, 1969.

8. J. M. Adamson, *The Fundamental Studies of Some Stainless Steels*, Ph.D. thesis, University of Oxford, 1972.

3.4 THE INFLUENCE OF IRRADIATION ON THE PROPERTIES OF PATH A ALLOY WELDMENTS - F. W. Wiffen (ORNL)

3.4.1 ADIP Task

ADIP Task I.B. 13, Tensile Properties of Austenitic Alloys.

3.4.2 Objective

This work will determine the response of welds and weld-affected zones to irradiation over a range of temperatures and fluences. Welds with type 316 or 16-8-2 stainless steel filler metal joining 20%-cold-worked type 316 base metal are being irradiated in the Oak Ridge Research Reactor (ORR) and High Flux Isotope Reactor (HFIR). Tensile tests to determine the effects of irradiation on the mechanical properties of the irradiated specimens will be supplemented by fractography, metallography, and microscopy.

3.4.3 Summary

Weldment samples have been irradiated in the HFIR in the temperature range 55 to 620°C to fluences producing 4.5 to 12 dpa and 100 to 410 at. ppm He in the weld metal zone. Tensile tests at temperatures near the irradiation temperatures showed appreciable strengthening up to 375°C. At 475 to 620°C the strength values were close to those of the control material. Tensile elongation showed a broad minimum in the range 300 to 400°C, with the lowest recorded total elongation of 3.5%.

3.4.4 Progress and Status

Welds have been prepared between sections of 6-mm-thick (0.25-in.) base metal plates of 20%-cold-worked type 316 stainless steel by using the gas-shielded arc welding process. Weldments discussed in this report were made with 16-8-2 filler metal. The specimens were machined from sections of material taken normal to the weld direction so that the specimen gage section contained both weldment and weld-affected material. The geometry of both the specimens used and the weld and the relationship between these are shown in Fig. 3.4.1.

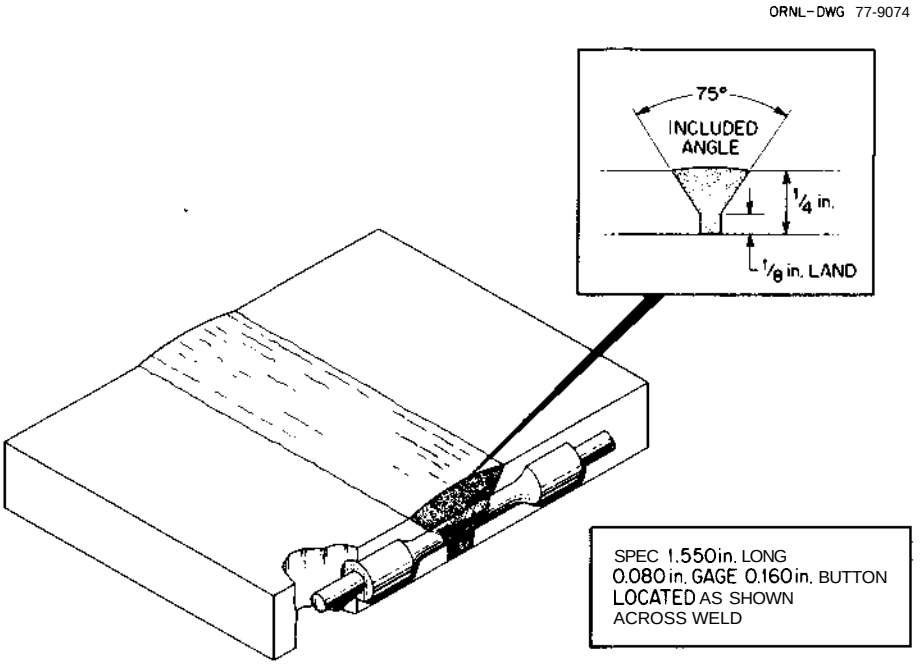

Fig. 3.4.1. Tensile Samples Showing the Location of Weld Metal in the Specimen Gage Section. The weld metal sections, located by ferrite measurement, ranged from 9.5 to 13.3 mm in a total gage length of 18.3 mm.

The weld-base metal interface in each specimen was located by finding the ferrite-containing (weldment) material with a ferrite scope. The weldment zone ranged from 9.5 to 13.3 mm long in the specimens used. This zone was centered in the 18.3-mm gage portion of the specimen.

A few of these specimens were irradiated in contact with 55°C reactor cooling water in experiment HFIR-CTR-16. Tensile and fracture properties of these specimens were reported previously,[1,2] and some results are repeated here to show the full matrix of available properties.

Specimens were irradiated above water coolant temperature in experiment HFIR-CTR-17. Temperatures are set by a helium gas gap between the specimen and specimen holder, as shown in Fig. 3.4.2.

Experiment HFIR-CTR-16 was in the reactor 9.91×10^6 s (114.66 d) at a reactor power of 100 MW; experiment HFIR-CTR-17 was in the reactor 1.184×10^7 s (137 d). The fluence on each specimen and the calculated displacement damage level and helium production that resulted are given in Table 3.4.1.

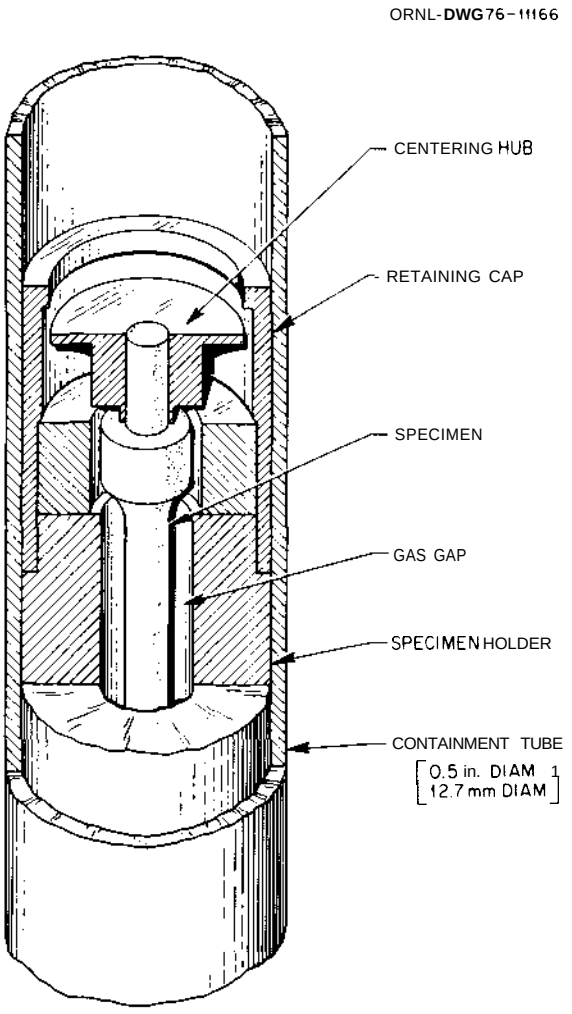

Fig. 3.4.2. The Experimental Capsule Used to Irradiate Weldment Samples in the HFIR. The irradiation temperature is determined by the width of the gas gap between the specimen and the filler piece.

Pre- and postirradiation measurements of specimen lengths indicated volume changes of less than ±0.4%. Any volume change must be a combination of microstructural changes in the 9.5 to 13.3 mm of weldment and in the remaining 19.7 to 15.9 mm of initially cold-worked type 316 base metal in the active specimen length. Uncertainty in length measurements contributes at least ±0.2% to the volume change. As a result volume changes within the weldment probably cannot be extracted from the measured length changes of less than ±0.15%. Since the base metal portion of the specimen contributes more than 80% of the total specimen volume, immersion density measurements of swelling were not attempted.

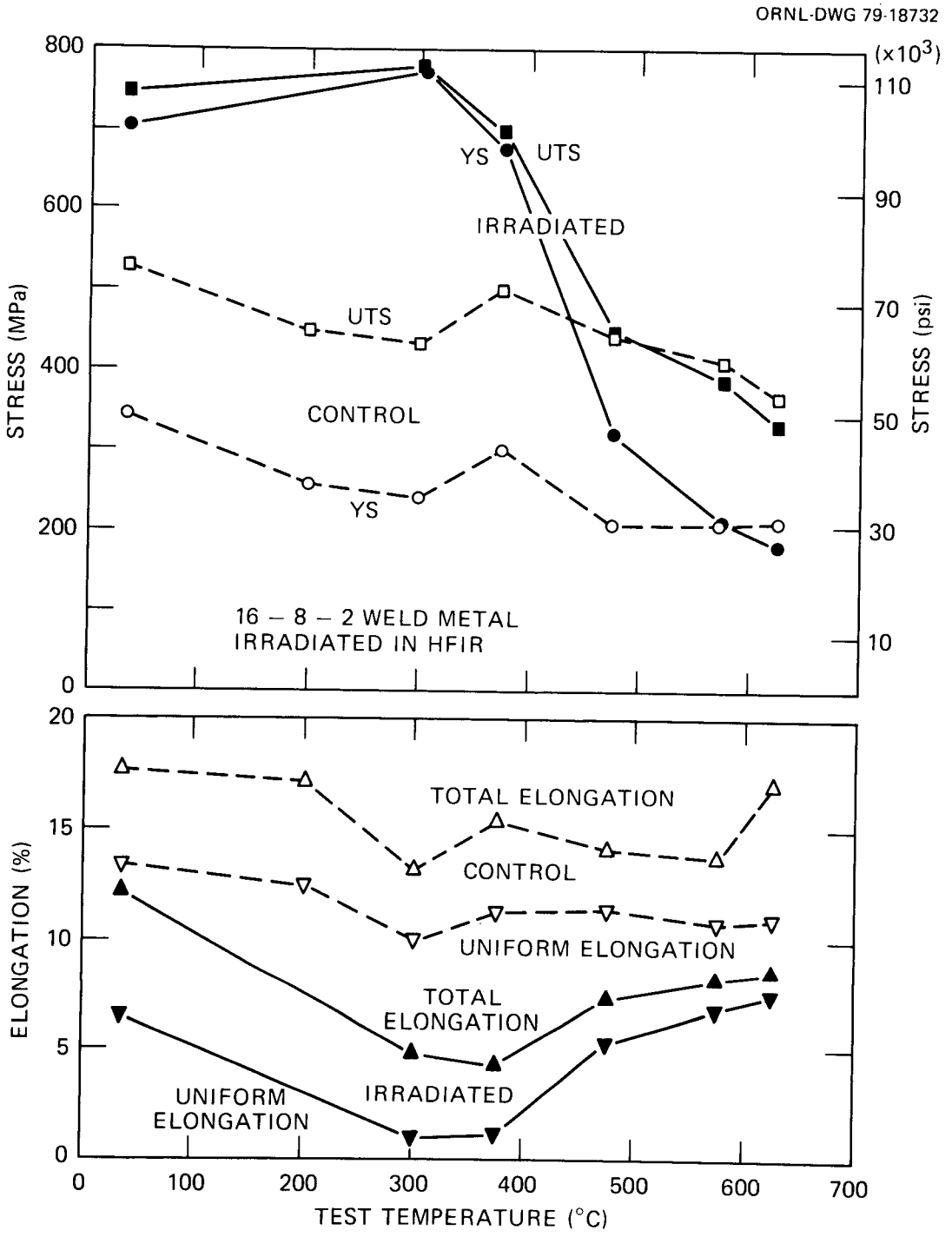

Fig. 3.4.3. Tensile Properties of 16-8-2 Weldments Irradiated in the HFIR. Specimens were irradiated at temperatures near the test temperature to fluences producing 4.5 to 11.8 dpa. Helium production resulted in 100 to 408 at. ppm in the weldments and 157 to 639 at. ppm in the type 316 base metal. The strain rate is 4.6×10^{-5}/s (0.0028/min). Average data are plotted at several temperatures (see Table 3.4.1).

Table 3.4.1. Irradiation Conditions and Tensile Properties of 16-8-2 Weldments Irradiated in the HFIR

Irradiation Conditions					Test Temperature (°C)	Tensile Properties[a]			
Temperature (°C)	Fluence (>0.1 MeV) (n/m^2)	dpa	Helium, at. ppm			Strength, MPa		Elongation, %	
			Weld Metal[b]	Base Metal[c]		0.2% Yield	Ultimate	Uniform	Total
	control				35	353	547	14.0	19.0
	control				35	333	510	12.9	16.5
	control				200	257	450	12.5	17.2
	control				300	241	433	10.0	13.3
	control				375	300	501	11.3	15.4
	control				475	209	441	11.4	14.1
	control				575	208	409	10.8	13.8
	control				625	210	367	11.1	17.1
55	0.5×10^{26}	4.5	100	157	35	680	735	6.8	12.0
55	1.09	8.7	250	390	35	701	740	5.8	11.8
55	1.35	10.8	340	532	35	727	759	7.2	13.0
284	0.87	6.5	160	251	300	771	775	1.0	4.8
371	0.88	6.6	164	257	375	740	756	1.1	4.9
374	1.32	9.8	307	481	375	633	668	1.3	3.5
374	1.30	9.7	302	473	375	654	672	1.1	4.5
466	1.11	8.2	235	368	475	369	491	4.9	6.9
473	1.59	11.8	408	639	475	293	430	6.0	7.6
473	1.59	11.8	407	637	475	307	442	5.1	7.3
557	1.10	8.2	234	366	575	215	389	6.9	8.4
564	1.48	11.0	366	573	575	205	395	6.7	8.3
564	1.47	10.9	364	570	575	201	377	6.8	7.9
620	1.63	12.1	423	662	625	183	332	7.4	8.6

[a] Strain rate = 4.6×10^{-5}/s (0.0028/min).

[b] Weldment is 8.62% Ni.

[c] Base metal is 13.5% Ni.

The irradiated tensile specimens were tested at temperatures near the irradiation temperature. Tests were conducted in air at a strain rate of 4.6×10^{-5}/s (0.0028/min).

Fracture positions were located on all specimens by measurements on post-test photomacrographs and by comparison with preirradiation ferrite zone measurements used to locate the weldments. These measurements indicated that fractures in all specimens tested near the irradiation temperature had occurred within the weldment. The minimum distance between the point of fracture and the indicated weld-base metal interface was 2 mm.

Tensile test results on control and irradiated weldments are tabulated in Table 3.4.1. The data ares also shown graphically in Fig. 3.4.3, with averages shown at temperatures where multiple tests were available. Stresses shown are engineering stresses, based on pretest specimen dimensions.

Irradiation at temperatures between 55 and 400°C has significantly strengthened the weldments. At 475°C the yield strength of irradiated specimens was greater than that of control specimens, but the ultimate tensile strength was equal for unirradiated and irradiated material. Irradiation and testing at 575 and 625°C produced strength values near but lower than the strength of unirradiated material.

As a function of irradiation and test temperature, the measured elongations exhibit a broad minimum in the range 300 to 400°C. This minimum mirrors the maximum strengthening observed at the same temperatures. Uniform elongation exceeded 1.0%, and total elongation exceeded 3.0% for all test conditions.

Fractography to determine the fracture mode has not been completed.

3.4.5 Future Work

Scanning electron microscopy and optical metallography as necessary are planned to determine the fracture mode. Other work may be initiated, pending the outcome of fractography.

3.4.6 References

1. F. W. Wiffen, D. P. Edmonds, J. F. King, and J. A. Horak, "The Influence of Irradiation on the Properties of Path A Alloy Weldments," *ADIP Quart. Prog. Rep. Mar. 31, 1978*, DOE/ET-0058/1, pp. 86–88.
2. F. W. Wiffen, D. P. Edmonds, and J. F. King, "Influence of Irradiation on the Properties of Path A Alloy Weldments," *ADIP Quart. Prog. Rep. June 30, 1978*, DOE/ET-0058/2, pp. 47-53.

4. PATH B ALLOY DEVELOPMENT - HIGHER STRENGTH Fe-Ni-Cr ALLOYS

Path B alloys are the Fe-Ni-Cr "superalloys" in which tensile, creep-rupture, and fatigue strength levels higher than attainable in the austenitic stainless steels are achieved by precipitation of one or more phases. Many alloys in this class exhibit low swelling in fast-reactor irradiations. The technology for use of Path B alloys in neutron radiation environments is not as advanced as for Path A alloys. A basis to select a specific alloy type for further development is lacking. Accordingly, the ADIP task group has selected five base research alloys that are representative of the basic systems of Path B alloys and deserve consideration for fusion reactor applications. The systems under investigation include γ' strengthened-molybdenum modified, γ' strengthened-niobium-modified, $\gamma'\gamma''$ strengthened, and a high-nickel precipitation-strengthened alloy (~75% Ni).

Near-term activities are focused on evaluating the effects of a fusion reactor neutron spectrum on key mechanical and physical properties. Damage created by the fusion reactor neutron spectrum is approximated by fission reactor irradiation. Data are presently being obtained on a limited number of commercial alloys on which scoping studies were initiated two to three years ago. The emphasis will shift to base research alloys as they become available. For those properties that are either inadequate or degraded to an unacceptable level, the influence of composition and microstructure on the response will be examined. The research program will be oriented toward determination of mechanisms responsible for the observed property changes and the effects of metallurgical variables on the response. The objective is to develop a basis for selection of the Path B prime candidate alloy(s).

5. PATH C ALLOY DEVELOPMENT - REACTIVE AND REFRACTORY ALLOYS

Two distinct and separate subgroups fall under the broad classification of Path C alloys. These subgroups are conveniently classified as "reactive metal alloys" and "refractory metal alloys." Analyses of the properties required for performance of materials in high-flux regions of fusion reactors and assessments of the known and extrapolated properties have identified titanium alloys of the reactive metal alloys and vanadium and niobium alloys of the refractory metal alloys as having the most promise for fusion reactor applications. For both the reactive and refractory alloys, there is an extreme lack of data that are relevant and necessary for selection of specific alloy types for development (i.e., solid solution, precipitation strengthened, single or multiphase). In the case of titanium alloys, the most critical deficiency is the lack of data on the response of these alloys to high-fluence neutron radiation. For vanadium and niobium alloys, while the effects of radiation on mechanical behavior are not adequately known, perhaps the most alarming deficiency is the near total lack of base-line information on the effects of cyclic (fatigue) loading on mechanical performance. Precisely because of these deficiencies in the data base and overall metallurgical experience, these alloys are still in a "scoping study" phase of their evaluation as candidates for fusion reactor first-wall materials.

The ADIP task group has selected four titanium alloys, three vanadium alloys, and two niobium alloys for the scoping phase of the development program. Titanium alloys are generally classified according to the relative amounts of a (hcp) and 3 (bcc) phases that they contain. The titanium alloys selected represent the three alloys (types a plus $, a rich, and 3 rich). Vanadium and niobium alloys are not in commercial use as are the other alloy systems in the program. Selection of the scoping alloys was based primarily on results of previous programs on vanadium cladding development for LMFBRs and high-temperature alloys for space power systems. The three vanadium alloys are V—20% Ti, V—15% Cr—5% Ti, and Vanstar 7. The binary has relatively good fabricability, and appears to be swelling resistant in fast-reactor irradiations but

is rather weak. The ternary V—15% Cr—5% Ti and precipitation-strengthened Vanstar 7 alloys are significantly stronger. The Nb—1% Zr binary alloy is included as a reference material, since a significant amount of data exists for this alloy irradiated in fast reactors. The alloy Nb—5% Mo—1% Zr is much stronger than the binary and can be developed for applications near 800°C.

Near-term activities on Path C alloys will focus on obtaining data on the unirradiated mechanical properties, corrosion, and compatibility, and the effects of irradiation on physical and mechanical properties. Fission reactor irradiation with and without helium preinjection, high-energy neutron sources, and charged-particle irradiations will be used in the development of techniques to approximate the effects of the fusion reactor neutron spectrum (He/dpa production). The objective is to develop sufficient understanding of the behavior of Path C alloy systems (Ti, V, and Nb alloys) to allow selection of Path C base research alloys. The effects of composition and microstructure on alloy performance will then be investigated in the base research alloys.

5.1 PREPARATION OF VANADIUM AND NIOBIUM PATH C SCOPING ALLOYS

R. E. Gold, R. L. Ammon, and R. W. Buckman, Jr. (Westinghouse Electric Corporation)

5.1.1 ADIP Task

I.D.1 Materials Stockpile for MFE Programs (Path C)

5.1.2 Objective

The purpose of this effort is to provide sufficient quantities of the vanadium and niobium Path C Scoping Alloys to permit initial evaluation of the potential these types of alloys might offer for fusion reactor applications. Final product forms, which are to be delivered to the Oak Ridge National Laboratory Fusion Materials Stockpile, include 2.5 mm (0.10 in.) plate, 1.5 mm (0.06 in.) and 0.76 mm (0.03 in.) sheet, and 6.4 mm (0.25 in.) diameter rod.

5.1.3 Summary

Three vanadium alloy and two niobium alloy compositions are being prepared for consumable arc melting and processing to plate, sheet, and rod for the Fusion Materials Stockpile. These are the Path C (V, Nb) Scoping Alloys selected for initial evaluations as candidate fusion reactor structural materials. All rod materials have been previously shipped to ORNL. During this reporting period, the plate and sheet materials of the niobium alloys have been prepared and are currently being readied for shipment. Final secondary processing to flat product finish sizes (2.5 mm plate and 1.5 mm and 0.76 mm sheet) is underway for the vanadium alloys. All materials associated with this contract will be shipped to ORNL by mid-October. An informal final report which provides detailed documentation of processing histories and final product chemical analyses will be prepared and forwarded to ORNL within thirty days of contract completion.

5.1.4 Progress and Status

During the current reporting period, all of the 6.4 mm (0.25 in.) diameter rod of all five alloys was delivered to the Fusion Materials Stockpile at the Oak Ridge National Laboratory. The flat products of the two niobium alloys (Nb-1Zr, Nb-5Mo-1Zr) have been produced by warm rolling the as-extruded and conditioned sheet bars to 3.75 mm (0.150 in.) plate, vacuum annealing at 1350°C for 1 hour, and cold rolling to final product forms of 2.5 mm, 1.5 mm, and 0.76 mm plate and sheet. These materials are currently undergoing nondestructive evaluation in the Quality Assurance Department of the Westinghouse Advanced Energy Systems Division. They will be ready for shipment to Oak Ridge during the first week of October.

The three vanadium alloys (V-20Ti, V-15Cr-5Ti, VANSTAR-7) have been warm rolled from the as-extruded sheet bar stage to 3.75 mm (0.150 in.) plate, and have been vacuum annealed at 1200°C for 1 hour. Final rolling of these alloys to the plate and sheet requirements of the contract will be completed during the first week of October. Following QA inspection to assure compliance with the terms of the contract, these flat products will be shipped to the Fusion Materials Stockpile; shipment is expected during the second week of October. Except for final chemical analyses on the flat products and submission of an informal final report which will document all efforts associated with this contract, shipment of the flat products will complete this procurement action.

5.2 MECHANICAL PROPERTY TESTING OF UNIRRADIATED PATH C ALLOYS — K. C. Liu (ORNL)

5.2.1 ADIP Task

ADIP Task I.B.3, Fatigue Crack Growth in Reactive and Refractory Alloys.

5.2.2 Objective

Fatigue and crack growth behavior are among the most important properties of an alloy to be used in a fusion reactor. There is essentially no information on these properties for refractory metal alloys. The objective of this work is to develop base-line information for the Path C refractory metal scoping alloys in the unirradiated condition.

5.2.3 Summary

The multipurpose system designed for testing Path C scoping alloys in high vacuum has been completed and is in operation. A series of strain-controlled fatigue tests of Nb—1% Zr has been initiated. Results of two room temperature tests in high vacuum showed that Nb—1% Zr is significantly more fatigue resistant than 20%-cold-worked type 316 stainless steel when tested in the same condition at a cyclic strain range of 0.5%.

5.2.4 Progress and Status

A vacuum system designed for use with the multipurpose material testing system was received at the end of June 1979. The testing system is now completed with capabilities of testing various types of specimens at elevated temperature in vacuum below 3 μPa.

A batch of miniature hourglass-shaped specimens, as shown in Fig. 5.2.1, was made from 6.4-mm-diam rods of Nb—1% Zr (heat 530118, not the ADIP heat). Specimens were heat treated at 1400°C for 1 h in a vacuum below 1 yPa.

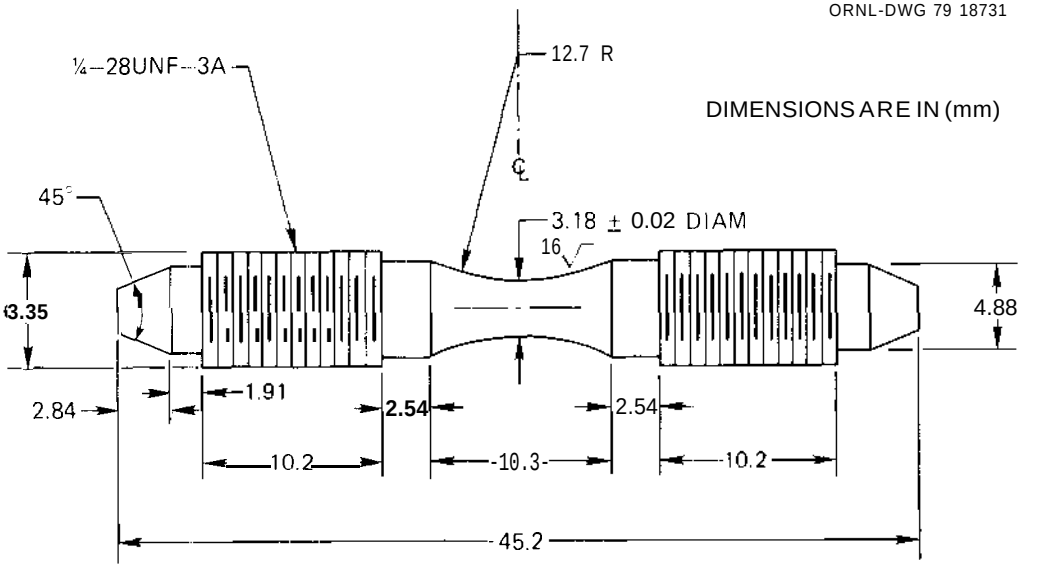

Fig. 5.2.1. Hourglass Fatigue Specimen.

Two preliminary tests were performed at room temperature in a vacuum below 0.1 mPa. These tests were fully reversed, axial strain controlled at ranges of ±0.5 and ±0.25%, respectively. Loading is controlled by an equivalent axial strain calculated from the diametral strain measured directly at the minimum gage section of the hourglass specimen. A symmetric triangular function beginning with compression was used in all the tests at a strain rate of 0.004/s.

A first test was cycled at ±0.5% strain with a specimen slightly out of tolerance. This specimen ruptured at 19,148 cycles, which falls within the scatter band of fatigue data for 20%-cold-worked type 316 stainless steel. A second test at ±0.25% strain registered 967,447 cycles at rupture. This figure is higher than the average of cyclic fatigue data of 20%-cold-worked type 316 stainless steel tested at the same strain range by a factor of 4.

Five Path C alloys from the ADIP reference heats were received as cold-worked 6.4-mm-diam rod stock. Preparation and machining of fatigue specimens are under way.

5.2.5 Conclusions

Results of a cyclic fatigue test at ±0.25% strain range indicate that Nb–1% Zr is more fatigue resistant than 20%-cold-worked type 316 stainless

steel for low strain range tests. If this alloy behaves as niobium alloy D-43[1] (Nb—9.5% W—1% Zr), an increase of fatigue life may result with increasing temperature up to about 850°C.

5.2.6 Future Work

A matrix of 12 cyclic fatigue tests of Nb—1% Zr has been initiated. Four tests are being conducted at room temperature loaded to ±1, ±0.5, ±0.25, and 0.15% strain, respectively. Similar tests are to be conducted at 550 and 650°C.

5.2.7 Reference

1. R. W. Swindeman, "Low-Cycle Fatigue Study of Columbium Alloy D-43," pp. 31—41 in *Fatigue at High Temperature*, Am. Soc. Test. Mater. Spec. Tech. Publ. 459, American Society for Testing and Materials, Philadelphia, 1969.

6. PATH D ALLOY DEVELOPMENT - INNOVATIVE MATERIAL CONCEPTS

Innovative material concepts are included as a path in the alloy development program because the fusion reactor environment is extremely demanding on materials in the high-flux region and the more conventional materials and metallurgical concepts may not be adequate. Novel approaches to alloy design, nonconventional material processing to tailor properties, or alternate materials such as structural ceramics and fiber composites will be considered.

7. STATUS OF IRRADIATION EXPERIMENTS AND MATERIALS INVENTORY

Irradiation experiments are presently being conducted in the ORR and HFIR, which are mixed-spectrum fission reactors, and in the EBR-II, which is a fast-spectrum reactor. Experiments are generally cooperative between several program participants. Experiment plans, test matrices, etc., are reviewed by the Alloy Development for Irradiation Performance Task Group.

The Office of Fusion Energy has assigned program responsibility to ORNL for the establishment and operation of a central inventory of research materials to be used in the Fusion Reactor Materials research and development programs. The objective is to provide a common supply of materials for the Fusion Reactor Materials Program.

7.1 IRRADIATION EXPERIMENT STATUS AND SCHEDULE

The following charts show the irradiation experiment schedule, including experiments completed, in progress, and planned. Experiments are presently under way in the ORR and the HFIR, which are mixed-spectrum reactors, and in the EBR-II, which is a fast reactor.

Specimens from EBR-II subassembly X287 are being sorted and shipped to participating laboratories. Pin B284 of subassembly X217D will be removed from the EBR-II in October.

ORR-MFE-2 and HFIR-CTR-26 and -27 are in the ORR and HFIR, respectively, and are performing satisfactorily. The design has been completed for HFIR-CTR-28 and -29, and these experiments are being fabricated.

The designs of the specimen racks and loading device for ORR-MFE-4 have been completed. The capsule parts are now being machined.

Experiment Designation	Objective
A. Oak Ridge Research Reactor	
ORR-MFE-1, ORR-MFE-2	Experiments to scope the effects of composition and microstructure on the tensile, fatigue, and irradiation creep of representative path A, B, and C alloys.
ORR MFE 3	Effects of irradiation on postirradiation fatigue crack growth in representative path A, B, and C alloys.
ORR-MFE-4	Effect of irradiation on tensile, fatigue, and irradiation creep of path A PCA (Prime Candidate Alloy) and path B base research alloys. Spectral tailoring to maintain correct He/dpa ratio. Irradiation on continuing basis.

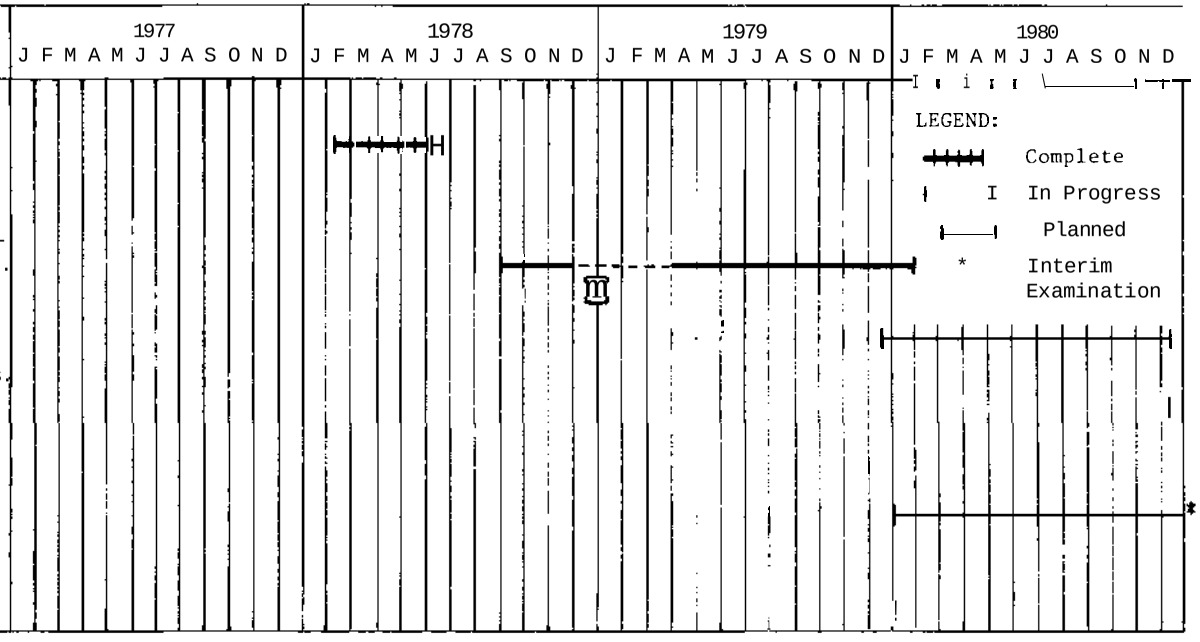

[1] MFE-2 was removed from the ORR on Nov. 29, 1978, to repair a small helium leak in the experiment containment. It is anticipated that the experiment will be reinstalled in the reactor during the latter part of April 1979. While the experiment was out of the reactor a dosimetry experiment was performed with core configuration as with MFE-2.

Experiment Designation	Objective
ORR-MFE-5	In-reactor fatigue crack growth experiment
B. Experimental Breeder Reactor II	
Subassembly X 264	Effect of preinjected helium (2—200 at. ppm) on microstructure and tensile properties of 316 SS, PE-16, V and Nb alloys. Fluence ≤2.3 × 10^{26} n/m^2, 500—825°C.
Subassembly X 287	Effect of preinjected helium (2—200 at. ppm He) on microstructure and tensile properties of 316 SS, PE-16, V and Nb alloys. Fluence ≤4 × 10^{26} n/m^2, 400—700°C.
Subassembly X 217D	Stress relaxation Ti alloys
See footnotes [1] [2] and [3]	Effect of irradiation on swelling, tensile, fatigue, and crack growth properties of Ti scoping alloys. 370, 450, and 550°C, fluence 4.5—5.5 × 10^{26} n/m^2.

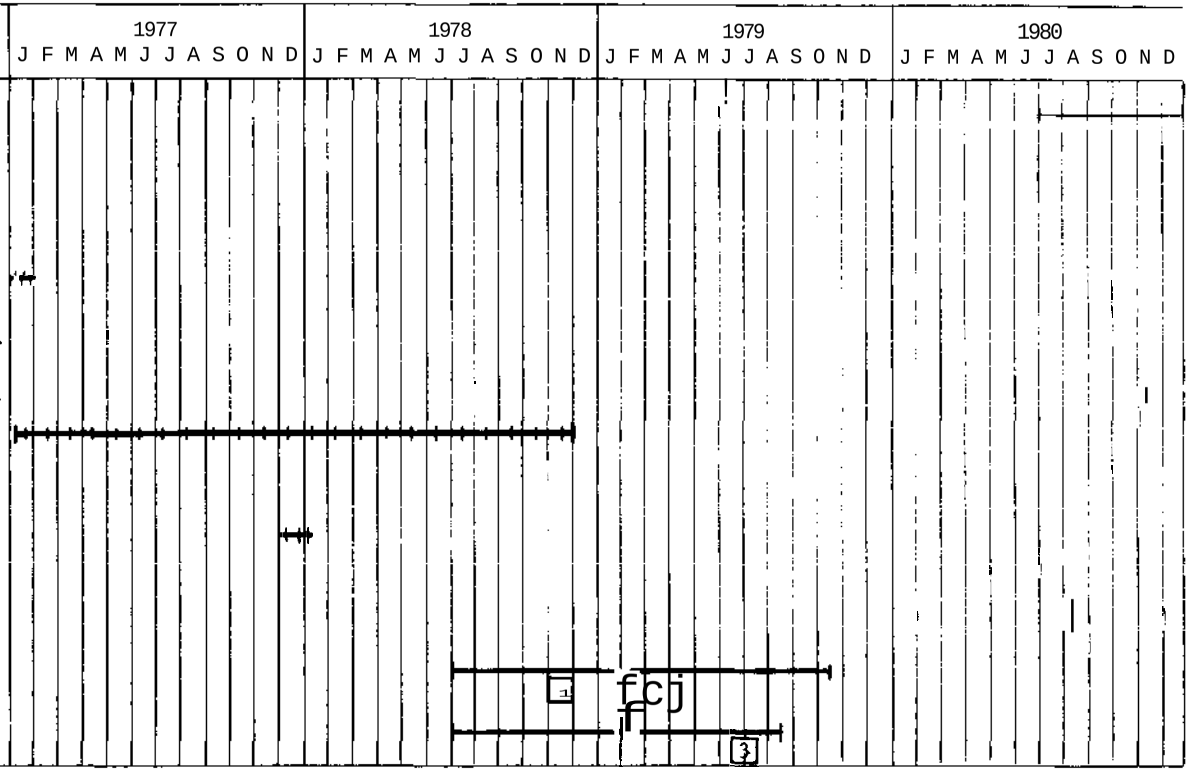

[1] EBR-II, row 2, pins B285 and B286.

[2] Subassembly removed for EBR-II run 99.

[3] Pin B284, row 2 for runs 96—98; row 4 for runs 100—102.

Experiment Designation	r Objective
Experiment plan depends on alloy availability. EBR-II space not yet identified.	Effect of Irradiation on swelling, tensile, fatigue, and crack growth properties of V and Nb scoping alloys. 370, 450, 550, and 650°C. Position in reactor not finalized, therefore no fluence estimate.
C. High Flux Isotope Reactor (HFIR)	
HFIR-CTR-4	PE-16 for swelling and tensile properties, 300–700°C 2.2–4.5 dpa, 100–350 at. ppm He
HFIR-CTR-7	PE-16 for swelling and tensile properties, 300–700°C ~9–18 dpa, 1250–3000 at. ppm He
HFIR-CTR-o ft	duplicate of -4
HFIR-CTR-9	316 and 316 + Ti for swelling and tensile properties, 280–680°C, 9–18 dpa, 400–1000 at. ppm He

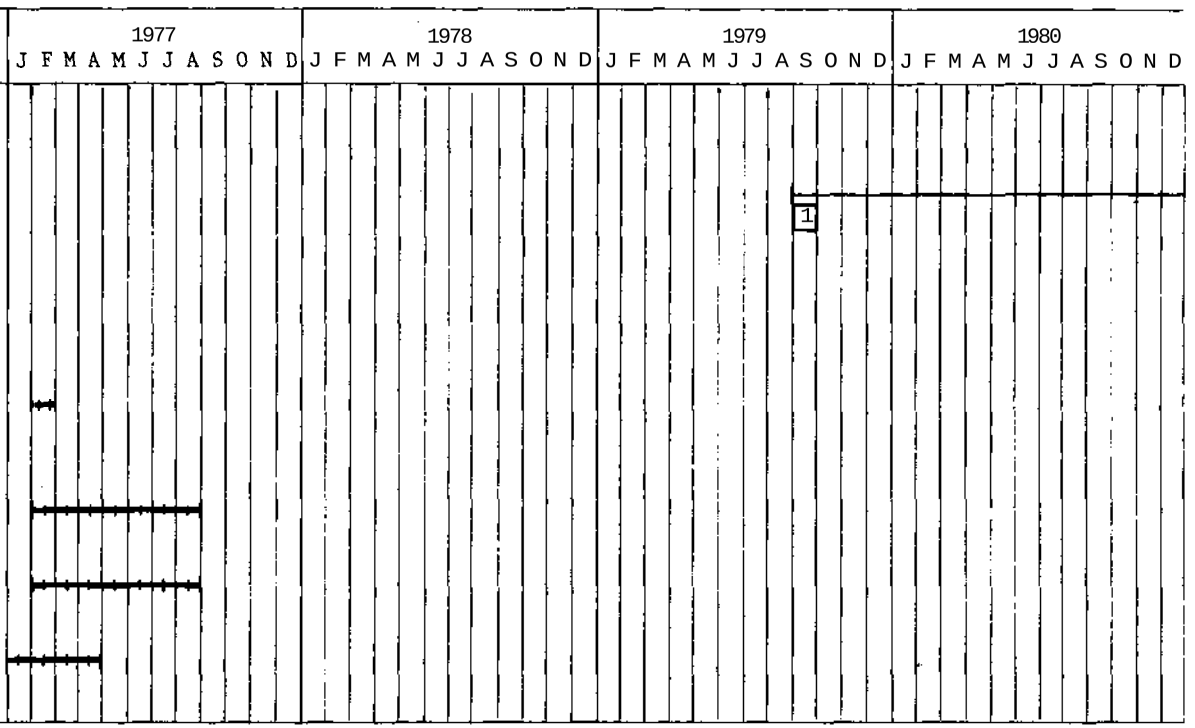

[1] Earliest date irradiations can begin on present alloy development schedule.

Experiment Designation	Objective
HFIR CTR-10	
HFIR CTR-11	duplicate of -9
HFIR-CTR-12	316 and 316 + Ti for swelling and tensile properties, 280—680°C, 5.5—11 dpa, 200—500 at. ppm He
HF1R-CTR-13	duplicate of -12
HFIR-CTR-14	20%-CW 316 for fatigue testing 300°C. 9 — 18 dpa, 400—1000 at. ppm He
HFIR-CTR-15	20%-CW 316 for fatigue testing 500°C, 5.5—11 dpa, 200—500 at. ppm He
HFIR-CTR-16	316, welds, PE-16, and Inconel 600 for swelling and tensile properties, ~55°C, 5.5—11 dpa, 150—2700 at. ppm He (depending on alloy)
HFIR CTR 17	Type 316 welded with 16-8-2 filler metal for tensile properties and failure analysis, 280—620°C, 6.7-13 dpa, 180—460 at. ppm He in weld metal

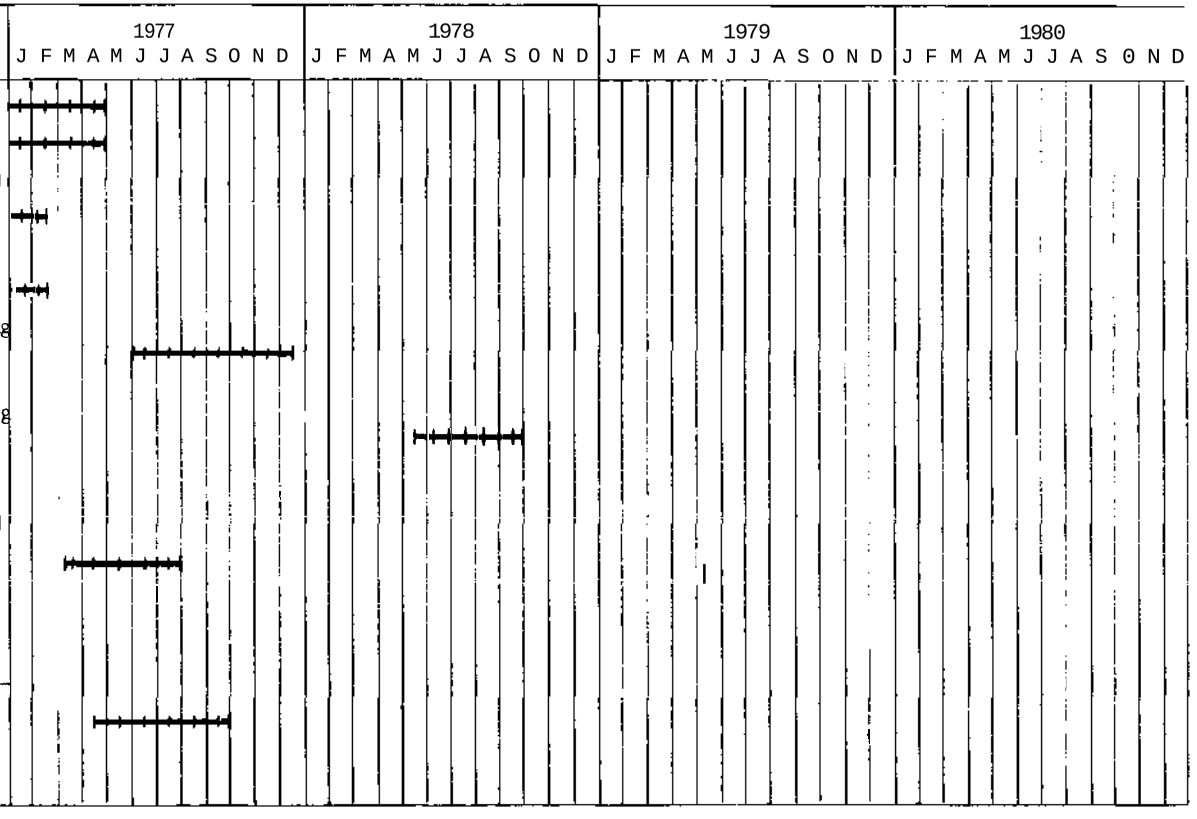

Experiment Designation	Objective
HFIR CTR-18	PE-16 and 20%-CW type 316 for swelling and tensile properties, 280–700°C, PE 16: 17 27 dpa, 3400–5600 at. ppm He 316: 27-34 dpa, 1600–2100 at. ppm He
HFIR-CTR-19	316 welded with 316 filler metal for tensile properties, 280–620°C, 5.5–11dpa, 200–500 at. ppm He
HFIR-CTR-20	20%-CW 316 for fatigue testing, 300°C, 5.5–11 dpa, 200–500 at. ppm He
HFIR CTR-21	20%-CW 316 for fatigue testing, 300–700°C, 4.4–9 dpa, 400–1000 at. ppm He
HFIR CTR 22	duplicate of 20
HFIR-CTR-23	PE-16 for fatigue testing, 300°C, 4.4–9 dpa, 370–1000 at. ppm He

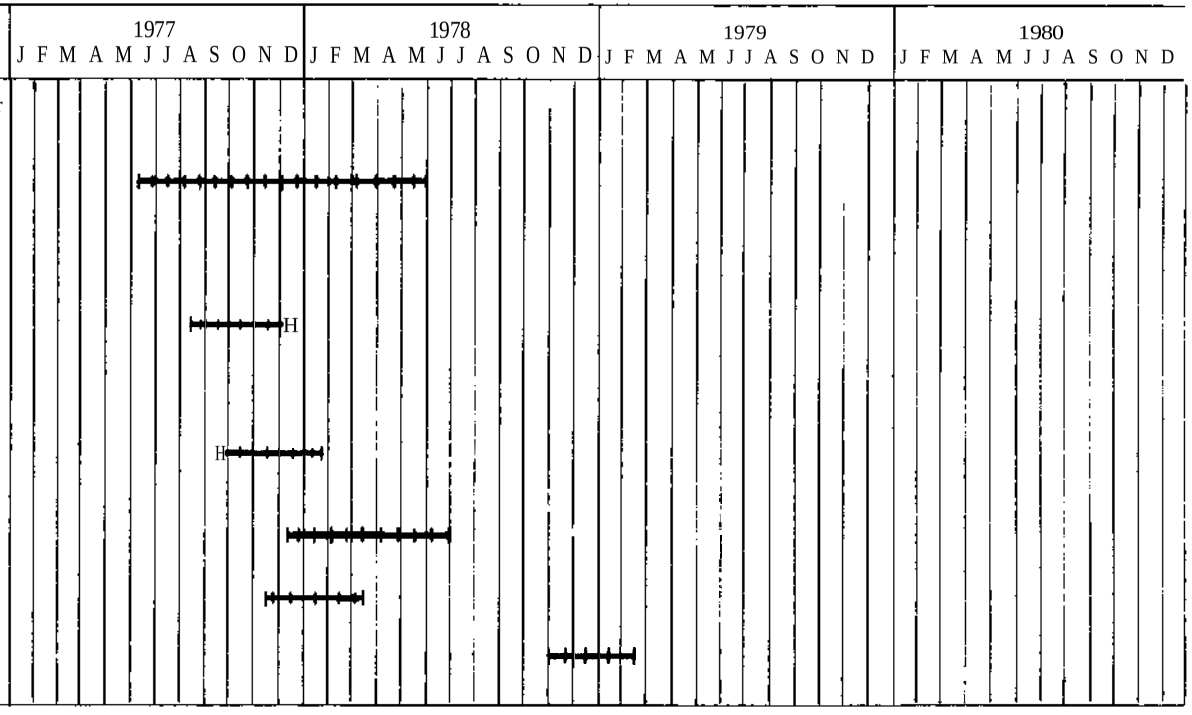

Experiment Designation	Major Objective
HFIR-CTR-24	Temperature calibration, tensile properties of MFE ref. 316, 2.25 dpa, 30 at. ppm He
HFIR-CTR-25	Temperature calibration, tensile properties of MFE ref. 316, 2.25 dpa, 30 at. ppm He
HFIR-CTR-26	Swelling and tensile properties of MFE ref. 316, 32 dpa, 1900 at. ppm He
HFIR-CTR-27	Swelling and tensile properties of MFE ref. 316, 56 dpa, 3450 at. ppm He
HFIR-CTR-28	Swelling and tensile properties of MFE ref. 316, 32 dpa, 1900 at. ppm He
HFIR-CTR-29	Swelling and tensile properties of MFE ref. 316, 56 dpa, 3450 at. ppm He
HFIR-CTR-30	Swelling and tensile properties, Paths A, B, and D microstructural variations, 40 dpa, 2500 at. ppm He (Path A)
HFIR-CTR-31	Swelling and tensile properties, Paths A, B and D microstructural variations, 20 dpa, 1200 ppm He (Path A)
HFIR-CTR-32	Swelling and tensile properties, Paths A, B and D microstructural variations, 10 dpa, 500 ppm He (Path A)

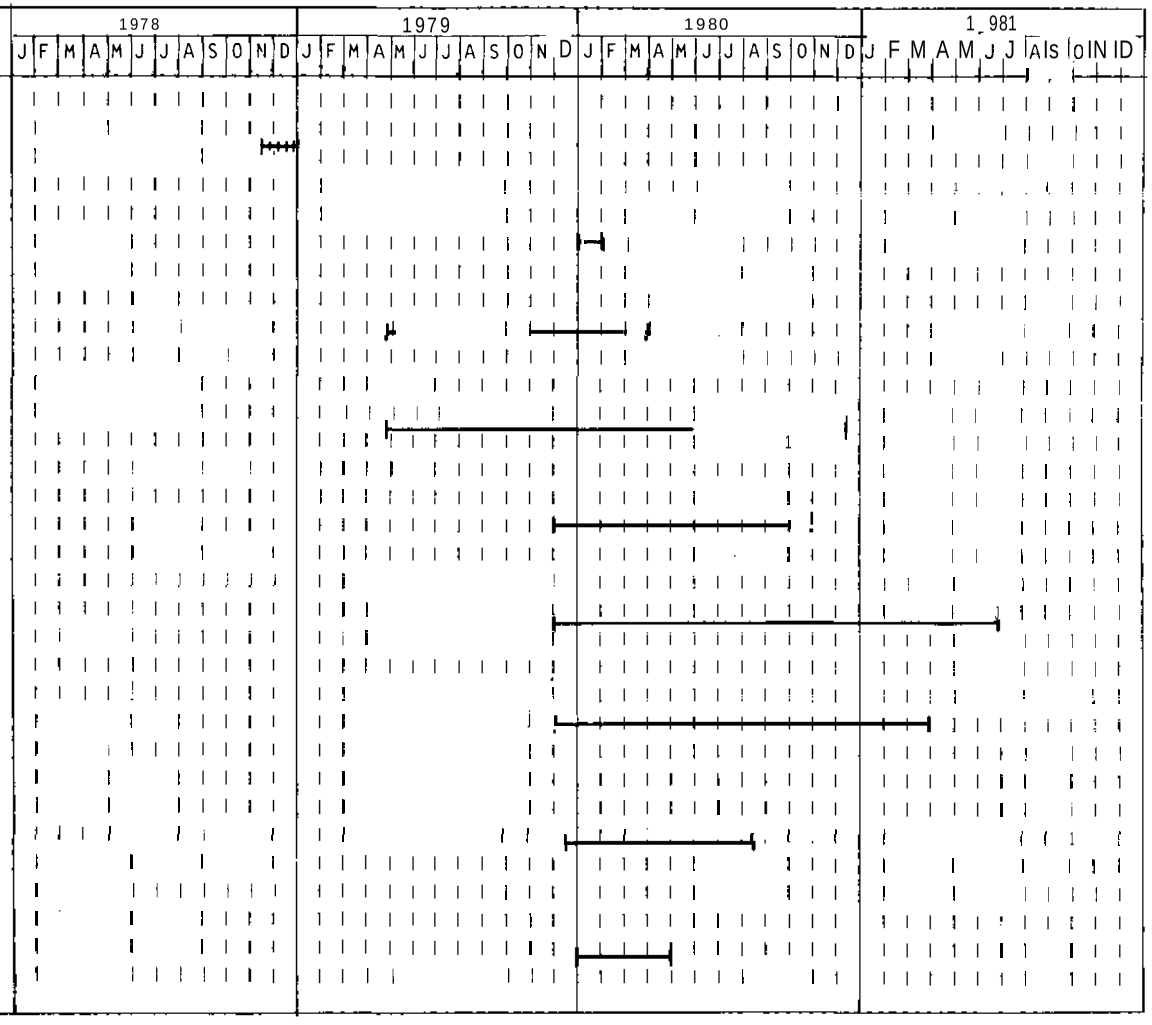

7.2 ETM RESEARCH MATERIALS INVENTORY — F. W. Wiffen, T. K. Roche (ORNL) and J. W. Davis (McDonnell Douglas)

7.2.1 ADIP Task

ADIP Task I.D.I, Materials Stockpile for MFE Programs.

7.2.2 Purpose and Scope

The Office of Fusion Energy has assigned program responsibility to ORNL for the establishment and operation of a central inventory of research materials to be used in the Fusion Reactor Materials research and development programs. The objective is to provide a common supply of materials for the Fusion Reactor Materials Program. This will minimize unintended materials variables and provide for economy in procurement and for centralized recordkeeping. Initially this inventory is to focus on materials related to first-wall and structural applications and related research, but various special purpose materials may be added in the future.

The use of materials from this inventory for research that is coordinated with or otherwise related technically to the Fusion Reactor Materials Program of DOE, but which is not an integral or directly funded part of it, is encouraged.

7.2.3 Materials Requests and Release

Materials requests shall be directed to ETM Research Materials Inventory at ORNL (Attention: F. W. Wiffen). Materials will be released directly if:

(a) The material is to be used for programs funded by the Office of Fusion Energy, with goals consistent with the approved Materials Program Plans of the Materials and Radiation Effects Branch.

(b) The requested amount of material is available, without compromising other intended uses.

Materials requests that do not satisfy both (a) and (b) will be discussed with the staff of the Materials and Radiation Effects Branch, Office of Fusion Energy, for agreement on action.

7.2.4 Records

Chemistry and materials preparation records are maintained for all inventory material. All materials supplied to program uses will be accompanied by summary characterization information.

7.2.5 Summary of Current Inventory (Sept. 30, 1979)

7.2.5.1 Path A Alloys

1. Reference alloy — type 316 stainless steel. Bar, plate, rod, and 0.180-in.-diam tubing are in stock. Rework will be scheduled as required.
2. Prime Candidate Alloy (PCA) (Fe—16 Ni—14 Cr—2 Mo—Mn, Ti, Si, C) was produced by Teledyne Allvac. Table 7.2.1 lists the product forms in stock.
3. PCA Tube production and remelt for composition variation is planned for FY 1980.

7.2.5.2 Path B Alloys

4. A reference heat of PE-16 is in stock at ORNL. Plate, rod, and 0.180-in.-diam tubing are available.
5. Base Research Alloys

Alloy	Ni	Cr	Mo	Nb	Ti	Al	Si
B-1	25	10	1		3	1.5	0.3
B-2	40	12	3		1.5	1.5	0.3
B-3	30	12		2	2	0.5	0.3
B-4	40	12		3	1.8	0.3	0.3
B-6	75	15		1	2.5	1.5	0.3

Two 140-kg heats of each alloy from Teledyne Allvac are in stock. A single sheet bar and a rod have been extruded from each of the five alloys, and the material is being used to produce final product form.

Table 7.2.1 lists the available primary product forms of the five alloys.

Table 7.2.1. *Path* A and B Developmental Alloys in the ETM Research Materials Inventory[a]

Alloy	Heat	Product Form[b]	Dimensions		Quantity				
			(ram)	(in.)	(kg)	(lb)	(m)	(ft)	(pieces)
Path A PCA	K-280	RCS bar	130	5					1[c]
		Round bar	100	4	417	920			
		Round bar	33	1 5/16	74	164	11	35	
		Round bar	12.06	0.475	63	138	69	227	
		Plate	13 x 130	1/2 x 5	70	154	4.6	15	
Path B BRA									
B-1	J-270	RCS bar	100	4	93	204			2
	J-271	RCS bar	100	4	91	200			2
B-2	J-268	RCS bar	100	4	98	217			2
	J-269	RCS bar	100	4	99	219			2
B-3	J-266	RCS bar	100	4	92	202			2
	J-267	RCS bar	100	4	93	204			2
B-4	J-264	RCS bar	100	4	92	202			2
	J-265	RCS bar	100	4	93	204			2
B-6	J-262	RCS bar	100	4	89	197			2
	J-263	RCS bar	100	4	83	184			2

[a] All from vendor Teledyne Allvac.

[b] RCS = round-corner square.

[c] One 13-mm (1/2-in.) slice from bar.

7.2.5.3 Path C Alloys (Refractory Alloys)

6. Small amounts of several niobium- and vanadium-base alloys are currently available at ORNL. Quantity and product forms are limited.

7. An order has been placed for the purchase of approximately 6 kg each of five alloys. Only sheet and rod will be produced.

   Alloys: Nb—1% Zr
   Nb—5% Mo—1% Zr
   V—20% Ti
   V—15% Cr—5% Ti
   V—9% Cr—3.3% Fe—1.3% Zr—0.05% C (Vanstar 7)

   Partial delivery has been made. Table 7.2.2 lists the material currently available. Sheet of each alloy will soon be available.

7.2.5.4 Path C Alloys (Reactive Alloys)

8. The titanium-base scoping alloys have the following compositions, wt%:

Alloy	Al	V	Mo	Zr	Sn	Cr	Si
Ti-64	6	4					
Ti-6242S	6		2	4	2		0.09
Ti-5621S	5		1	2	6		0.25
Ti-38644	3	8	4	4		6	

   At least 0.75 m^2 (1200 $in.^2$) of each of these alloys is currently available in 0.76-mm (0.030-in.) thickness. This sheet is from the same heat as material currently in reactor experiments. Larger section sheet of alloy Ti-5621S is also available.

   Orders are now being developed to purchase new stocks of these alloys in several product forms. Delivery dates have not yet been determined.

   The titanium-base alloys are stored at McDonnell Douglas. However, inventory control and materials release are handled by ORNL, and requests should be addressed to ORNL.

Table 7.2.2. Path C Scoping Alloys (Refractory Metals[a]) in the ETM Research Materials Inventory

Alloy	Heat	Quantity	
		(m)	(ft)
V—20% Ti	CAM-832 Top	9.3	30.6
V—15% Cr—5% Ti	CAM-835 Bottom	7.9	25.8
Vanstar 7[b]	CAM-836 Top	7.6	24.8
Nb—1% Zr	CAM-839 Bottom	8.0	26.2
Nb—5% Mo—1% Zr	CAM-841 Bottom	8.1	26.7

[a]All 6.35-mm-diam (0.250-in.) rod received from vendor, Westinghouse Electric Company, during current reporting period.

[b]Nominal composition V—9% Cr—3.3% Fe—1.3% Zr—0.05% C.

8. CORROSION TESTING AND HYDROGEN PERMEATION STUDIES

Corrosion, erosion, and mass transfer are processes that may degrade mechanical properties, alter heat transfer characteristics of heat transport systems, and present maintenance problems when radioactive nuclides are involved. The importance of hydrogen permeation and the behavior of hydrogen in the alloy systems under development is clear from consideration of tritium inventory, containment, etc. In the early stages of the development program, base-line information is required to define compatible or noncompatible alloy systems and coolants. As optimized alloys are developed, more detailed data on effects of adjustments in alloy composition or structure may be required. Extensive engineering compatibility data will be required on the final optimized alloys.

8.1 THE COMPATIBILITY OF TYPE 316 STAINLESS STEEL WITH NITROGEN-CONTAMINATED STATIC LITHIUM - P. F. Tortorelli and J. H. DeVan (ORNL)

8.1.1 ADIP Task

ADIP Task I.A.3, Perform Chemical and Metallurgical Compatibility Analyses.

8.1.2 Objective

The purpose of this program is to determine the chemical compatibility of fusion reactor candidate materials with metallic lithium. Specimens are exposed to static lithium-containing selected solute additions to identify the kinetics and mechanisms that govern corrosion by lithium. Specific program objectives are: (1) to determine the effects of N, C, H, and 0 on apparent solubilities in Li, (2) to determine the C and N partitioning coefficients between alloys and Li, (3) to determine the effects of soluble (Ca, Al) and solid (Y, Zr, Ti) active metal additions on corrosion by Li, and (4) to determine the tendencies for mass transfer between unlike solid metals in lithium.

8.1.3 Summary

Data on the weight loss and grain boundary penetration of type 316 stainless steel exposed to lithium with varying concentrations of nitrogen are presented. We observed no penetration at 600 and 700°C for nitrogen concentrations below 3000 ppm.

8.1.3 Progress and Status

Previous work[1] has shown that 2 wt % N in static lithium at 500 to 700°C resulted in severe corrosion of type 316 stainless steel relative to tests in as-purified lithium. At 500°C we observed a very porous near-surface layer, while at 600 and 700°C grain boundary penetration dominated. Other workers[2] empirically found that below 727°C the depth of penetration along grain boundaries of type 304L stainless steel could be described by

$$X = [4000N \exp(-15{,}600/T)t]^{1/2} , \quad (1)$$

where

X = average penetration depth, mm;

t = exposure time, h;

T = absolute temperature;

N = concentration of nitrogen in lithium (constant throughout exposure).

Since our experiments were conducted in sealed capsules (see ref. 3 for the experimental details), the nitrogen concentration of the lithium decreased with time as it reacted with the stainless steel. It can be approximated by[4]

$$N = A_0 \exp(-at) \quad , \tag{2}$$

where A_0 is related to the initial concentration of nitrogen in the lithium and to the geometry of the system, and a is proportional to the diffusion coefficient of nitrogen in stainless steel. We thus modified Eq. (1) to account for the time dependence of N:[4]

$$X = [4000A_0 \exp(-15{,}600/T) \exp(-at)t]^{1/2} \quad . \tag{3}$$

When compared to the previous data, Eq. (3) satisfactorily predicted the time dependence of the penetration of type 316 stainless steel exposed to Li— 2 wt % N (ref. 4), but yielded values of the penetration depth that were greater than the measurements by factors of 6 to 10. Subsequently, we performed more experiments with type 316 stainless steel and varied the nitrogen concentration of the lithium. The weight changes and metallographic results are given in Table 8.1.1, which also includes the appropriate data from our earlier tests in Li— 2 wt % N (ref. 4). Figure 8.1.1 illustrates the grain boundary penetration at 600 and 700°C as a function of the nitrogen concentration of the lithium.

Table 8.1.1. Weight Changes and Metallographic Results from Tests of Type 316 Stainless Steel in Nitrogen-Contaminated Lithium for 100 h

N in Li (wt %)	Temperature (°C)	Weight Change (g/m^2)	Metallographic Results
0.08	500	+0.1	No attack
0.08	600	0.0	No attack
0.08	700	0.0	Slight surface roughening
0.16	500	0.0	
0.15	600	0.1	
0.16	700	0.0	Slight surface roughening
0.23	500	+0.1	
0.24	600	—0.1	
0.24	700	0.0	Slight surface roughening
0.31	500	—0.3	Slight surface roughening
0.31	600	—0.4	Surface roughening
0.33	700	+0.1	Surface roughening
0.62	500	—7.8	
0.63	600	—0.3	gb[a] attack to 5 ym
0.59	700	—0.8	gb attack to 17 ym
0.93	500	0.0	
0.94	600	—0.4	
0.87	700	-2.5	gb attack to 30 ym
1.24	500	+0.1	
1.25	600	-2.7	
1.26	700	—4.1	gb attack to 39 ym
1.47	500	-33.6	Porous layer to 21 ym
1.54	600	—6.2	gb attack to 9 ym
1.55	700	—5.5	gb attack to 32 ym
2.00	500	—17.2[b]	Porous layer to 11 μm[c]
2.00	600	—15.1[b]	gb attack to 13 μm[c]
2.00	700	—22.4[b]	gb attack to 41 μm[c]

[a] gb = grain boundary.

[b] Average of four measurements.

[c] Average of three measurements.

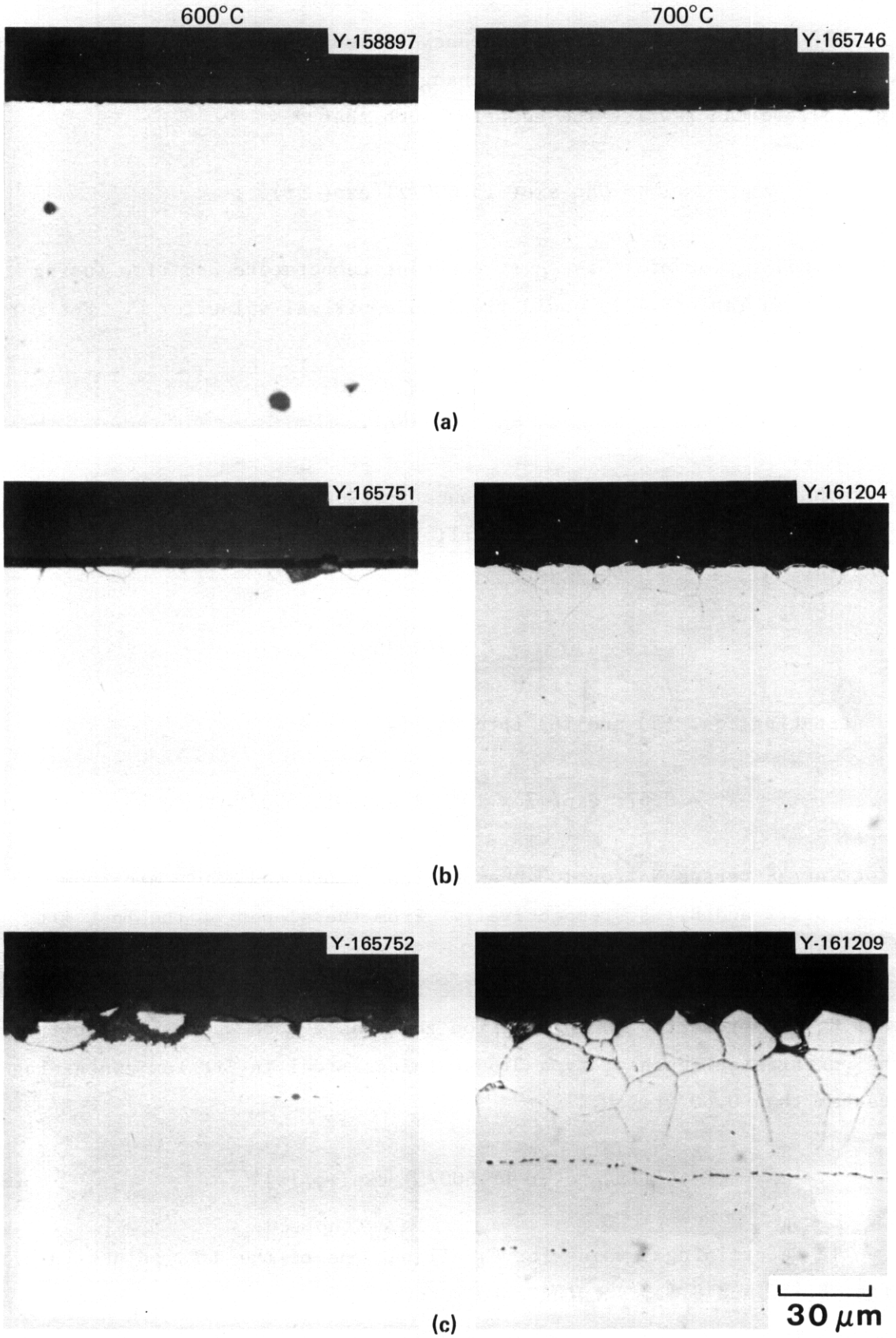

Fig. 8.1.1. Type 316 Stainless Steel Exposed to Nitrogen-Contaminated Lithium. (a) Initial concentration of 0.08 wt % N, (b) 0.6 wt % N, and (c) 1.5 wt % N.

If we assume that the discrepancy between the calculated and measured values of X can be diminished by changing the preexponential factor in Eq. (3), we can rewrite the equation such that

$$X^2 = CA_0 \exp(-15{,}600/T) \exp(-at)t \quad . \tag{4}$$

Therefore, a plot of X^2 vs A_0 at constant temperature and time (using the data in Table 8.1.1) would yield an empirical value for C. For our system

$$A_0 = 0.67N_0 \quad , \tag{5}$$

where NQ is the initial nitrogen concentration in the lithium in weight percent. Furthermore, from our earlier work on the time dependence of the penetration,[4]

$$a \approx 7 \times 10^{-4}/\text{h} \quad . \tag{6}$$

Substituting Eqs. (5) and (6) into Eq. (4) yields

$$X^2 = 0.67t \exp(-7 \times 10^{-4}t) \exp(-15{,}600/T) CN_0 \quad . \tag{7}$$

Plots of X^2 versus NQ for 100-h exposures at 600 and 700°C are shown in Figs. 8.1.2 and 8.1.3, respectively. From the slopes of the best fit lines above about N_0 = 0.40 wt %, C = 91 for 7 = 600°C and C = 140 for 7 = 700°C. Taking the average of the two C values and substituting it into Eq. (4) resulted in an equation that was a good approximation for the penetration depth of type 316 stainless steel in lithium containing greater than 0.60 wt % N:

$$X = [115A_0 \exp(-15{,}600/T) \exp(-at)t]^{1/2} \quad . \tag{8}$$

In determining a value for C, all but one of the data points in Figs. 8.1.2 and 8.1.3 showing zero penetration were ignored. However,

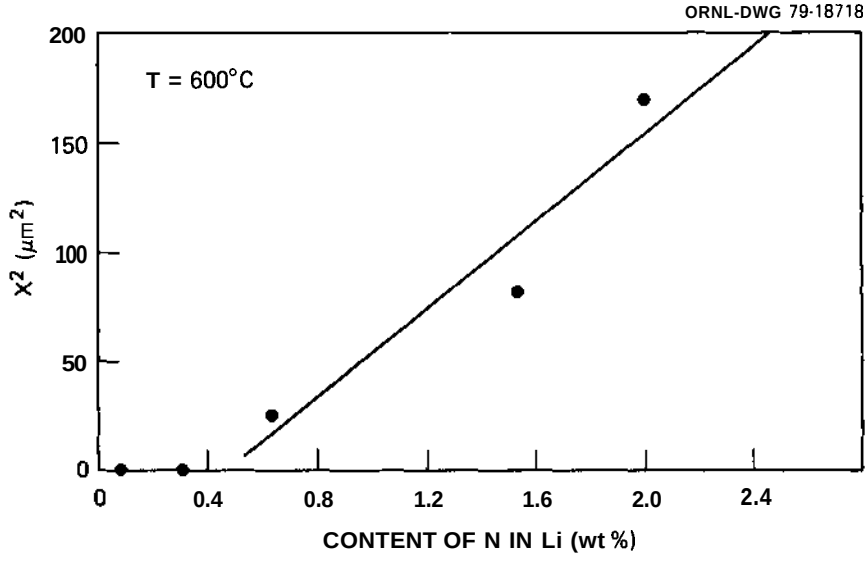

Fig. 8.1.2. Plot of the Square of the Average Grain Boundary Penetration vs the Initial Concentration of Nitrogen in Lithium for Type 316 Stainless Steel at 600°C.

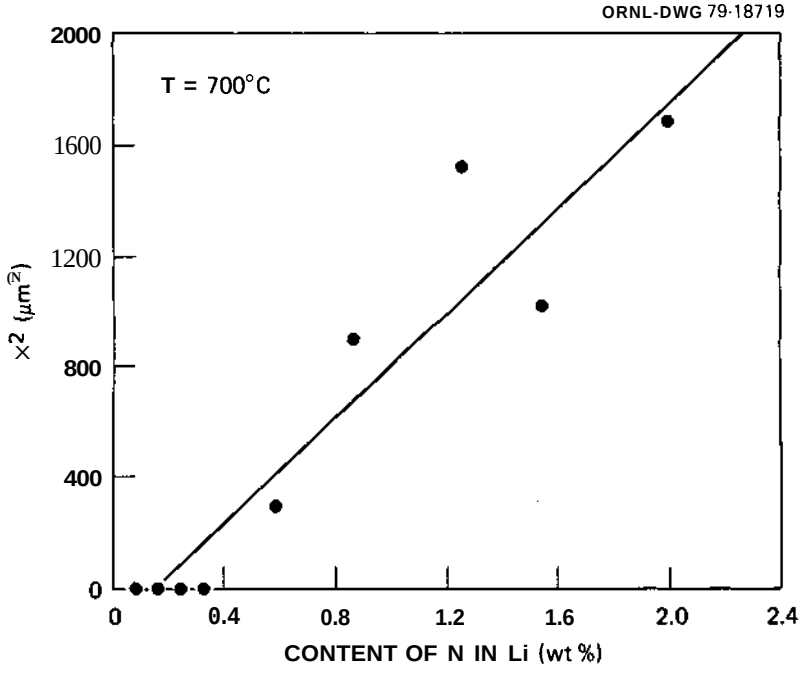

Fig. 8.1.3. Plot of the Square of the Average Grain Boundary Penetration vs the Initial Concentration of Nitrogen in Lithium for Type 316 Stainless Steel at 700°C.

they are valuable measurements because they indicate that the mechanism of penetration associated with the dependences of Eq. (4) are not operative at lower concentrations. As mentioned above, Eq. (4) was based on the findings of Olson et al.,[2] who postulated a mechanism of formation of a grain boundary corrosion product that promoted penetration either along the boundary or in the region immediately adjacent to it. While they found their equation to apply in all cases down to their lowest nitrogen concentrations (3000 wt ppm), our data indicate a threshold between 3000 and 6000 wt ppm. However, we must reiterate that in the former experiments the nitrogen concentration was constant throughout a test, while in our experiments [see Eq. (2)] the actual nitrogen concentration in the lithium decreases exponentially with time. Therefore, the mean concentrations are lower than those at $t = 0$. (For example, in the test with 3100 wt ppm N at 700°C, the final concentration was 1200 wt ppm.) However, regardless of this variation the present results suggest that there is a threshold nitrogen concentration below which the penetration of type 316 stainless steel by static lithium decreases sharply or is eliminated. While we cannot directly couple these results to tests in flowing lithium, it is noteworthy that in two lithium thermal-convection loops of type 316 stainless steel with 600°C maximum temperatures and nitrogen concentrations of 500 and 1700 wt ppm, grain boundary penetration was not evident.[5]

8.1.5 Conclusions

We did not observe degradation of the compatibility of type 316 stainless steel with static lithium containing nitrogen when the concentration of the nitrogen was kept below 1000 to 3000 wt ppm. The penetration predicted by extrapolation of results from experiments with higher nitrogen concentrations in lithium did not occur at these lower nitrogen levels.

8.1.6 References

1. P. F. Tortorelli and J. H. DeVan, "Capsule Tests of Type 316 Stainless Steel in Nitrogen-Contaminated Lithium," *ADIP Quart. Prog. Rep. Sept. 30, 1978,* DOE/ET-0058/3, pp. 84–91.

2. D. L. Olson and D. K. Matlock, *Liquid Lithium Corrosion Research, Prog. Rep. Apr. 1, 1977—Dec. 31, 1977*, COO-2313-7, Colorado School of Mines, Golden, Colo.; see also G. N. Reser, D. L. Olson, and D. K. Matlock, "Liquid Lithium Rate Expressions for Type 304L Stainless Steel," paper 114 presented at NACE Corrosion/79, Atlanta, Ga., Mar. 12-16, 1979.

3. J. H. DeVan and J. R. DiStefano, "Capsule Tests of Iron-Base Alloys in Lithium," *ADIP Quart. Prog. Rep. Mar. 31, 1978*, DOE/ET-0058/1, pp. 190—99.

4. P. F. Tortorelli, J. H. DeVan, and J. E. Selle, "Effects of Nitrogen and Nitrogen Getters in Lithium on the Corrosion of Type 316 Stainless Steel," paper 115 presented at NACE Corrosion/79, Atlanta, Ga., Mar. 12-16, 1979.

5. P. F. Tortorelli and J. H. DeVan, "Corrosion in Lithium-Type 316 Stainless Steel Thermal-Convection Systems," *ADIP Quart. Prog. Rep. Mar. 31, 1979,* DOE/ET-0058/5, pp. 148—55.

8.2 THERMAL-CONVECTION LOOP TESTS OF Fe-Ni-Cr ALLOYS - P. F. Tortorelli and J. H. DeVan (ORNL)

8.2.1 ADIP Task

ADIP Task I.A.3, Perform Chemical and Metallurgical Compatibility Analyses.

8.2.2 Objective

The purpose of this task is to evaluate the corrosion resistance of possible first-wall materials to flowing lithium in the presence of a temperature gradient. Corrosion rates (in terms of both dissolution and deposition) are measured as functions of time, temperature, additions to the lithium, and flow conditions. These measurements are combined with chemical and metallographic examinations of specimen surfaces to establish the mechanisms and rate-controlling processes for dissolution and deposition reactions.

8.2.3 Summary

The status of the various lithium thermal-convection loops (TCLs) is reviewed. The effect of prior loop operation on the corrosion of new type 316 stainless steel specimens was slight: the corrosion rate of this steel in flowing lithium was not greatly enhanced when α-ferrite was also present in the system. Additionally, the reaction of aluminum in lithium with type 316 stainless steel at 500 to 600°C was very rapid and resulted in thin surface films. This process is consistent with the observed kinetics of the growth of aluminum-steel reaction layers.

8.2.4 Progress and Status

As described previously[1] two types of TCLs are being used to evaluate the compatibility of materials with lithium. The first type is in the form of a 0.46- by 0.64-m parallelogram that contains interlocking tab specimens of the same material as the loop. The loop is operated without interruption and is then cut open to remove tab specimens for analysis. The second type of TCL is larger (0.48 by 0.76 m) and is designed so that

tab specimens can be withdrawn and inserted without altering the loop operating conditions. In this way corrosion rates can be monitored at selected time intervals for a given set of test specimens.

It has previously been reported[2] that the corrosion rates of type 316 stainless steel in lithium TCLs became constant with time after an initial period of accelerated weight loss. Among three TCLs operated for greater than 3000, 4000, and 9000 h, these steady-state dissolution rates ranged from about 10 to 20 mg/m^2h (9 to 18 μm/year). Flow restrictions developed in two of the TCLs and necessitated shutting down these loops. Subsequently, their cold legs were cut out and replaced with new ones of similar material (type 316 stainless steel) that were welded into place. (The analysis of a mass transfer plug from one of these cold legs was given in the preceding quarterly report.[3]) The two TCLs were again filled with lithium and flow was reestablished in both. New specimens were inserted into one of the refurbished loops, and corrosion rates have now been measured after 500 and 1000 h. The new data points for the specimen at the 600°C (maximum temperature) position in the loop are shown as the solid circles in Fig. 8.2.1, which also includes the previous data from the loop before its shutdown (open circles). The weight losses of the specimen from the second set are slightly greater than that of the original one.

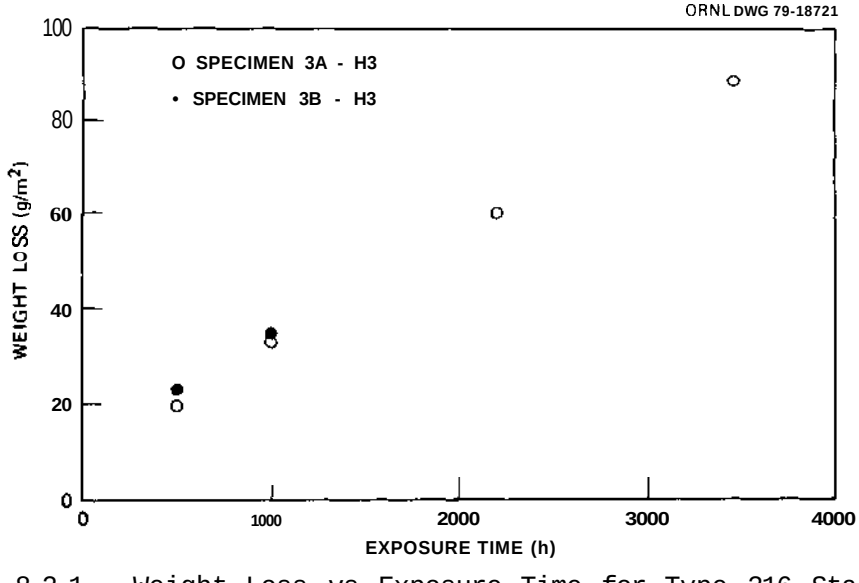

Fig. 8.2.1. Weight Loss vs Exposure Time for Type 316 Stainless Steel in a Lithium Thermal-Convection Loop at 600°C.

The preferential removal of nickel from type 316 stainless steel exposed to flowing lithium leads to a destabilization of the austenitic phase and a subsequent transformation to ferrite in the near-surface region. An α-ferrite surface was thus produced on the inside of the hot leg of the above loop, and by inserting new type 316 stainless steel coupons into it, dissimilar metals were coupled by the lithium. Under such conditions some acceleration of the dissolution of the type 316 stainless steel may be expected as a result of the enhanced driving force for the redistribution of nickel among the various components. However, the observed increase in weight loss shown in Fig. 8.2.1 is small. Consequently, this dissimilar-metal transfer effect is not great under the present conditions.

It has been found1 that the addition of aluminum to lithium reduced the mass transfer rate of type 316 stainless steel by a factor of 5. To confirm this behavior at a higher flow rate and to study the time dependence of this process, the experiment was repeated in one of our larger type 316 stainless steel TCLs (see above) that had operated for greater than 3000 h with pure lithium. An aluminum wire of appropriate weight (5 wt % Al relative to the lithium) was wrapped around the upper part of the hot-leg specimen rod and inserted into the TCL. The lithium flow stopped almost immediately and, despite several attempts, could not be reinitiated. After about 24 h the specimens were taken out of the loop, and most of the coupons in the hot leg had significant weight gains. Weight changes of type 316 stainless steel exposed to Li—5 wt % Al for about 24 h are:

Temperature (°C)	Weight Change (g/m^2)
596	+5.7
592	+6.3
577	+10.5
557	+12.2
538	+6.3
519	+2.9
501	+0.6

While this initial attempt to introduce aluminum into flowing lithium was unsuccessful (although we used a similar method in an earlier test with a small loop[1]), the measurable weight gains of the corrosion coupons within only 24 h indicate that the aluminum must have deposited on the coupon surfaces and that this reaction with the stainless steel was rapid. Metallographic examination revealed some evidence of thin surface layers. This behavior is consistent with the observed time dependence for the aluminum-steel reaction zone depth,[4]

$$x \propto t^{1/2} , \qquad (1)$$

since such a solution applies to a diffusion condition where the diffusing species (in our case aluminum) exists as a thin film on the surface.[5] (A detailed treatment of this aluminum-steel reaction zone and a summary of our earlier results on corrosion inhibition of Fe-Ni-Cr alloys in static and flowing lithium will soon be published.[4]) The reason for the greatest weight gains not being at the hottest points in the loop (see weight change data above) is not known, although it may result from some redistribution of aluminum by localized convective currents. The temperatures noted in the above weight change data are not the actual ones experienced during the 24-h exposure since the temperature profile of the loop was dramatically changed when flow was stopped. Rather, they are the temperatures of the coupons at the moment of their insertion into the loop.

In this quarter a small 45 wt % Fe—31 wt % Ni—21 wt % Cr TCL was put into operation with coupons of Path B Alloys B1 and B3 in the hot zone. Despite the high dissolution rates of higher nickel alloys in static lithium,[6] the loop has completed about 1800 h at a maximum loop temperature of 500°C with no indication of flow restrictions caused by mass transfer deposits. The loop is scheduled to be destructively examined after 3000 h of operation.

8.2.5 Conclusions

1. Corrosion rates in a type 316 stainless steel/flowing lithium/α-ferrite system resemble those in a type 316 stainless steel-flowing lithium system; the effect of dissimilar-metal transfer is slight.

2. The reaction of aluminum in flowing lithium with type 316 stainless steel is rapid and is consistent with the observed kinetics of reaction layer growth in static lithium.

8.2.6 References

1. J. H. DeVan and J. R. DiStefano, "Thermal-Convection Loop Tests of Type 316 Stainless Steel in Lithium," *ADIP Quart. Prog. Rep. Mar. 31, 1973,* DOE/ET-0058/1, pp. 200–08.
2. P. F. Tortorelli and J. H. DeVan, "Thermal-Convection Loop Tests of Stainless Steel in Lithium," *ADIP Quart. Prog. Rep. Deo. 31, 1978,* DOE/ET-0058/4, pp. 120–27.
3. P. F. Tortorelli and J. H. DeVan, "Mass Transfer Deposits in Lithium-Type 316 Stainless Steel Thermal-Convection Loops," *ADIP Quart. Prog. Rep. June 30, 1979,* DOE/ET-0058/6, pp. 89–94.
4. P. F. Tortorelli, J. H. DeVan, J. E. Selle, and H. D. Upton, "Corrosion Inhibition in Lithiura/Ni-Bearing Alloy Systems," to be presented at the IEEE 8th Symposium on Engineering Problems of Fusion Research, San Francisco, Calif., Nov. 15, 1979, and to be published in conference proceedings.
5. P. F. Tortorelli and J. H. DeVan, "The Corrosion of Ni-Fe-Cr and Co-V-Fe (LRO) Alloys in Static Lithium," *ADIP Quart. Prog. Rep. Mar. 31, 1979,* DOE/ET-0058/5, pp. 141-47.

8.3 CORROSION RATE OF TYPE 316 STAINLESS STEEL IN FLOWING KNO_3-$NaNO_2$-$NaNO_3$ — J. R. Keiser and P. F. Tortorelli (ORNL)

8.3.1 ADIP Task

ADIP Task I.A.3, Perform Chemical and Metallurgical Compatibility Analyses.

8.3.2 Objective

Molten salts have been proposed for blanket, coolant, and tritium-processing applications in a fusion reactor. The purpose of the present work is to determine the corrosion behavior of candidate alloys in appropriate molten salts.

8.3.3 Summary

The status of the molten-salt thermal-convection loops (LiF-BeF_2, KNO_3-$NaNO_2$-$NaNO_3$, and LiF-LiBr-LiCl) is reviewed. The corrosion rates of type 316 stainless steel in KNO_3-$NaNO_2$-$NaNO_3$ and the composition of the salt are reported as a function of time and temperature. Corrosion rates varied from about 5 mg/m^2h (4 ym/year) at 430°C to 66 mg/m^2h (59 ym/year) at 550°C.

8.3.4 Progress and Status

As described earlier[1] we are presently investigating the compatibility of structural materials with three molten salts through use of thermal-convection loops (TCLs). The current status of the molten-salt loops is shown in Table 8.3.1. The LiF-BeF2 salt, commonly referred to as flibe, is a potential candidate for the tritium-breeding fluid in a fusion reactor blanket, while the nitrate-based heat transfer salt (HTS) is a possible coolant. The molten-salt mixture LiF-LiCl-LiBr can be used as a process solvent for extracting tritium from lithium. Therefore, all three salts have applications in fusion systems.

Results have been reported earlier[2,3] on the corrosion of type 316 stainless steel exposed to flowing HTS. During the first 10,000 h of operation, the weight loss rates were 7 ym/year at a maximum loop temperature (T_{max}) of 430°C and 8 ym/year at 505°C. The T_{max} was then raised to

Table 8.3.1. Status of Molten-Salt Loops

Loop Material	Specimen Material	Salt Composition	Cover Gas	Current Operating Temperatures, °C (max)	(min)	Operating Time[a] (h)
316 stainless steel	316 stainless steel	$LiF-BeF_2$ (66-34 mol %)	Ar	650	525	30,991
Hastelloy N	316 stainless steel 12 specimens HastelloyN 4 specimens	$NaNO_2-KNO_3-NaNO_3$ (49-44-7 mol %)	Air	505	395	27,466
316 stainless steel	316 stainless steel	LiF-LiCl-LiBr (22-31-47 mol %)	Ar	530	480	9,146

[a]As of Sept. 30, 1979.

550°C, and a new specimen that was exposed for about 6800 h suffered weight loss at a rate of 74 μm/year. The surfaces of the specimens had an oxide layer whose outer zone was low in iron compared with the matrix concentration.[3] Subsequently, loop operation was continued at a T_{max} of 550°C for another 2500 h. As shown in Fig. 8.3.1, which includes all the weight change data to date, the corrosion rate of type 316 stainless steel in HTS remained fairly constant between 6800 and 9300 h. The T_{max} was then reduced to 505°C, where the rate of weight loss returned to approximately the same value measured earlier (see Fig. 8.3.1).

If we assume that the dissolution of type 316 stainless steel in HTS is a thermally activated phenomenon, the corrosion rate, R_w, can be written as

$$R_w = A \exp(-Q/RT) \quad , \tag{1}$$

where Q is the activation energy for the rate-limiting process. Since corrosion rates have now been measured at three temperatures, a plot of

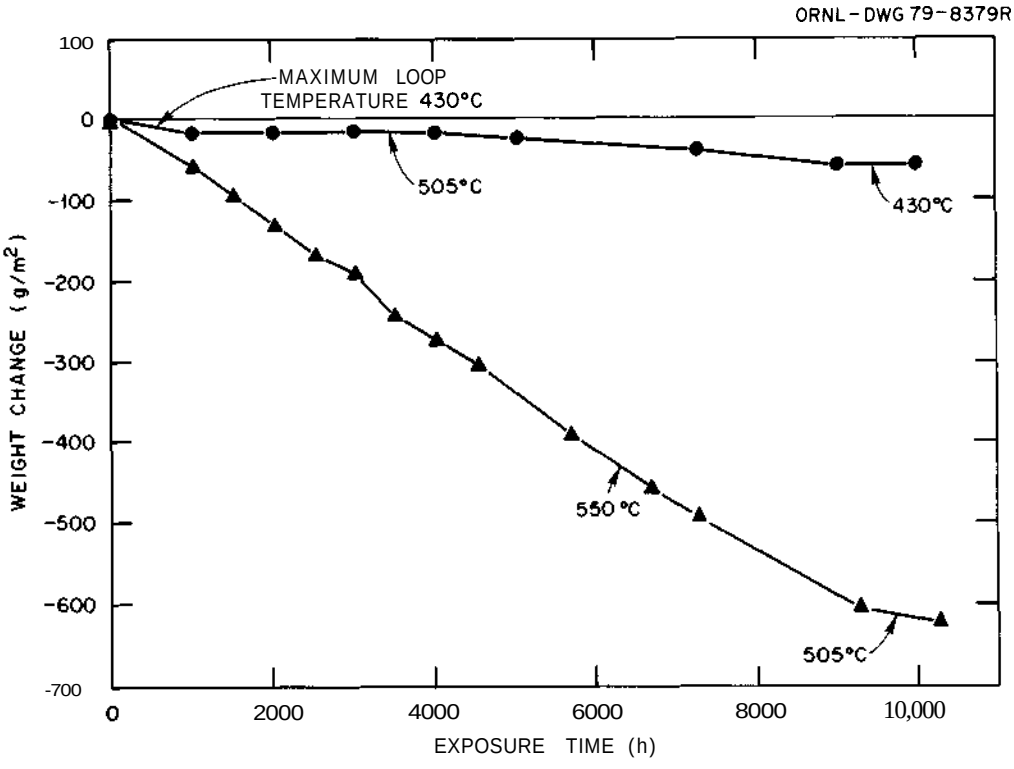

Fig. 8.3.1. Weight Changes vs Time for Type 316 Stainless Steel Exposed to Flowing KNO_3-$NaNO_2$-$NaNO_3$ in a Thermal-Convection Loop.

$\ln R_w$ (where R_w is the average corrosion rate at T) vs $1/T$ (see Fig. 8.3.2) yielded $Q \approx 100$ kJ/mol (24 kcal/mol). This value indicates a dissolution rate controlled by solid-state diffusion:

$$R_w \propto \sqrt{D} = D_0^{1/2} \exp\left(-\frac{Q'}{2RT}\right), \tag{2}$$

since $Q' = 2Q \approx 200$ kJ/mol (48 kcal/mol), which is consistent with values of activation energies for the diffusion of Cr, Fe, or Ni in stainless steel.

The composition of the HTS has been monitored throughout the operation of the TCL, and Table 8.3.2 lists these results. Note that while the concentration of chromium in the salt has continually increased, the iron and nickel concentrations decreased slightly until the maximum loop temperature

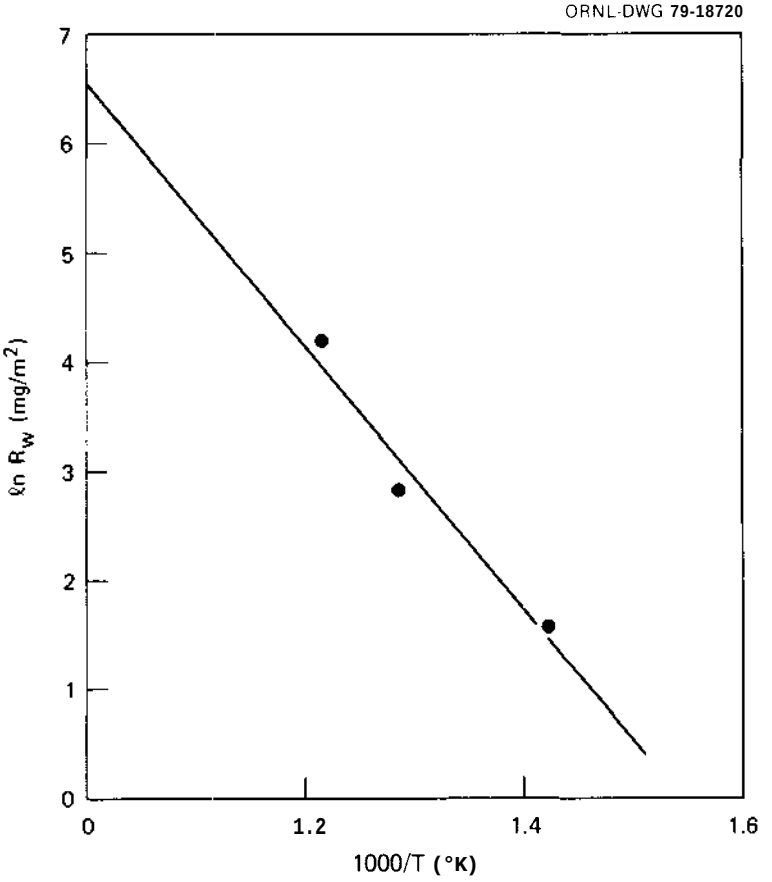

Fig. 8.3.2. Arrhenius Plot of the Corrosion Rate of Type 316 Stainless Steel in Flowing KNO_3-$NaNO_2$-$NaNO_3$ vs Temperature.

Table 8.3.2. Composition of Loop Heat Transfer Salt

Loop Operating Time (h)	Maximum Loop Temperature (°C)	Concentration, wt				
		NO_3^- (%)	NO_2^- (%)	Fe (ppm)	Ni (ppm)	Cr (ppm)
1,512	430	37.6	24.5	17	12	52
2,832	430	39.3	25.3	10	<5	70
5,568	505	35.9	24.7	7	<1	93
9,0.72	505	39.5	25.0	1	<0.1	163
13,632	550	40.1	24.2	34	8	303
15,150	550	39.6	24.6	25	46	429
16,440	550	40.0	24.0	131	27	555
21,120	550	37.9	24.8	<10	<10	747

was raised to 550°C; whereupon they initially increased significantly but then decreased again to fairly low levels. This latter reduction in the amount of iron and nickel in the HTS probably corresponds to the deposition of these elements in the cooler region of the loop. Indeed, electron microprobe analysis of a specimen at the coldest part of the loop (~420°C) revealed near-surface layers enriched in iron and nickel.[3] Since it took several thousand hours for the concentrations of iron and nickel to decrease, the deposition reactions appear to be quite sluggish. Table 8.3.2 also includes the NO_2 and NO_3 concentrations of the HTS and shows that very little change has occurred in their relative concentrations during the 20,000-h operation of the TCL.

8.3.5 Conclusions

The corrosion rate of type 316 stainless steel in flowing KNO_3-$NaNO_2$-$NaNO_3$ increased with increasing temperature and was unacceptable at 550°C. The dissolution appeared to be controlled by solid-state diffusion. The chromium concentration of the salt increased monotonically, while most of the dissolved nickel and iron were deposited in the cooler region of the loop.

8.3.6 References

1. J. R. Keiser and E. J. Lawrence, "Compatibility of Blanket, Coolant and Tritium-Processing Salts," *ADIP Quart. Prog. Pep. Sept. 30, 1978,* DOE/ET-0058/3, pp. 99—100.
2. J. H. DeVan and J. R. Keiser, "Compatibility Studies of Type 316 Stainless Steel and Hastelloy N in KNO_3-$NaNO_2$-$NaNO_3$," *ADIP Quart. Prog. Rep. Mar. 31, 1978,* DOE/ET-0058/1, pp. 209—14.
3. J. R. Keiser, J. H. DeVan, and E. J. Lawrence, "Compatibility of Molten Salts with Type 316 Stainless Steel and Lithium," to be published in *Journal of Nuclear Materials,* December 1979.

DOE/ET-0058/7
Distribution
Category
UC-20, 20c

DISTRIBUTION

1—4. Argonne National Laboratory, 9700 South Cass Avenue, Argonne, IL 60439

L. Greenwood
V. Maroni
D. L. Smith
H. Wiedersich

5—6. Battelle-Pacific Northwest Laboratory, P.O. Box 999, Richland, WA 99352

J. L. Brimhall
D. Dingee

7. Carnegie-Mellon University, Schenley Park, Pittsburgh, PA 15213

J. C. Williams

8—203. Department of Energy, Technical Information Center, Office of Information Services, P.O. Box 62, Oak Ridge, TN 37830

For distribution as shown in TID-4500 Distribution Category, UC-20 (Magnetic Fusion Energy), and UC-20c (Reactor Materials)

204—209. Department of Energy, Office of Fusion Energy, Washington, DC 20545

M. M. Cohen
T. C. Reuther, Jr. (5 copies)

210. Department of Energy, Oak Ridge Operations Office, P.O. Box E, Oak Ridge, TN 37830

Office of Assistant Manager, Energy Research and Development

211. General Atomic Company, P.O. Box 81608, San Diego, CA 92138

S. M. Rosenwasser

212–217. Hanford Engineering Development Laboratory, P.O. Box 1970, Richland, WA 99352

D. G. Doran
J. J. Holmes
R. E. Nygren
E. C. Opperman
R. W. Powell
J. L. Straalsund

218–219. Lawrence Livermore Laboratory, P.O. Box 808, Livermore, CA 94550

M. Guinan
C. M. Logan

220. Massachusetts Institute of Technology, Cambridge, MA 02139

D. J. Rose

221–222. McDonnell Douglas Astronautics Company, East, P.O. Box 516, St. Louis, MO 63166

J. W. Davis
D. L. Kummer

223–225. Naval Research Laboratory, Washington, DC 20375

Superintendent, Materials Science and Technology Division
J. A. Sprague
H. Watson

226–253. Oak Ridge National Laboratory, P.O. Box X, Oak Ridge, TN 37830

Central Research Library (2 copies)
Document Reference Section
Laboratory Records Department (2 copies)
Laboratory Records Department, RC
ORNL Patent Section
B. G. Ashdown
E. E. Bloom (5 copies)
D. N. Braski
J. H. DeVan
T. A. Gabriel
M. L. Grossbeck
M. R. Hill (3 copies)
K. C. Liu
P. J. Maziasz
C. J. McHargue
T. K. Roche
J. L. Scott
P. F. Tortorelli
F. W. Wiffen
J. W. Woods

254–255. Sandia Laboratories, Livermore Division 8316, Livermore, CA 94550

J. Swearengen
W. Bailer

256. University of California, Department of Chemical, Nuclear, and Thermal Engineering, Los Angeles, CA 90024

R. W. Conn

257. University of Virginia, Department of Materials Science, Charlottesville, VA 22901

W. A. Jesser

258. University of Wisconsin, 1500 Johnson Drive, Madison, WI 53706

W. G. Wolfer

259. Westinghouse Electric Company, Fusion Power Systems Department, P.O. Box 10864, Pittsburgh, PA 15236

R. E. Gold

ft U.S. GOVERNMENT PRINTING OFFICE: 1980-640-245/019